

CHALMERS
UNIVERSITY OF TECHNOLOGY

Degradation of metallic interconnects in solid oxide electrolysis cells: mechanisms, materials challenges, and design strategies

Downloaded from: https://research.chalmers.se, 2026-11-27 01:57 UTC

Citation for the original published paper (version of record):
Gunduz, K., Reddy, M., Chyrkin, A. et al (2027). Degradation of metallic interconnects in solid oxide electrolysis cells: mechanisms, materials
challenges, and design strategies. Progress in Materials Science, 165.
http://dx.doi.org/10.1016/j.pmatsci.2026.101872

N.B. When citing this work, cite the original published paper.

research.chalmers.se offers the possibility of retrieving research publications produced at Chalmers University of Technology. It covers all kind of research output: articles, dissertations, conference papers, reports etc. since 2004. research.chalmers.se is administrated and maintained by Chalmers Library

(article starts on next page)

Progress in Materials Science 165 (2027) 101872

Contents lists available at ScienceDirect

Progress in Materials Science

journal homepage: www.elsevier.com/locate/pmatsci

Snapshot Reviews in Emerging Fields

Degradation of metallic interconnects in solid oxide electrolysis cells: mechanisms, materials challenges, and design strategies

Kerem Ozgur Gunduz [a], Mareddy Reddy [b], Anton Chyrkin [c,d], Jan Froitzheim [c,*]

[a] Gebze Technical University, Materials Science and Engineering, 41400 Gebze, Turkey
[b] Alfa Laval Technologies AB, Business Unit Electrolyzer and Fuel Cell Technologies, Lund, 22100, Sweden
[c] Chalmers University of Technology, Department of Chemistry and Chemical Engineering, Kemivägen 10, 41296 Gothenburg, Sweden
[d] Department of Functional Materials Engineering, Faculty of Electronics, Telecommunications and Informatics, Gdańsk University of Technology, ul. G. Narutowicza 11/12, Gdańsk, 80-233, Poland

A B S T R A C T

With their unmatched electrical-to-chemical conversion efficiency, solid oxide electrolysis cells (SOECs) are increasingly recognized as a cornerstone technology for the green energy transition. Realizing this potential, however, critically depends on the durability of key stack components, most notably the metallic interconnects. Metallic interconnects in solid oxide electrolysis cells must withstand aggressive high-temperature, dual atmosphere conditions. This review evaluates the current state of metallic interconnect materials for SOEC stacks, drawing on the more extensive Solid Oxide Fuel Cell (SOFC) literature while highlighting key differences. The analysis is structured around oxidation behavior on the oxygen and hydrogen/steam sides and dual atmosphere effects, with emphasis on the interplay between chromia scale growth, chromium volatilization, and breakaway oxidation and their impact on interconnect lifetime and electrical performance. Key distinctions in SOEC operation, including high steam content, reversed current polarity, and dual atmosphere exposure, are highlighted, revealing conditions where SOFC-based insights fail or require modification. The review evaluates alloy design and coating strategies and identifies critical knowledge gaps, particularly in low-temperature steam-side corrosion and dual atmosphere degradation, outlining priorities for SOEC-specific material development.

1. Introduction

Solid oxide cells (SOCs) are electrochemical devices that can operate either in fuel cell or electrolysis mode, enabling efficient energy conversion and storage. Solid oxide fuel cells (SOFCs) generate electricity by electrochemically oxidizing the fuel, whereas solid oxide electrolysis cells (SOECs) operate in reverse, using electricity to split water into hydrogen or to co-electrolyze CO_2 and H_2O into syngas ($CO + H_2$). In practical applications, individual cells are stacked in series to increase voltage and power output, requiring an interconnect (IC) component to electrically connect adjacent cells.

The interconnect plays a crucial role by electrically linking adjacent cells as well as physically separating fuel and oxidant gases to prevent mixing and unintended combustion. Additionally, it provides structural rigidity and stability to the stack, maintaining integrity under high temperatures and compressive loads. Optimizing interconnect materials and design is therefore essential for improving the performance, durability, and efficiency of SOC stacks.

SOCs operate under extreme conditions, including high temperatures (600–1000 °C) and simultaneous exposure to both oxidizing and reducing atmospheres. Traditionally, ceramic materials such as lanthanum chromite were used as interconnects due to their chemical stability. However, their high cost, brittleness, and low thermal conductivity have limited their application.

With the advances in design (electrode and metal supported cells instead of electrolyte supported cells) and development in

* Corresponding author.
E-mail address: jan.froitzheim@chalmers.se (J. Froitzheim).

https://doi.org/10.1016/j.pmatsci.2026.101872
Received 6 June 2026; Received in revised form 9 October 2026; Accepted 25 October 2026
Available online 29 October 2026
0079-6425/© 2026 The Author(s). Published by Elsevier Ltd. This is an open access article under the CC BY license (http://creativecommons.org/licenses/by/4.0/).

materials (e.g. ceria-based electrolytes), operating temperatures of SOCs dropped significantly to 600–800 °C, referred to as intermediate temperature solid oxide cells (IT-SOC). This drop in temperature enabled the utilization of metallic materials as interconnects. Metallic materials overcome the aforementioned limitations, making them promising candidates for interconnect applications at elevated temperatures. Compared to ceramics, metallic interconnects offer benefits such as lower material cost, enhanced thermal conductivity, greater ductility and lower manufacturing costs. A primary challenge, however, is their susceptibility to high temperature oxidation, which leads to the formation of a resistive oxide scale (detailed in sections 5 and 6) and may even cause stack failure. This oxide scale reacts with the environment and releases volatile chromium species (section 4) which then may condense at the air electrode, poisoning electrocatalytic sites (triple phase boundaries) and consequently degrading cell performance and operational lifespan. The growth of this oxide scale also increases the resistance across the cells, thereby leading to significant ohmic polarization losses. To address these limitations, novel steel compositions with enhanced oxidation resistance and superior electrical properties, specifically designed for interconnect applications, have been developed. To further improve these properties, various coatings have been devised. These coatings, including spinel oxides, perovskite oxides, and reactive element oxides, vary in their composition and structure, as discussed in section 5.4.

With approximately 40,000 publications, the SOC field is extensively studied. However, only a small fraction (less than 5%) of this work addresses interconnect materials. Cost analyses vary greatly due to different design assumptions, but interconnects are widely recognized as a major contributor to stack cost, highlighting the importance of developing durable and cost-effective interconnect materials [1–3]. The importance of the interconnect for stack durability has been demonstrated by Beyrami et al. [4] who modelled SOEC stack lifetime and identified interconnect failure as the limiting end-of-life criterion under a wide range of operating conditions.

The first review on metallic interconnect materials was written by Quadakkers et al. in 2003 [5] which already identified ferritic stainless steels (FSS) as the most suitable interconnect material for SOCs operating at and below 800 °C. Since then, extensive research on interconnect steels and coatings for SOFCs has been carried out. A Scopus search for "SOFC, interconnect, coating" provides 700 studies while there are only a handful of studies investigating SOEC operation. While both systems use similar ceramic materials and operate at high temperature, the operating conditions differ. Interconnects face individual challenges in SOECs and SOFCs due to differences in their respective operating environments and gas compositions, which demand a thorough reassessment of interconnect degradation. In this review, we use the large body of research on SOFC to outline challenges and solutions in the context of SOEC, discuss where results can be directly transferred and where this is not the case. We will limit our discussion to steam electrolysis with planar SOEC designs. Other SOEC applications include conversion of CO_2 to CO and co-electrolysis of CO_2/H_2O mixtures directly to syngas ($CO + H_2$) [6]. The latter promises increased efficiency for syngas production compared to steam electrolysis and a subsequent water–gas shift reactor. However, introduction of carbon containing species results in a series of new degradation challenges such as carburization and carbon deposition, which are distinct from those encountered during steam electrolysis and are therefore not considered here. Although tubular SOECs have been considered, this design is more typical for SOFC operation. For more information on tubular SOCs the reader is referred to these reviews [7,8].

The review will discuss the differences in SOFC and SOEC, outline fundamental concepts in high temperature oxidation, introduce interconnect steels with the emphasis on alloying elements and alloy design. In sections 5 and 6 air and steam side oxidation are discussed, respectively. Section 7 focuses on dual atmosphere oxidation i.e. the simultaneous exposure of the steel to both of these

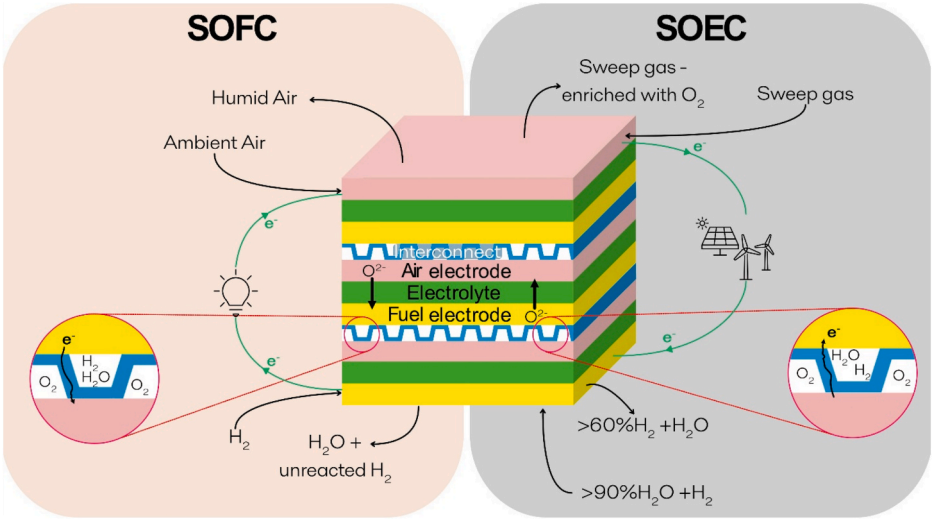

Fig. 1. Schematic comparison of the operating environments in planar solid oxide fuel cell (SOFC) and solid oxide electrolysis cell (SOEC) operation. The different electrochemical reactions result in distinct gas atmospheres at the interconnect. In SOFC mode, the air side is exposed to a high flow of ambient air, while the fuel side consists of H_2-rich gas with increasing steam content towards the outlet. In SOEC mode, the situation is reversed: the fuel-side inlet contains predominantly H_2O with little H_2, and steam content decreases along the flow path. On the oxygen side, a sweep gas is typically enriched in O_2 as it passes through the stack.

atmospheres while section 8 discusses how the oxidation process affects the electronic resistance of the oxide scale and the effect of current and stack operation on the oxidation properties.

Fig. 1 compares the operating environments of a stack operating in SOFC and SOEC mode. Both technologies employ essentially the same multilayer cell architecture consisting of an air electrode, electrolyte and fuel electrode. However, the electrochemical reactions and electronic current proceed in opposite directions. This reverse operation results in fundamentally different gas compositions, electrical polarity, oxygen chemical potential and current flow at the interconnect–electrode interfaces. Differences in gas atmospheres, electrical polarity, and thermal profiles lead to variations in degradation behavior between SOFC and SOEC, these will be discussed in the respective sections. To avoid confusion associated with mode-dependent anode and cathode terminology, the terms oxygen electrode and fuel/steam electrode are used throughout this review.

In SOEC mode, the oxygen electrode operates under higher oxygen partial pressures (pO_2 >0.21 bar) due to continuous oxygen evolution during electrolysis in a potentially H_2O free environment. On the fuel side in SOEC mode, steam concentrations are typically very high, often above 90% at the inlet, which is not the case in SOFCs that usually operate at lower fuel utilization. The result is that in SOEC mode, both sides of the interconnect are subject to different oxidizing conditions than their respective counterparts in an SOFC. Furthermore, the thermodynamics of cell reactions create distinct thermal profiles within the stack. The exothermic nature of the SOFC reaction requires large amounts of cooling air to maintain stable operating temperature. On the other hand, SOECs require no cooling, but air may be provided as a sweep gas to dilute O_2 concentrations for safe operation. Although in SOEC the process is endothermic, it is mostly operated thermoneutral or even slightly exothermic, depending on the operating voltage due to ohmic losses. Additionally, SOECs are poised to operate at higher current densities, with reversed current flow, potentially intensifying interfacial degradation mechanisms (see section 8.2).

Emerging SOEC designs increasingly consider pressurized operation to improve hydrogen production efficiency and reduce downstream compression costs. Elevated pressure can further modify oxidation kinetics and scale adherence, though systematic studies under these conditions remain limited (see section 5.5).

The combination of high steam content, reversed current polarity, elevated oxygen partial pressures, and intermittent operation in SOECs creates a unique set of challenges for interconnect materials. Degradation mechanisms observed in SOFCs such as chromia scale growth, chromium volatilization, and breakaway oxidation, i.e. the formation of fast growing Fe-rich oxides, may be accelerated, suppressed or fundamentally altered under SOEC conditions. As a result, insights from SOFC research cannot always be directly transferred to SOECs; careful reassessment is required, as discussed throughout this review.

2. Fundamentals of high-temperature oxidation

Prior to presenting and discussing specific findings, an introduction to the fundamentals of high temperature oxidation is given to provide a framework for the upcoming sections. With respect to SOEC interconnects in steam electrolysis, the corrosive species are O_2 and H_2/H_2O. The latter is often referred to as reducing atmosphere although an FSS interconnect will still oxidize in these conditions.

As in all chemical reactions, the oxidation reaction is governed by thermodynamics and kinetics. Thermodynamics determine whether the reactions under given conditions will occur or not, while kinetics determine the rate of the reaction.

Thermodynamically, all commonly used alloying elements in interconnect steels (Fe, Cr, Mn, Si, Ti) are stable as oxides under typical SOEC conditions. Hence oxidation of such elements is spontaneous. By contrast, metals with lower oxygen affinity that are commonly used in coatings, such as Ni, Co, or Cu, remain stable in metallic form over much of the fuel side oxygen partial pressure range.

Regarding kinetics, the oxidation process begins with the adsorption of oxygen atoms on the surface followed by oxide nucleation and growth until the whole surface is covered with the oxide film [9]. After complete coverage, the reaction usually proceeds with diffusion controlled parabolic oxidation described by Eq. (1) [10]:

$$X^2 = 2K_p t \tag{1}$$

X is the scale thickness, t is time and K_p is the parabolic growth rate constant in units $cm^2\ s^{-1}$. The parabolic rate law is also commonly expressed in terms of mass gain according to Eq. (2) [10]:

$$\left(\frac{\Delta m}{A}\right)^2 = 2K_w t \tag{2}$$

Here Δm is the mass gain while A is the surface area, t is time and K_w is the parabolic growth rate in $g^2cm^{-4}s^{-1}$ determined by mass gain measurements [10]. It should be noted that the notation for K_p and K_w is somewhat inconsistent in the literature. Furthermore, some publications do not consider the integration constant (=2) in Eq. (2). Thus, one should be careful when making comparisons between parabolic rate constants. It is worth noting that the parabolic rate law often provides a good approximation while being based on a very simple physical model that assumes a single phase, compact oxide with uniform properties (e.g. no grain boundary effects) [9,10]. Due to these assumptions, deviations are not uncommon. In the case of interconnects typically a duplex oxide scale, $Cr_2O_3/(Cr,Mn)_3O_4$, complicates Wagnerian modeling because the two layers have different growth and depletion rates [11–14]. A SiO_2 sublayer may also form depending on the Si content, while elements with high oxygen affinity, such as Ti and Al, form oxide precipitates beneath the Cr_2O_3/metal interface [15–18]. Such precipitates develop due to reaction between dissolved oxygen and these elements, known as internal oxidation (addressed in the following text). Furthermore, specimen thickness, initial grain size, and microstructural changes such as austenitization can affect oxidation kinetics [19–24]. Alterations in the oxide scale such as varying defect equilibria [25],

defects in the oxide and oxide spallation [21], oxide grain size and coarsening [26,27] can additionally cause deviations of the simple parabolic kinetics.

A particularly important deviation from parabolic oxidation kinetics under simulated SOFC conditions is caused by Cr(VI) evaporation. At temperatures below approximately 700 °C in humid air, chromium volatilization can outweigh the mass gain associated with oxide growth, resulting in a net mass loss [28–31].

This effect is expected to be negligible in H_2/H_2O and dry SOEC oxygen-side atmospheres and is discussed in more detail in Section 4. More generally, the oxidation atmosphere, including air, H_2/H_2O, and dual-atmosphere conditions, strongly influences the oxidation behavior, particularly at lower temperatures such as 600 °C. In addition, interconnects are commonly coated with protective oxides such as $(Co,Mn)_3O_4$ to suppress Cr(VI) evaporation, while reactive-element coatings containing Ce, La_2O_3, Y_2O_3, or CeO_2 can slow down oxide growth rate along with improved adhesion (see Section 3.1) [32,33]. In both cases oxidation kinetics will be affected. Despite these deviations from parabolic law, in some cases parabolic kinetics provide a good approximation to describe the growth kinetics. Hence, for lifetime modeling, potential deviations from parabolic kinetics need to be assessed and it is advised that investigations should be carried out in a system specific manner.

Another important term in oxidation of high-temperature alloys relevant in this context is breakaway oxidation. It occurs when the slow growing protective Cr_2O_3 scale can no longer be maintained. Classically this occurs after long periods of protective parabolic growth. At some point, due to a critical Cr depletion at the metal/oxide interface, the Cr_2O_3 scale growth can no longer be maintained, and fast-growing Fe-rich oxides form instead [34,35].

For interconnects this often manifests itself in the form of Fe-rich oxide islands with an outer part of Fe_2O_3 (oxidation in air or O_2) and an inward growing part of $(Fe,Cr)_3O_4$. These oxide islands increase in number and size until the entire surface is covered with Fe-rich oxide [35]. The transition from protective parabolic growth to breakaway oxidation can usually be seen in the mass gain curve by a sharp increase in oxidation rate. This is illustrated in Fig. 2. Hence, the initiation of breakaway oxidation marks the oxidation induced end of service lifetime of the interconnect.

Therefore, the initial formation of a protective $Cr_2O_3/(Cr,Mn)_3O_4$ double layered oxide and its maintenance during operation is critical for the service lifetime of interconnects. The amount of Cr necessary to form and maintain a protective Cr_2O_3 scale can be estimated using two expressions developed by Carl Wagner [36,37]. The Wagnerian criteria are based on equating fluxes of the competing species, i.e., Cr flux toward the alloy surface (Cr diffusivity) vs oxygen flux into the metal (oxygen permeability) (Eq. (4)) or Cr consumption by oxide growth (parabolic rate constant) vs Cr supply (Cr diffusivity) to the alloy surface (Eq. (5)) once a continuous oxide scale is formed.

Prior to discussing these expressions, it is important to state that both formulae are derived in conditions where Fe cannot oxidize which is only true for low humidity H_2 SOEC environments (at 600 °C for $H_2/H_2O > 3.55$). In that case the oxidation reaction for a Fe-Cr metal where only Cr oxidizes is expressed as Eq. (3):

$$Cr + 1.5O \rightarrow CrO_{1.5} \tag{3}$$

Among the two criteria, the first criterion predicts the critical Cr content above which an external Cr_2O_3 scale will form on the alloy surface [37]. Below this value, Cr will oxidize inside the metal and form Cr_2O_3 precipitates within metal instead of forming an external layer. This is illustrated schematically in Fig. 3 [38]. This immobilizes Cr and prevents the formation of a protective oxide scale. This type of oxidation is defined as internal oxidation. It is also a diffusion controlled process and follows parabolic oxidation kinetics. For further information on internal oxidation please refer to [10]. Nonetheless, which regime prevails depends on the competition between oxygen flux and Cr flux in the metal and is expressed as Eq. (4):

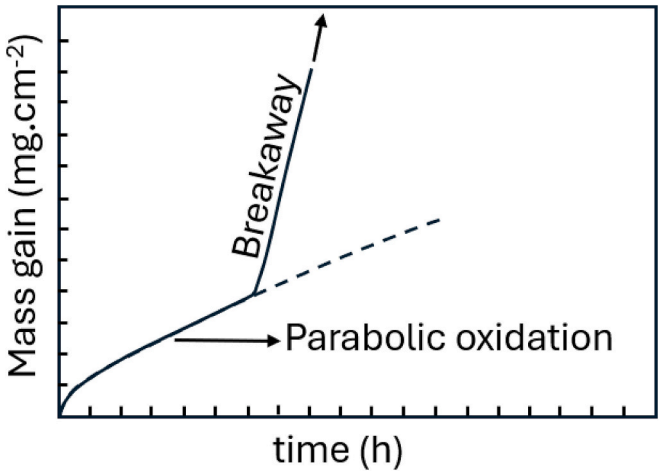

Fig. 2. Schematic mass gain vs time curves for FSS interconnects: protective parabolic oxidation (dashed line projection) and the initiation of rapid breakaway oxidation (solid line inflection). Breakaway oxidation corresponds to the loss of chromia-scale protectiveness and marks the onset of accelerated degradation.

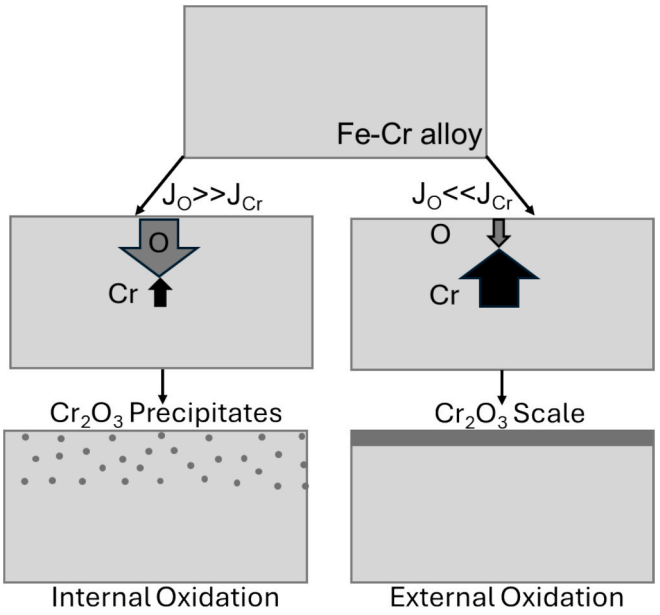

Fig. 3. Schematic illustration of the competition between chromium and oxygen transport governing internal and external oxidation. After Nanko and Do [38].

$$N_{Cr}^{(1)} = \left[\frac{\pi}{2\nu}g^{*}\frac{V_m}{V_{ox}}\frac{N_O^{(s)}D_O}{D_{Fe-Cr}}\right]^{\frac{1}{2}} \tag{4}$$

$N_{Cr}^{(1)}$ is the critical Cr concentration, $N_O^{(s)}$ is the oxygen solubility in the steel. D_o and $D_{Fe\text{-}Cr}$ are the lattice diffusion coefficients of O and Cr respectively. V_m and V_{ox} are the molar volumes of Fe-Cr steel and Cr_2O_3 approximately 7 and 15 cm^3 $mole^{-1}$ respectively. The value g* was experimentally determined originally on In-Ag alloys as 0.3 which corresponds to the critical volume ratio of oxide/metal required for the transition from internal to external oxidation [36]. v is equal to 1.5 and represents a stoichiometric factor for the reaction of Cr into $CrO_{1.5}$ (Eq. (3)). Eq. (4) was derived for a binary alloy in which the base metal is noble and does not oxidize. However, in most SOEC relevant environments both Fe and Cr will oxidize which might require a correction factor [39].

After the formation of an initial protective Cr_2O_3 scale, the second criterion predicts the minimum Cr concentration required to maintain this initially formed scale [36]. This 2nd criterion is expressed as Eq. (5):

$$N_{Cr}^{(2)} = \left(N_{Cr}^{(o)} - N_{Cr}^{(i)}\right) = \frac{V_m}{V_{ox}}\left(\frac{\pi K_p}{2D_{Fe-Cr}}\right)^{\frac{1}{2}} \tag{5}$$

$N_{Cr}^{(2)}$ is the minimum Cr concentration to maintain a Cr_2O_3 scale while $N_{cr}^{(o)}$ is the initial Cr concentration of the alloy and $N_{cr}^{(i)}$ is the Cr concentration at the oxide-alloy interface. V_m and V_{ox} are the molar volume for the Fe-Cr steel and Cr_2O_3 respectively. K_p is the oxide growth rate and D is the interdiffusion coefficient for Fe-Cr alloy. It should be noted that the equation does not account for Cr loss due to Cr(VI) evaporation.

To calculate $N_{Cr}^{(1)}$ and $N_{Cr}^{(2)}$ for the Fe-Cr system several literature data sets can be used although some extrapolation to lower temperatures is required. The required data are N_OD_O, $D_{Fe\text{-}Cr}$ and K_p. Chyrkin et al. recently made a critical review of the available data sets [40]. Regarding $N_O^{(s)}$ D_O the commonly considered values are within one standard deviation, except for the data of Takada et al.

Table 1
Calculated $N_{Cr}^{(1)}$ and $N_{Cr}^{(2)}$ values based on literature data.

Temperature (°C)	$N_o^{(S)}D_O(cm^2s^{-1})$	$D_{Fe\text{-}Cr}(cm^2s^{-1})$	$K_p(cm^2s^{-1})$	$N_{Cr}^{(1)}$	$N_{Cr}^{(2)}$
500	$3.3x10^{-17}$	$9.7x10^{-16}$	$2.9x10^{-19}$	0.070	0.010
550	$2.9x10^{-16}$	$7.3x10^{-15}$	$3.1x10^{-18}$	0.078	0.012
600	$1.8x10^{-15}$	$4.1x10^{-14}$	$2.6x10^{-17}$	0.081	0.015
650	$9.6x10^{-15}$	$2.0x10^{-13}$	$1.7x10^{-16}$	0.086	0.017
700	$4.4x10^{-14}$	$8.0x10^{-13}$	$9.1x10^{-16}$	0.090	0.020
750	$1.7x10^{-13}$	$2.8x10^{-12}$	$4.1x10^{-15}$	0.094	0.022
800	$5.9x10^{-13}$	$9.0x10^{-12}$	$1.6x10^{-14}$	0.098	0.025
850	$1.8x10^{-12}$	$2.6x10^{-11}$	$5.8x10^{-14}$	0.102	0.028
900	$5.1x10^{-12}$	$6.7x10^{-11}$	$1.8x10^{-13}$	0.106	0.031

[40–46]. For the calculations below, the classical data set of Swisher and Turkdogan is used [42]. For $D_{Fe\text{-}Cr}$ values the most recent dataset of Williams and Faulkner is preferred (210 kJ/mole) [47] since this data set is obtained on a composition similar to interconnect steels. This set agrees well with studies at elevated temperatures [48,49]. For K_p values Brylewski et al. oxidized Crofer 22 APU in air and found an activation energy around 251 kJ/mole [50]. Brylewski also reviewed the available data and showed that the activation energy of interconnect steels is within the range between 230–280 kJ/mole. Based on these calculations $N_{Cr}^{(1)}$ increases from ~ 7 to 11% as the temperature increases from 500 to 900 °C (see Table 1). $N_{Cr}^{(2)}$ has a weak temperature dependence because of the fast diffusivity of Cr in Fe-Cr alloys. According to experimental observations, Fe-Cr alloys containing above 10 wt% Cr are considered as external chromia formers at typical SOEC operating temperatures [51]. To provide sufficient Cr reservoir to allow for a lifetime of several 10,000 h and to better match the thermal expansion coefficient of the cell, a Cr concentration between 18–22 wt% is common for interconnect steels. Additionally, the trend with respect to temperature fits well with the recent findings of Chyrkin et al. on ferritic Fe-10Cr-2Mo alloy between 800–1100 °C [23]. However, it should be emphasized that the used diffusion and permeability data are for bulk materials. While at temperatures > 800 °C these equations can predict the behavior of Fe-Cr alloys remarkably well at lower temperatures diffusion is increasingly governed by diffusion along interfaces such as grain boundaries [43]. Under these circumstances the models require adjustments to provide meaningful results.

The second criterion, although useful, is valid for semi-infinite slabs. Yet the interconnect steels used in SOC are thin and vary around 200–500 μm [19]. Hence the thickness of the steel will eventually affect the depletion profile as depletion from both sides overlaps and will decrease the Cr concentration in the steel. This was demonstrated by Huczkowski et al. and Chyrkin et al. for ferritic interconnect steels [22,33]. The slope of the depletion profile is determined by the $K_p/D_{Fe\text{-}Cr}$ ratio. For Ni-base alloys and austenitic steels the slope will be steep since Cr diffusion in these alloys is slow. For ferritic Cr_2O_3 formers diffusion of Cr is fast and rather flat diffusion profiles can be obtained [22,33]. Additionally, from an application perspective it is important to estimate how long the interconnect steel will last under SOEC service conditions. In other words, prediction of the onset of breakaway corrosion (t_B). Models that take steel thickness into account and predict the onset of breakaway oxidation including thin components (e.g. 200–500 μm) are summarized by Pillai et al. [21] and Chyrkin et al. [22]. For further details please refer to the references [21,22,33,52–55].

Yet, additional mechanisms such as Cr(VI) evaporation, formation of cracks due to thermal cycling or hydrogen related effects might significantly reduce the onset of breakaway. Evans et al. [56] showed the effect of stress on the breakaway oxidation and hence classified the failure types as I) Intrinsic Chemical failure where the steel depletes until the point where the oxide is not thermodynamically stable at the metal/oxide interface. In contrast, II) Mechanically Induced Chemical Failure (MICF) occurs when cracking or spallation of the oxide scale exposes a Cr-depleted alloy surface that is unable to regenerate the protective Cr_2O_3 scale. The effect of stress on interconnect steels was shown by Galerie et al. by deliberately forming cracks on the surface [34].

Finally, predictions of steel lifetime based on depletion are mostly carried out in air. Such studies are not available in SOEC related steam side (H_2/H_2O) or in dual atmosphere conditions, especially at low temperatures (550–650 °C). This is partly due to failure of these steels after very short exposure durations and the failure mechanisms are still not completely understood [57–59]. Yet for the future, performing such studies is essential, especially under high humidity containing H_2/H_2O atmosphere and dual atmosphere to determine interconnect lifetime under these conditions.

3. Interconnect materials and alloy design

Early SOFC designs relied on ceramic interconnects made of doped $LaCrO_3$ [60]. Subsequently, there has been a transition to

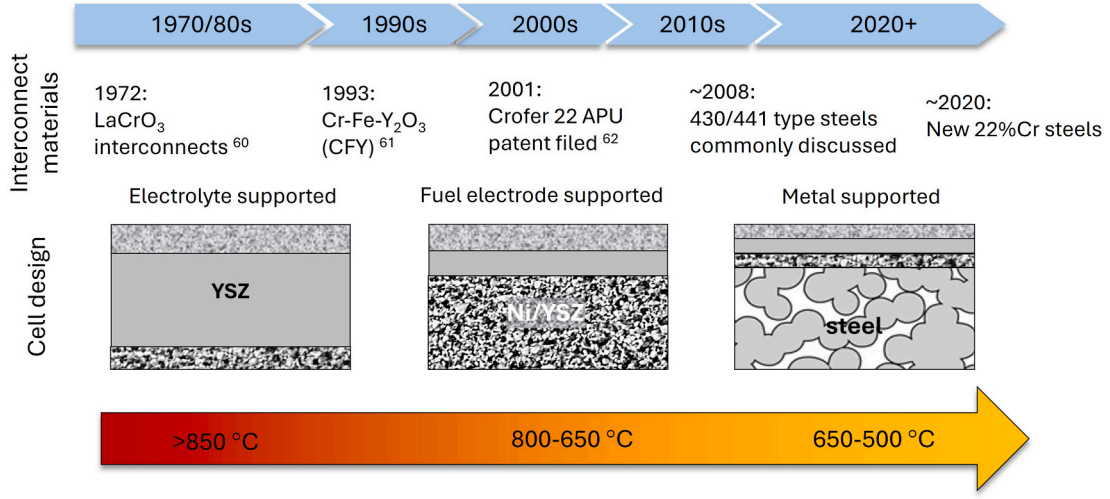

Fig. 4. Schematic illustration of the interdependence between cell architecture, operating temperature, and interconnect materials. While lower operating temperatures create opportunities for lower-cost interconnect materials, established high-temperature cell designs continue to employ Cr-based alloys. Microstructures are based on Jiao et al.[63] and Udomsilp et al.[64].

metallic interconnects [61,62], driven by advances in cell design and reductions in operating temperature. Fig. 4 provides an overview of the historical development of interconnect materials in relation to these technological shifts. A range of chromia-forming alloys has been investigated for this application, including ferritic stainless steels (FSS), austenitic stainless steels, Cr-base alloys, and Ni-base alloys. While Ni-base alloys offer superior high-temperature corrosion resistance, their coefficient of thermal expansion (CTE) is poorly matched to other stack components which is also the case for austenitic stainless steels. As a result, only FSS and Cr-base alloys are generally considered suitable for interconnect applications [5].

Cr-base alloys such as Plansee Ducrolloy or CFY (Cr–5%Fe–1%Y_2O_3) were initially explored as substitutes for ceramic interconnects due to their excellent corrosion and electrical properties [61]. Operating temperatures have decreased from ~ 1000 °C to ~ 850 °C for modern electrolyte-supported cells, ~750 °C for fuel electrode-supported cells, and ~ 600 °C for metal-supported cells. This shift has enabled the use of metallic interconnects, such as Crofer 22 APU [62], with steels dominating below ~ 800 °C due to their lower cost and superior manufacturability. As such, cell design, operating temperature, and interconnect material selection are closely interlinked. CFY remains in use for some electrolyte-supported designs, whereas FSS dominate at temperatures below 800 °C due to their ease of manufacturing and lower cost. Therefore, the following sections focus on FSS, beginning with the influence of alloying elements and continuing with an examination of commercial steels, including those specifically developed for SOC applications.

3.1. Effect of alloying elements

3.1.1. Chromium

The main purpose of chromium additions is to stabilize the ferritic structure and to provide corrosion protection. If the Cr supply is sufficient, a protective Cr_2O_3 layer is formed on the steel surface. A higher Cr content results in a lower CTE and provides a larger Cr reservoir, which is desirable although above ~ 23–24 wt% Cr there is a risk for brittle σ-phase formation [65,66]. σ phase is a FeCr intermetallic that is known to cause embrittlement. In binary Fe-20 wt% Cr alloys σ-phase formation is predicted to occur below ~ 600 °C according to the Fe-Cr phase diagram. At such low temperatures, kinetics for σ-phase formation is slow and it is usually not observed in Fe-22Cr steels, even after long exposure times [19]. Xiong et al. [66] observed nano sized Cr enriched regions by dedicated APT studies on 26 wt% Cr steel at 500 °C after 1000 h. Furthermore, Hammer et al. [65] have clearly observed σ-phase on 26 wt% Cr steels at 700 °C. Interdiffusion of Ni, which occurs when the interconnect is in contact with a Ni-rich contact layer, also promotes σ-phase formation and it has been observed in this context on 22 wt% Cr steels [67].

3.1.2. Manganese

Most steels discussed for interconnect applications contain about 0.5% Mn. Manganese diffuses through the chromia scales to form a $(Cr,Mn)_3O_4$ spinel cap layer. This reduces Cr(VI) evaporation by 2–3x at 800 °C which is commonly considered too much for SOFC applications [68]. The spinel's conductivity is claimed to be >10x higher than Cr_2O_3 [69]. However, further addition of Mn is detrimental since it increases the oxidation rate and causes spallation [70,71].

3.1.3. Silicon and aluminum

Small amounts (<0.5 wt%) of Si and Al are commonly found in many steels, as these elements are used as deoxidants during the steel production process. To avoid the presence of these elements, more expensive production methods, such as vacuum induction melting, are required. In Fe-Cr alloys, aluminum tends to oxidize internally, forming discrete particles near the metal surface, while silicon typically forms a silica sub-layer at the metal-oxide interface [16,72,73]. This silica layer is expected to deteriorate scale adhesion due to its low thermal expansion coefficient, especially in cyclic oxidation conditions [74]. It is commonly believed that such a silica layer results in an increase in Area Specific Resistance (ASR) [72,73,75]. Yet, Huczkowski et al. [16] observed no significant difference in the ASR between two Crofer 22 APU type steels with varying Si content (0.11 wt% Si vs < 0.01 wt% Si). Furthermore, Chen et al. [58] showed that the thermally grown silica sublayer improves the protectiveness in H_2/H_2O atmospheres.

3.1.4. Refractory elements (Nb, W, Mo)

The presence of Nb results in the formation of Laves phase precipitates (Fe_2Nb). Apart from improving creep strength these precipitates tie up Si [16]. This allows Si to be present in the alloy without having a detrimental effect on ASR. However, excess Nb increases oxidation rates [76,77]. W and Mo also act as strengthening elements and tend to be concentrated in the Laves phase precipitates [78,79]. Furthermore, Nb, W and Mo stabilize the bcc structure reducing the risk of austenite formation once the steel is depleted in Cr at high temperatures (≥850 °C) [22,24].

3.1.5. Titanium

Ti is a ferrite stabilizer and the main purpose for including Ti is to tie up the remaining carbon by forming carbides and/or carbonitrides [80]. TiO_2 is more stable than Cr_2O_3. Therefore, when present in the alloy, Ti undergoes both internal oxidation and forms oxide particles at the outermost layer of the oxide [16]. Internal oxidation is suppressed when the alloy contains Al and Si. Ti doping of Cr_2O_3 enhances oxide conductivity but accelerates chromia growth rate [81,82]. TiO_2 internal precipitation leads to strengthening of the near-surface region which enhances the material's resistance to surface wrinkling, which can otherwise occur from the relaxation of oxidation-induced stresses during thermal cycling [82]. Suggested mechanisms behind the acceleration of oxide growth rate are i) formation of ionic defects due to doping effect [82] and ii) grain refinement of Cr_2O_3 due to segregation of TiO_2 on Cr_2O_3 grain boundaries [83].

3.1.6. Reactive elements (Ce, La, Hf, Y, Zr etc.)

Many high-temperature alloys contain very small amounts (100 ppm to 0.1%) of rare earth elements. These small additions of "reactive elements" are well known to have a strong beneficial effect on oxidation behavior. REs can be added during steel production (e.g., Crofer 22 APU) or applied as coatings (discussed in section 5.4). While the exact mechanisms by which reactive elements affect scale growth are still debated, several observations are widely accepted: (i) oxide scale adherence is dramatically improved, (ii) the oxidation rate is reduced, (iii) Cr_2O_3 scales exhibit a fine-grained microstructure, and (iv) tracer isotope studies suggest that cation transport in the oxide scale is inhibited, leading to a growth mechanism dominated by inward oxygen transport. For a more in-depth discussion, interested readers are referred to references [84–86].

3.2. Commercial steel grades

A handful of steel grades are commonly suggested as interconnect materials. In the SOC literature designations rather inconsistently mix trade names and standards. Below is a list of commercial steels that were mostly developed for SOC interconnect applications.

- Crofer 22 APU was developed jointly by Forschungszentrum Jülich and VDM and is widely regarded as the first steel grade engineered specifically for SOFC interconnect applications. The very low Si and Al concentration, combined with La addition, resulted in excellent oxidation resistance and an adherent oxide scale. However, these compositional requirements result in high production costs and the material has limited creep resistance.
- Crofer 22 H is a successor of Crofer 22 APU. It forms Laves phases which resulted in much higher creep strength to address the creep limitation on Crofer 22 APU. Moreover, the Laves phases bind Si which enables higher tolerance for Si which results in lower production costs.
- Sanergy HT was the designation of a steel grade developed by Sandvik Materials Technology. It was discontinued around 2012. Now the name refers to a protective coating developed by Alleima (former Sandvik Materials Technology).
- ZMG232 is a 22 wt% Cr steel developed by Hitachi Metals (now Proterial) with a focus on Zr doping along with La. It exists in different versions in addition to ZMG232, ZMG232L [87] (low Si and Al), ZMG232G10 [18] (higher Cr, W and Cu). ZMG232G10 is the currently available version of this steel. There are few recent publications on this material.
- 460 FC was developed by POSCO and is produced by Vacuum Oxygen Decarburization, without RE elements. Limited studies showed similar performance to Crofer 22 APU [88], however, published long-term performance data remain more limited compared with well-established alloys such as Crofer 22 APU.
- E-Brite [89] was developed in the 1970 s as a high Cr ferritic steel (26 wt% Cr) for the chemical process industry. It has been proposed as interconnect material in the early 2000s but interest seems to have subsided. Because of the low concentration of Mn, the Cr(VI) evaporation is considerably higher than Crofer 22 APU or other Mn containing alloys [13]. Furthermore, due to the high Cr content there is a risk for σ phase embrittlement.
- Therma22FC [90] is a recently developed alloy from Outokumpu specifically for SOFC and SOEC interconnect application. According to Outokumpu, it is a 21 wt% Cr steel stabilized with Ti and Nb and containing Cu and V. It is reported to have good creep resistance and corrosion performance in dual oxidizing and reducing atmospheres. No data is available yet in scientific literature about the performance of the alloy.
- JFE-FC1 [91] was announced by JFE steel in 2025. According to JFE it forms a "unique oxide scale" that makes the protective coating redundant. Currently, there is no independent confirmation of this claim with no scientific studies in the literature.

Apart from these steels known under their trade names several 400 series steels have been proposed for interconnect applications, in particular AISI 441, AISI 444 and AISI 430. Table 2 provides an overview of the most common materials and their respective compositions.

In terms of corrosion resistance, high-Cr ferritic stainless steels with reactive element (RE) additions, such as Crofer 22 APU, provide the highest performance. Crofer 22 APU remains the benchmark FSS interconnect material, with stable operation demonstrated in stack tests exceeding 40,000 h. In contrast, long-term oxidation and performance data for AISI 441 are scarce in the open literature, as much of the testing conducted by industrial stakeholders remains proprietary. The long-term degradation of FSS interconnects is governed by the continuous growth of the protective chromia-spinel scale. However, the ultimate lifetime limitation is

Table 2
Chemical composition of commonly suggested interconnect steels in wt%. Instead of providing nominal compositions which typically are rather broad, a specific composition found in the literature is given.

Name	EN	C	Cr	Mn	Si	Nb	Mo/W	Ti	RE	others	Reference
Crofer 22 APU	1.4760	0.004	22.9	0.38	0.01	–	–	0.06	0.07 La	–	[92]
Crofer 22 H	1.4755	–	23.0	0.44	0.25	0.5	1.9 W	0.1	0.07 La	–	[93]
ZMG232	N/A	0.02	21.97	0.50	0.40	–			0.22 Zr 0.04 La	0.21 Al	[94]
ZMG232G10	N/A	0.02	24.0	0.30	0.10	–	2.0 W		0.25 Zr 0.06 La	1 Cu 0.1 Al	[18]
460 FC	N/A	0.007	22.3	<1	0.09	<0.5	Mo	yes	–	–	[88]
AISI 430	1.4016	0.04	16.2	0.49	0.34	–	–	–	–	–	[92]
AISI 441	1.4509	0.014	17.6	0.35	0.59	0.39	–	0.17	–	–	[92]
AISI 444	1.4521	0.015	19.03	0.35	0.4	0.6	1.86 Mo	0.005	–	–	[92]

often associated with progressive chromium depletion in the substrate. As oxide growth consumes chromium, the local Cr concentration may eventually fall below the critical level required to maintain a protective chromia scale, leading to breakaway oxidation. For operation at 800 °C and above, long-term durability requires a substantial Cr reservoir, which can be enhanced by increasing interconnect thickness, while RE additions suppress oxidation. At temperatures below 700 °C, reduced diffusion distances decrease the importance of the Cr reservoir, further cost savings can be achieved through the omission of RE alloy additions. Under these conditions, steel microstructure and pre-treatment become increasingly important because degradation is governed primarily by processes occurring in the near-surface region. Future interconnect development will not only be driven by oxidation resistance and durability but by factors such as cost, manufacturability in large volumes, coating compatibility, and large-scale industrial implementation. As a result, next-generation interconnect materials will require not only optimal technical performance but balanced techno-economic optimization of alloy and coating composition, microstructure and thickness as well as manufacturing routes.

4. Cr(VI) evaporation

4.1. General remarks

Metallic interconnects made from FSS readily oxidize under high pO_2 atmospheres, resulting in the formation of an oxide scale. The formation of a dense and protective Cr_2O_3 oxide scale is desired to prevent the material from rapid oxidation; nevertheless, its continuous growth increases the ohmic resistance of the interconnect. An additional degradation mechanism involves the interaction of the chromia scale with the air-side atmosphere, resulting in Cr(VI) evaporation as shown in the following equations Eq. (6), Eq. (7).

$$Cr_2O_3(s) + \frac{3}{2}O_2(g) \rightarrow 2CrO_3(g) \tag{6}$$

$$Cr_2O_3(s) + \frac{3}{2}O_2(g) + 2H_2O(g) \rightarrow 2CrO_2(OH)_2(g) \tag{7}$$

While other volatile Cr(VI) species exist, these are the most important formation reactions. The formation of CrO_3 as shown in Eq. (6) is mainly relevant above 1000 °C. Eq. (7) in contrast requires the presence of H_2O, as Cr(VI) evaporation also occurs through the formation of oxy-hydroxides which is particularly relevant in SOFC conditions. Chromium evaporation has two consequences: it can poison the air electrode, thereby degrading stack performance, and it depletes the chromium content of the FSS alloy, which can trigger catastrophic oxidation involving the accelerated formation of non-protective iron oxides.

To mitigate the degradation from the above processes, specialty steels such as Crofer 22 APU were developed for interconnect applications. While these alloys demonstrate improved performance via reduced chromia scale growth and chromium evaporation, they remain insufficient for achieving the long-term operational stability required for SOC stacks. To further address these challenges, coatings are often employed. Coatings serve several critical functions on FSS interconnects by reducing the chromia scale growth, suppressing chromium evaporation, and lowering the ohmic resistance increase, thereby increasing the material compatibility and the lifetime of the metallic interconnects. These aspects will be discussed in more detail in the following sections.

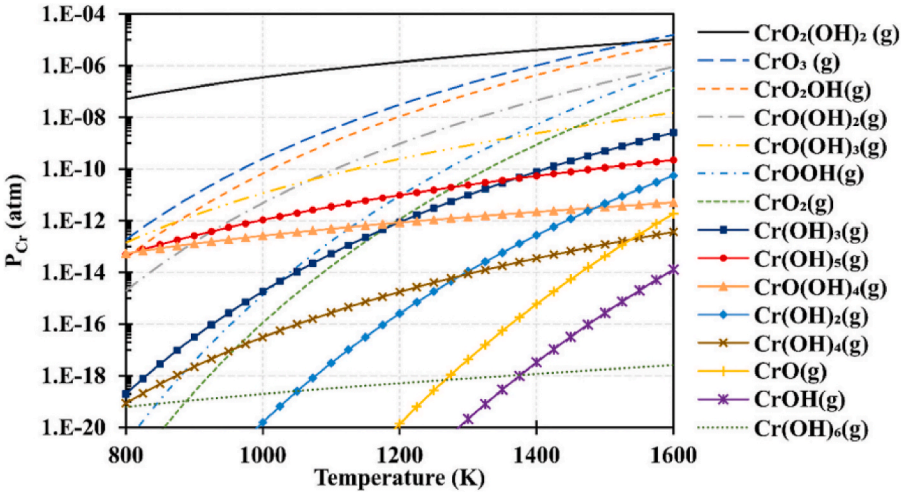

Fig. 5. Thermodynamic equilibrium partial pressures of chromium-containing gaseous species above Cr_2O_3 as a function of temperature in humid air ($pO_2 = 0.21$ atm, $pH_2O = 0.03$ atm). The predominance of $CrO_2(OH)_2$ at SOC-relevant temperatures explains the strong influence of water vapor on chromium volatilization. Reprinted with permission from [101].

4.2. Cr(VI) evaporation and poisoning

Several Cr(VI) species can form during the interaction of the Cr_2O_3 scale with O_2 and H_2O as shown in Fig. 5. Cr(VI) evaporation is affected by various factors such as temperature, humidity, gas flow rate, and the orientation of the sample with respect to the flow direction. From a thermodynamic perspective, Cr(VI) evaporation is promoted by higher partial pressures of H_2O or O_2. Falk-Windisch et al. [31] reported that the activation energy for chromium evaporation from FSS (85–95 kJ mol^{-1}) is approximately three times lower than that for oxidation (250–280 kJ mol^{-1}), indicating an increased influence of Cr(VI) evaporation at lower temperatures. For typical SOC operating temperatures and in the presence of H_2O, $CrO_2(OH)_2$ is the dominant volatile Cr(VI) species while the formation of CrO_3, is mostly relevant above 1000 °C. At 850 °C $CrO_2(OH)_2$ will be more abundant than CrO_3 if $p(H_2O)$ is above 1 mbar [95]. More detailed information on the effect of different factors on chromium evaporation can be found here [96–99]. Several methods such as traditional condensation-based collectors [100], quartz wool collectors [99] and denuder-based techniques [30] have been proposed to measure chromium evaporation with varying degrees of collection efficiency.

Cr poisoning has been one of the major challenges to the commercialization of the current SOFC technology relying on metallic interconnects. Cr(VI) volatile species, originating from the chromia scale on the interconnect, are deposited on the air electrode as shown in Eq. (8) and (9). They block the active triple-phase boundaries (TPBs), hindering the oxygen reduction reaction.

$$CrO_3(g) + 3e^- \rightarrow \frac{1}{2}Cr_2O_3(s) + \frac{3}{2}O^{2-} \quad (8)$$

$$CrO_2(OH)_2(g) + 3e^- \rightarrow \frac{1}{2}Cr_2O_3(s) + H_2O(g) + \frac{3}{2}O^{2-} \quad (9)$$

As a result, the electrochemical activity of the electrode is reduced, leading to the degradation of SOC performance over time. This process is commonly known as chromium poisoning. In addition to the direct blocking of TPBs by Cr_2O_3, Sr-doped air electrodes such as $La_{1-x}Sr_xCoO_3$ are usually prone to Sr segregation at the surface where they can react with volatile Cr(VI) species resulting in the formation of $SrCrO_4$ [102] thereby causing the degradation of the air electrode and increasing the area specific resistance. Numerous papers have been written on these topics, and the reader is referred to [103–107] for further details.

In addition to chromium poisoning, chromium evaporation is also detrimental because it depletes the FSS of Cr. When the subsurface Cr concentration falls below the critical level to sustain chromia scale formation, the alloy undergoes breakaway corrosion, characterized by the accelerated formation of non-protective, iron-rich oxides. The higher activation energy for Cr diffusion in the steel (210 kJ mol^{-1}) results in the bulk diffusion process slowing substantially and becoming the rate-limiting step for replenishing Cr at the surface, while the rate of chromium evaporation remains comparatively high due to its lower activation energy [31,47]. This exacerbates this issue at lower temperatures.

4.2.1. Cr(VI) evaporation in SOEC

The reaction at the air electrode differs between SOEC and SOFC, where oxidation happens in the former (O^{2-} is converted into O_2) while reduction (O_2 transforms into O^{2-}) happens in the latter. This polarization favors the $CrO_2(OH)_2$ reduction reaction (i.e. deposition) in SOFC mode while in SOEC mode the reduction of Cr(VI) to lower valency states such as Cr(III) is less favorable. Thus, Cr(VI) deposition at TPB-sites will be more preferred in SOFC, where the oxygen reduction reaction competes with the Cr(VI) reduction. So, Cr(VI) reduction is not thermodynamically favored in SOEC. In fact, operating a poisoned air electrode in SOEC mode provided electrochemical cleaning of TPBs [107,108]. However, chromium poisoning could still be a significant problem as Cr can diffuse by

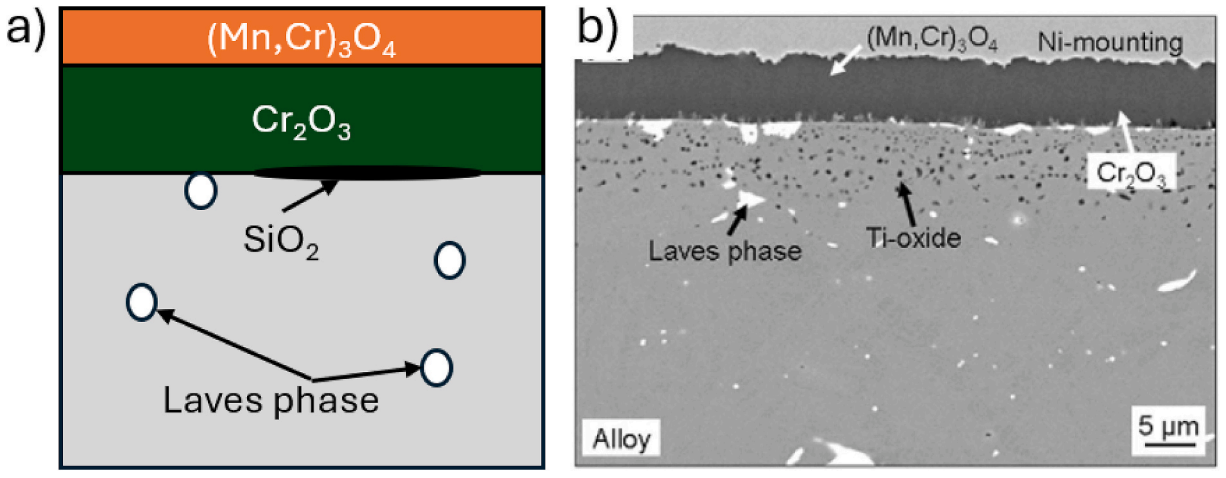

Fig. 6. (a) Schematic of a typical oxide scale formed on the interconnect in air, (b) backscattered electron image of the oxide scale of Crofer 22 H formed after 10 000 h in air at 800 °C. Reprinted with permission from Niewolak et al. [17].

solid state diffusion from the interconnect to the air electrode to interact and form undesirable species such as $SrCrO_4$ [101,104].

There are also operational reasons why chromium evaporation is considered to be of greater significance in SOFCs compared to the SOECs: The electrolysis reaction is endothermic and does not require cooling. This contrasts with SOFCs which require large volumes of air for cooling. In SOECs, however, no inlet is formally required on the oxygen side, although most stacks will have a sweep gas inlet to avoid the buildup of pure O_2 for safety reasons. The much lower volume required allows for the use of dried air to mitigate chromium evaporation. As seen from Eq. (7) H_2O is required to form $CrO_2(OH)_2$ and in its absence the volatilization of Cr_2O_3 is suppressed because CrO_3 has a significantly lower vapor pressure. The lower flow rate will further reduce the overall chromium loss. However, it is important to consider that hydrogen produced at the fuel electrode may leak to the air side, potentially increasing $p(H_2O)$ and accelerating chromium evaporation.

5. Oxide scale formation – oxygen side

Most FSS used for SOC interconnects contain Mn. When exposed to air, these steels commonly form a double layered oxide scale composed of an outer $(Cr,Mn)_3O_4$ layer and an inner Cr_2O_3 layer. This is shown schematically as well as by an example of Crofer 22 H after 10,000 h in Fig. 6. Cr_2O_3 and $(Cr,Mn)_3O_4$ are the main oxides forming initially on interconnect steels, the latter present as a cap layer [17]. Formation of $(Cr,Mn)_3O_4$ cap layer is thermodynamically feasible and growth of this layer occurs through grain boundary diffusion of Mn through Cr_2O_3 grain boundaries [109]. At 800 °C, the electrical conductivity of $(Cr,Mn)_3O_4$ spinel (4×10^{-3} – 0.9 S cm^{-1} [110] depending on Mn/Cr ratio) is commonly suggested to be higher than chromia (0.001 and 0.05 S cm^{-1}) [81,111–113]. The significant variation in literature values for the conductivity of chromia is likely due to factors such as impurity incorporation, oxygen gradients, temperature effects, and scale doping.

5.1. Oxidation above 800 °C

Investigations into the high-temperature oxidation of FSS for interconnect applications typically show a positive mass gain above 800 °C, attributed to the growth of a protective oxide scale. Simultaneously, Cr(VI) evaporation causes mass loss under these conditions. Due to the weaker temperature dependence of the evaporation reaction its relative importance increases at lower temperatures. Although not negligible the mass loss due to Cr(VI) evaporation is generally considered less significant at higher temperatures. For example, Sachitanand et al. [13] reported that after 1000 h at 850 °C in air containing 3% H_2O, the mass gain from oxidation was 1.41 mg/cm^2, while the mass loss (Cr_2O_3) from chromium evaporation was only 0.25 mg/cm^2. In low manganese FSS such as E-brite, however, the effect of chromium evaporation becomes more pronounced. This is because these alloys cannot form a continuous $(Cr,Mn)_3O_4$ spinel phase. Hence, significant Cr(VI) evaporation is observed on that material.

The high-temperature stability of ferritic stainless steels is critically dependent on the suppression of the detrimental austenite phase, a role fulfilled by strong ferrite-stabilizing elements like Cr, Ti, Si, Nb, and Mo. Chyrkin et al. [22,24] showed that stabilized alloys (e.g., Crofer 22 H, Fe-18Cr-2Mo) had extended lifetime at 900 °C in contrast with their counterparts, Crofer 22 APU and Fe-18Cr that are more prone to form austenite once Cr is depleted. Similarly, unstabilized AISI 430 (16 wt% Cr) has undergone breakaway corrosion before AISI 409 (11 wt% Cr) at 850 °C [114]. Although this stabilization is essential for preventing accelerated corrosion above ~ 850 °C it is not relevant below because austenite formation is thermodynamically not favored for Fe-Cr alloys at lower temperatures.

5.2. Oxidation below 800 °C

Most research on the oxidation of FSS has historically focused on temperatures of 800 °C and higher. Recently, however, rapid advancements in intermediate-temperature solid oxide cells (IT-SOCs) have spurred increased interest in the performance of these steels between 600–700 °C. Due to the higher activation energy of chromia scale growth compared to chromium evaporation, chromium evaporation exerts a disproportionate influence on mass gains under 800 °C with a pronounced effect as temperature decreases. This results in the parabolic oxidation rate constant becoming irrelevant as mass loss by chromium evaporation can be higher than the mass gain by chromia scale formation. This results in non-parabolic kinetics and mass gains being highly dependent on gas flow rate and $p(H_2O)$. Several FSS alloys, including AISI 441, Sanergy HT, and Crofer 22 H, showed a net mass loss (paralinear oxidation) at 750 °C, 650 °C, and 600 °C. These alloys showed an initial mass gain followed by continuous mass loss. Furthermore, the formation of a continuous, protective $(Cr,Mn)_3O_4$ spinel layer is kinetically hindered due to slower cation diffusion. This delay is evident in the chromium evaporation rate, which fails to reach a steady state even after 500 h of exposure. This phenomenon is particularly common in FSS grades that contain a higher volume fraction of Laves phase precipitates, such as AISI 444 and Sanergy HT.

5.3. Oxide scale adherence and lifetime

The long-term stability of chromia scales may be compromised by oxide spallation. Oxide scale spallation is usually stress induced and occurs when the oxide scale reaches a critical thickness. Thus, it is mostly an issue for interconnects operating at higher temperatures. Scale spallation can also be induced by silicon impurities in the steel that form an insulating silica subscale. The thermal expansion mismatch between this subscale and steel introduces interfacial stresses triggering spallation. Furthermore, Cr_2O_3 scale growth is predominantly controlled by outward chromium diffusion, which creates voids at the metal/scale interface, degrading adhesion which may lead to eventual delamination and contact loss. The “reactive element effect” is a critical strategy for improving

the high-temperature oxidation resistance of chromia-forming alloys. The incorporation of reactive elements like Lanthanum (La) drastically improves oxide scale adhesion. It is commonly suggested that reactive elements suppress outward Cr diffusion (see section 5.4). This reduces the overall growth rate and hence reduces stresses and suppresses pore formation at the metal oxide interface.

The reactive element effect can be produced by a wide variety of reactive element addition methods, such as microalloying, dispersion of oxides and surface coatings with a thin layer of the reactive element oxide. Mikkelsen [115] showed that the oxidation rate of Fe-22Cr is significantly reduced by addition of 0.3 wt% Ce to the steel. Typically, reactive elements were added to steels specifically tailored for the interconnect applications such as Crofer 22 APU or Crofer 22 H. In addition to the presence of reactive elements in the steel such as Crofer 22 APU, several authors showed an improvement in the oxidation behavior in the presence of reactive elements added in the form of a coating [11,116,117]. Similar results of reduced oxidation kinetics are observed on Sanergy HT [12] and AISI 441 [118,119].

The formation of a continuous, protective chromia scale on FSS interconnects requires a Cr content of at least 15–20 wt% under SOC conditions. The service lifetime of these components is also limited by Cr depletion, which is caused by scale growth and Cr(VI) evaporation, leading to breakaway oxidation. The dominant depletion mechanisms are temperature dependent. Above 800 °C, rapid bulk diffusion in the bcc lattice replenishes the Cr consumed by initial scale formation and subsequent evaporation, making the lifetime dependent on the total Cr reservoir (Cr content and thickness). Conversely, at lower temperatures, Cr diffusion is orders of magnitude slower, preventing effective replenishment of the subsurface. In this regime, where Cr(VI) evaporation is the dominant consumption factor, the interconnect's lifetime is primarily determined by its initial Cr content and microstructure governing fast diffusion paths rather than its thickness.

5.4. Coatings in air

Despite the improvements to limit the degradation in high pO_2 conditions – such as adding Mn to reduce Cr(VI) evaporation and incorporating reactive elements to reduce oxide scale growth and ASR, it is apparent that coatings are needed for long-term operation of SOCs. Coatings have been extensively investigated for interconnects in solid oxide cells to enhance their performance and longevity. The selection criteria for coatings are similar to those for the interconnects, such as a CTE similar to the other cell components, good electrical conductivity, ease of manufacturing, chemical compatibility with adjacent cell components, good adhesion, and low cost. Historically, the primary purpose of the coating was to inhibit Cr(VI) evaporation. The various coatings proposed in the literature can be broadly divided into two main groups: spinel-based coatings and perovskite-based coatings. Although perovskite based coatings are found to have excellent electrical conductivity and matching coefficients of thermal expansion (CTE) with other SOFC components, they are found to be less effective in preventing Cr(VI) evaporation [120]. Spinel-based coatings offer enhanced thermal stability, electrical conductivity, and chemical stability, making them the preferred choice over perovskite-based coatings for SOFC interconnects. With respect to spinel type coatings, $(Co,Mn)_3O_4$, $(Cu,Mn)_3O_4$, and $(Ni,Fe)_3O_4$ based spinels with various dopants are most commonly researched for this application. Due to their compositional versatility and compatibility with cost-effective, scalable

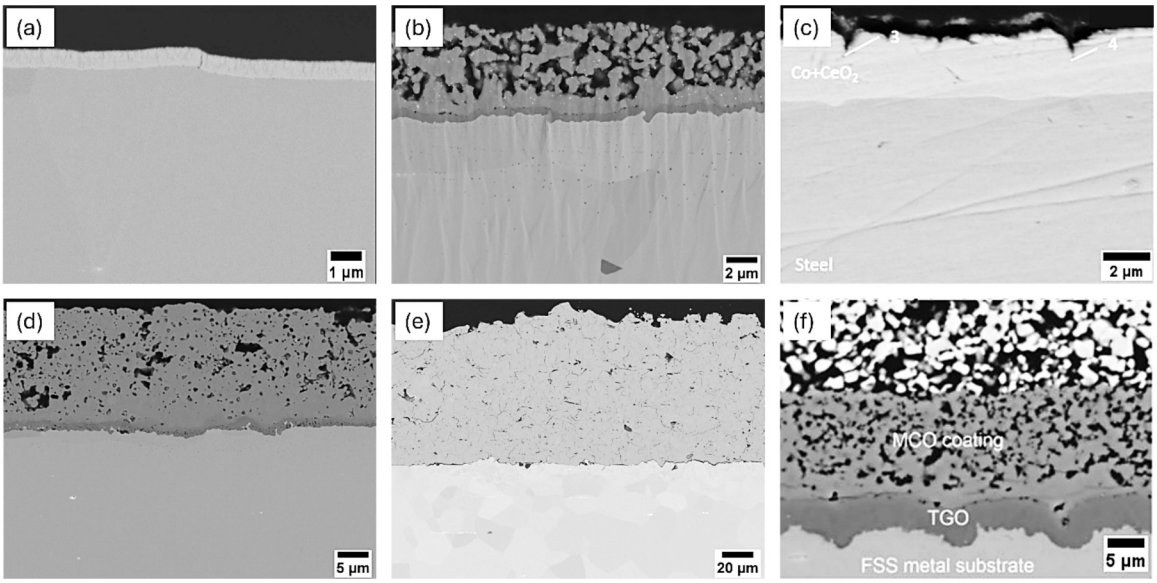

Fig. 7. Cross-sectional SEM images of Crofer 22 APU coated by (a) physical vapour deposition (PVD), (b) ultrasonic spray coating (USC), (c) electroplating (EP), (d) electrophoretic deposition (EPD), and (e) atmospheric plasma spraying (APS) in the as-received condition. (f) Air-side cross-section of an interconnect after 40,000 h of service in a SOFC stack. The images highlight the strong influence of deposition method on coating thickness, porosity, and morphology despite similar coating chemistry. Note that the micrographs are presented at different magnifications. Reprinted with permissions from [149–151].

synthesis techniques, spinel coatings are highly attractive candidates for interconnect protection. Such coatings are deposited using various methods, such as physical vapor deposition (PVD) [32,121–124], sol–gel dip-coating [125–128], electrophoretic deposition (EPD) [129–132], electroplating [133,134], screen printing [135,136], spray pyrolysis [137–139], inkjet printing [140,141], thermal co-evaporation [142,143] and atmospheric plasma spraying (APS) [144–148]. The diversity of application methods for chemically similar spinel-based coatings is illustrated in Fig. 7a–f, which compares cross-sectional SEM micrographs of Crofer 22 APU coated by PVD, ultrasonic spray coating, electroplating, EPD, and APS in the as-received condition [149–151]. These images highlight how the selected deposition technique strongly influences coating morphology, thickness, uniformity, and porosity. For more information on the coating application methods, refer to the review papers [152–155] which focus on coatings.

The ability of the coating to inhibit chromium evaporation is the most important parameter for determining the effectiveness of a coating. Nevertheless, very few publications have performed tests in flowing air that have directly quantified chromium evaporation. Most studies evaluate Cr(VI) evaporation behavior by measuring the Cr concentration with post-mortem cross-sectional and compositional analysis at the coating-air interface, thereby predicting coating effectiveness. Some studies perform cell tests by exposing solid oxide fuel cells directly to coated or uncoated interconnects in humidified flowing air to benchmark electrochemical performance degradation and analyze post-mortem cathode surface changes [156]. Reddy et al. [149] investigated in a comparative study the chromium evaporation behavior of several coatings developed at eight different research institutions. Most coatings, based on $(Co,Mn)_3O_4$ spinels, exhibited similar chromium evaporation, which is about 20–100 times lower than the uncoated steel after 500 h. These results firmly establish the efficacy of $(Co,Mn)_3O_4$ spinel coatings in suppressing chromium volatilization. More data on the chromium evaporation of different alloys (coated and uncoated) could be found in [149,157].

More recently, the effect of coatings to reduce the Cr_2O_3 scale growth thereby limiting the increase in ASR has been studied. Several coatings deposited using wet deposition processes such as electrophoretic deposition reported reduced oxide scale growth in the presence of $(Co,Mn)_3O_4$ (MCO) coatings [158]. However, almost all the coatings were subjected to reduction and oxidation treatment at temperatures higher than the exposure temperatures to improve the coating density (coating densification), which could have an impact on the oxidation kinetics of the coated steels. On the other hand, Froitzheim et al. [159] showed that 600 nm of Co coating, which rapidly converts to spinel, decreased chromium evaporation significantly compared to the uncoated steel but did not affect the chromia scale growth rate substantially. Fontana et al. [11] performed exposures for up to 30 months on reactive element oxide coated Crofer 22 APU, which showed significantly thinner oxide scale and lower area specific resistance compared to the uncoated Crofer 22 APU. However, reactive element coatings were shown to be ineffective in reducing the chromium evaporation [118] and thicker layers would increase electrical resistance. The combination of reactive elements with $(Co,Mn)_3O_4$, was shown to be effective to reduce chromia scale growth and chromium evaporation [12]. The steel coated with a combination of a 10 nm Ce and 640 nm Co coating, showed significantly lower chromia scale growth compared to the 640 nm Co-coated steel as shown in Fig. 8 [159,160]. The slower chromia scale growth on the Ce/Co coated steel is attributed to the 10 nm Ce layer. Increasing the thickness of Ce from 10 nm to 50 nm did not reduce chromia scale growth further [114]. Significant research has been focused towards improving the conductivity of the spinels to reduce the ASR [132,138,161–163]. For example, doping the $(Co,Mn)_3O_4$ spinels with Fe, Cu has been commonly employed to improve the conductivity. Goebel et al. [164] questioned whether the conductivity of the coating is that important because the chromia scale has several orders of magnitude lower conductivity than the coating. If the thermally grown chromia scale and the coating are interpreted as two resistors connected in series, the effect of the coating conductivity is expected to be negligible except for

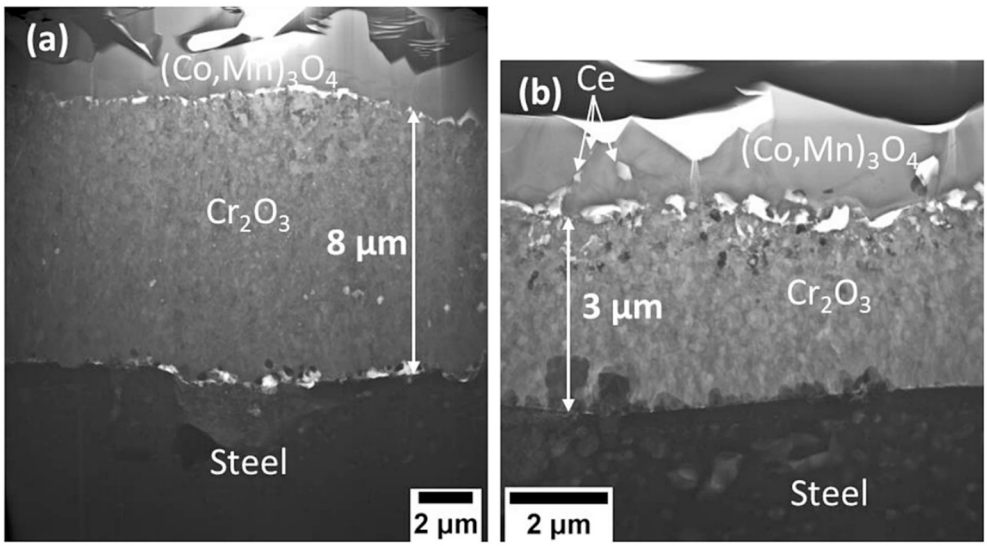

Fig. 8. TEM bright field images of (a) Co coated and (b) Ce/Co coated Fe-22Cr steel exposed at 850 °C for 3000 h. The addition of Ce significantly reduces chromia-scale thickness, illustrating the reactive element effect. Note the higher magnification on the right image. Reprinted with permission from [159,160].

extreme cases. This argument was further corroborated by Reddy et al. [149] who reported that coated steels exposed for 3000 h at 800 °C exhibited highly similar ASR values even though the coating thicknesses varied by a factor of 100. Nevertheless, a highly conductive surface layer might be beneficial in real stack operation: with contact points towards the electrode being spaced widely apart from each other. In such a scenario a coating provides a high conductivity path on the interconnect surface so that the effective contact area becomes larger.

During the high-temperature operation, an intermediate "reaction zone" or reaction layer frequently forms at the interface between the Cr_2O_3 scale and the spinel coating. The Cr diffuses into the coating and incorporates into the spinel lattice forming $(Co,Mn,Cr)_3O_4$ phase. This phenomenon is particularly common when a high temperature coating densification step has been performed [132,165,166] as seen in Fig. 7a-f. Sustained Cr incorporation alters the defect chemistry and cation distribution of the spinel over long-term exposure and could decrease the concentration of active charge carriers, increasing the ASR. One study proposed that pre-oxidation prior to coating deposition resulted in no spinel reaction zone even after coating densification treatment at 800 °C [167]. Other studies suggested application of diffusion barriers such as CeO_2 [168] and NiO [169].

Long-term evaluation of MCO coatings on the air side spanned about 40,000 h, testing performance both in a laboratory stagnant air furnace at 800 °C [32] and under actual SOFC operating conditions at a nominal temperature of 850 °C [151]. Fig. 7f shows a cross-section of the coated interconnect after 40,000 h stack operation. The analysis indicates that chromium migrates into the coating over time, forming an intermediate reaction layer between the coating and the Cr_2O_3 scale. However, no Cr was detected within the contact layer, confirming the protective efficacy of the coating. Furthermore, the chromia scale thickness remained similar between the rib (with electrical contact) and the gas channel (without electrical contact) regions, suggesting that current polarization had a negligible effect; however, variations were observed between the inlet and outlet due to temperature gradients.

While $(Co,Mn)_3O_4$ spinel coatings have demonstrated excellent performance, the toxicity and critical status of cobalt necessitate the exploration of cobalt-free options like $(Cu,Mn)_3O_4$ and $(Fe,Ni)_3O_4$, which is crucial for long-term sustainability and economic viability. $(Cu,Mn)_3O_4$ offers high electrical conductivity [170], similar CTE to other SOFC components and lower densification temperature. However, the primary limitations of this coating include long-term structural instability and its high reactivity with Cr_2O_3, resulting in higher Cr(VI) evaporation. The coating is ineffective in suppressing chromium evaporation above 750 °C whereas promising results have been reported at 650 °C, suggesting greater suitability for low temperature applications [149,171]. The stability of the $(Cu,Mn)_3O_4$ is reported to increase with the addition of Ni [172] and Fe [139,156,172,173]. $CuMn_{1.7}Fe_{0.3}O_4$ composition demonstrated exceptional long-term stability after 10,000 h at 750 °C outperforming state of the art Co–Mn spinels [156]. $(Fe,Ni)_3O_4$ spinel has lower conductivity [170] than $(Co,Mn)_3O_4$ and demonstrates less efficacy in preventing Cr(VI) evaporation [114], probably because of interdiffusion between chromia and spinel. However, $(Fe,Ni)_3O_4$ spinel coatings showed lower chromia scale growth compared to $(Co,Mn)_3O_4$. Although existing coatings effectively suppress chromium evaporation and chromia scale growth, they usually fail to prevent the formation of a SiO_2 subscale. For cost reduction, coated commercial steels like AISI 441 and 444 are viable alternatives, demonstrating performance comparable to coated Crofer 22 APU in lab studies [92]. While the addition of Nb and Mo to these steels is intended to reduce Si subscale formation by binding Si in laves phases [174], precise control during large-scale manufacturing remains a challenge. As a mitigation strategy, Cavichiolo et al. [175,176] have applied a nickel coating that diffuses into the steel, inducing a subsurface transformation into an austenitic phase. This treatment promotes the internal oxidation of silicon, thereby inhibiting the formation of a continuous SiO_2 subscale. However, as nickel continues to diffuse deeper into the steel, this austenitic region eventually reverts to a ferritic phase [176].

5.5. SOEC vs SOFC – oxygen side

A significant difference in oxygen partial pressure exists on the oxygen side of the interconnect between SOEC and SOFC operational modes. In SOEC mode, the evolution of oxygen at the air electrode results in exposure of the interconnect to nearly pure oxygen if no sweep gas is utilized. Conversely, in SOFC mode, high air flow rates maintain a relatively constant oxygen partial pressure, approximately that of air ($pO_2 \approx 0.21$ bar). This fundamental difference brings into question the validity of extrapolating oxidation data obtained under SOFC air-side conditions to predict the behavior of the interconnect on the air side during SOEC operation. Furthermore, there is a trend in SOEC development towards pressurized operation, the influence of pressure on oxidation remains poorly understood due to significant experimental challenges and a scarcity of published data.

The dependence of the FSS oxidation rate on oxygen partial pressure (pO_2) is debated, as it dictates the defect chemistry of the chromia scale. According to fundamental studies, the oxidation rate is expected to increase with pO_2 if the defect structure is dominated by cation vacancies while the oxidation rate should be independent of pO_2 if interstitial cations are the dominant defects [177]. In practice, this relationship is complicated by the presence of the spinel layer as well as several impurities in the steel which can influence the defect structure.

Studies on elevated pressure in air/O_2 on FSS do not exist to the authors' knowledge. However, experiments reducing $p(O_2)$ showed only a minimal impact of $p(O_2)$ on the oxidation kinetics. Alnegren et al. [95] investigated the oxidation of uncoated ferritic steels (17–22% Cr) at 850 °C, over a pO_2 range of $10^{-4} - 1$ bar. Their findings showed that the oxidation rates were largely independent of the oxygen partial pressure. Palcut et al. [178] observed a minimal dependence of oxide scale growth on oxygen partial pressure. Schmucker et al. [179] investigated the oxide growth rate of Ni-30Cr alloys between 10^{-13}- 10^{-3} bar O_2 pressure at 1150 °C and reported that growth rates were independent of pO_2. These observations make sense from a thermodynamic perspective: Although changes in oxygen activity might affect defect equilibria to some extent, the underlying driving force for Cr_2O_3 scale growth is the oxygen activity gradient between the metal oxide interface ($p(O_2) \sim 10^{-30}$ bar) and the surface ($p(O_2) = 0.2$ bar). An increase by a few bars should not change this gradient in a meaningful manner.

Since no cooling air is required, in ideal operation the SOEC oxygen side is completely dry so that the formation of $CrO_2(OH)_2$ is suppressed, and Cr(VI) evaporation is expected to be negligible which questions the requirement of a coating. However, several factors must be considered. Foremost, potential hydrogen leakage from the fuel electrode can increase oxygen-side humidity. Furthermore, a protective coating can reduce oxide scale growth or inhibit detrimental reactions with the contact paste, and the electrode material. Therefore, protective coatings are still required to ensure stability during high pO_2 SOEC operation. In summary, SOEC coating design might give Cr(VI) evaporation characteristics a lower priority while a reduction of oxide scale growth is expected to remain a critical issue.

6. Oxide scale formation – H_2/H_2O side

6.1. General remarks

Under SOEC operating conditions, the steam side (cathode) is where water vapor is split into H_2 and O^{2-}. The latter is transported to the air side through the electrolyte. CO_2 or $CO_2 + H_2O$ can also be electrolyzed by SOEC to form CO or $CO + H_2$ which may lead to additional degradation mechanisms such as carburization [180,181]. Nevertheless, this review focuses on steam electrolysis. Usually, the gas fed to the steam side contains a small amount of hydrogen ($H_2/H_2O \approx 0.1$). The primary purpose for this hydrogen recirculation is to prevent the oxidation of Ni, used as a catalyst and conductive mesh. These atmospheres containing both H_2 and H_2O are commonly expressed as H_2/H_2O. The pO_2 of such gas is determined by the temperature and the ratio of H_2/H_2O.

This gas mixture is analogous to the fuel side of the SOFC, with a few key differences. The inlet of the SOFC is relatively dry and rich in H_2 (low steam concentration) while the outlet is enriched in steam due to formation of water vapor. In case of SOEC the situation is reversed. The outlet is rich in H_2 due to electrolysis of water vapor while the inlet is rich in steam. SOEC inlet conditions are expected to have higher humidity than SOFC outlet conditions. Consequently, from a high temperature oxidation perspective, SOEC operation is expected to be more challenging due to the higher water vapor concentration at the inlet.

Although the oxidation of Ni is prevented by recirculating some H_2 in case of steam electrolysis, the interconnect still spontaneously oxidizes in these conditions. Because Cr_2O_3, $(Cr,Mn)_3O_4$, and depending on H_2/H_2O ratio and temperature, Fe_3O_4 or FeO will be thermodynamically stable in such gas. Table 3 gives an overview of equilibrium oxygen partial pressures and dissociation pressures of relevant oxides under typical SOEC conditions [10]. Due to the very low pO_2, in H_2/H_2O environments Cr(VI) evaporation is not a concern since the partial pressures of such evaporative Cr-species are insignificantly low [182]. It should be emphasized that most of the studies in H_2/H_2O were carried out in diluted gas mixtures with low water vapor concentrations such as Ar-5%H_2-3%H_2O simulating the inlet of the SOFCs. However, undiluted gases with higher water vapor concentrations, which are most relevant for SOEC inlets typically require more complicated experimental equipment.

As illustrated in Table 3, in most cases pO_2 values are sufficient to oxidize Fe, Cr, and Mn. Therefore, understanding the oxidation mechanism of FSS in H_2/H_2O gas is crucial and relevant for both SOEC and SOFC. Despite exhibiting low pO_2, oxidation of FSS in H_2/H_2O gas is complex. A change in temperature shifts the H_2/H_2O equilibrium and hence has a direct effect on pO_2. Furthermore, gas composition, surface preparation and pre-oxidation greatly affect the oxidation kinetics [19,57,59,183]. Depending on the interplay of these parameters, protective Cr_2O_3/Cr_2MnO_4 duplex scales or fast-growing Fe-rich oxides may form on the surfaces of FSS interconnects. Formation and growth of the latter leads to fast degradation of the FSS interconnect [57,59,184,185]. In contrast to air, due to the low pO_2, Fe_2O_3 is not stable in most H_2/H_2O atmospheres. Hence, Fe_3O_4, FeO and $(Fe,Cr)_3O_4$ phases are observed as Fe-rich oxides in H_2/H_2O environments [57,59,184,185].

6.2. Effect of temperature

Irrespective of the exposure environment temperature has a strong impact on the oxidation behavior of FSS. On the air side the oxidation rate commonly follows simple Arrhenius kinetics while the situation is more complicated on the fuel side. Early SOCs were operating at and above 800 °C, therefore, oxidation studies of interconnect materials have been mostly performed at these

Table 3
Oxygen activity of different H_2/H_2O mixtures and dissociation pressures of relevant metal oxides at 600 and 800 °C.

Species	600 °C	800 °C
$p(H_2)/p(H_2O) = 100$	1.71×10^{-28}	5.38×10^{-23}
$p(H_2)/p(H_2O) = 10$	1.71×10^{-26}	5.38×10^{-21}
$p(H_2)/p(H_2O) = 1$	1.71×10^{-24}	5.38×10^{-19}
$p(H_2)/p(H_2O) = 0.1$	1.71×10^{-22}	5.38×10^{-17}
$p(H_2)/p(H_2O) = 0.01$	1.71×10^{-20}	5.38×10^{-15}
Stability of NiO	5.79×10^{-20}	9.77×10^{-15}
Stability of FeO	1.36×10^{-25}	1.1×10^{-19}
Stability of Fe_3O_4	5.09×10^{-25}	4.69×10^{-18}
Stability of Fe_2O_3	7.04×10^{-16}	2.58×10^{-10}
Stability of Cr_2O_3	1.98×10^{-36}	4.23×10^{-28}
Stability of MnO	1.84×10^{-42}	2.89×10^{-33}

temperatures [50,183,184,186,187]. With the developments in cell design and materials, nowadays the operating temperatures of some SOCs are well below 800 °C [188,189]. Counterintuitively, lower temperatures may lead to a sharp increase in corrosion rate with the most severe corrosion usually observed around 600 °C which is illustrated in Fig. 9 [19,57,190]. At 800 °C, the oxide scales have similar thickness in air and H_2/H_2O while the difference in scale thickness is much larger at 600 °C (about 2 orders of magnitude). Hence, the discussion is separated into temperatures ≥ 800 °C and below 800 °C to disentangle the different mechanisms.

6.2.1. Oxidation at 800 °C and above

According to studies carried out at 800 °C and above, duplex protective scales similar to the air side were commonly reported as Cr_2O_3/Cr_2MnO_4 on steels such as ZMG232, Crofer 22 APU and AISI 441 [15,17,50,59,75]. Yet the morphology of the spinel layer is different and exhibits a plate- or whisker-shaped structure in H_2/H_2O atmosphere [17,50,75]. Furthermore, in such atmospheres Mn only occupies octahedral sites as Mn^{2+} and hence the spinel phase is stoichiometric (Cr_2MnO_4) which is not the case on the air side [17,191]. It is worth noting that despite pO_2 being about 20 orders of magnitude lower, the oxidation rate of interconnect steels is not dramatically different compared to air [15,17,50]. In this context it is important to differentiate between single phase Cr_2O_3 formers and steels that form duplex Cr_2O_3/Cr_2MnO_4 scales. It is well established that single phase Cr_2O_3 formers oxidize faster in H_2/H_2O atmosphere compared to air atmosphere [192]. Furthermore, Cr_2O_3 grows dominantly inwards, forms a finer grained oxide with much better adhesion in H_2/H_2O [193–195]. Additionally, Cr_2O_3 grown in H_2/H_2O is an n-type semiconductor [25]. For further details the reader is referred to the studies in references [25,192–195].

However, unlike single phase Cr_2O_3 formers, the oxidation rates of Mn containing interconnect steels at 800 °C are somewhat lower in H_2/H_2O compared to air [17,50]. Yet dedicated, time resolved studies performed on Crofer 22 APU, Haynes 230 and Ni-Cr-Mn alloys by thermobalance showed that initially these alloys oxidize faster in H_2/H_2O but then the oxidation rate drops after 60–80 h of exposure for steels and 20–30 h for Haynes 230 [17,194,196]. Consistent with this Guillou et al. studied AISI 441 at 800 °C and found that while initial oxidation rates in air and H_2/H_2O were similar the oxidation rate in H_2/H_2O decreased below that in air as the exposure proceeded [197]. This effect is attributed to the formation of a Cr_2MnO_4 cap layer, which limits the transport of hydroxyl groups present in H_2/H_2O atmosphere [17]. It has been suggested that surface coverage with spinel takes longer time compared to air atmosphere since Mn only occupies octahedral sites as Mn^{2+} (Mn^{3+} is a smaller cation hence diffuses faster) which explains why these alloys oxidize faster at the initial stage [17]. Therefore, Mn addition is both beneficial in mitigating the Cr(VI) evaporation in the air side and slowing down the oxidation rate in H_2/H_2O. Yet, Guillou et al. [196,197] reported 1–2 orders of magnitude higher ASR values for oxide scales grown in H_2/H_2O (~1 Ω*cm^2) compared to air (alloy 230 ≈0.01 Ω*cm^2, AISI 441≈ 0.1 Ω*cm^2), although oxidation kinetics were faster in air side for both alloys. The authors related this effect to the proton incorporation into the oxide scale [196,197].

Nonetheless, there are also discrepancies observed at 800 °C. Unlike other studies, Chyrkin et al.[57], Ardigo et al. [183,184,198] and King Jr. et al. [187] reported Fe-rich oxide formation on AISI 441 FSS in H_2/H_2O. Yet, the mass gains compared to a Cr_2O_3/Cr_2MnO_4 were rather similar since a Cr rich layer was present at the metal oxide interface [57]. The reason for this behavior is currently unknown but may be related to differences in transient oxidation during the heating stage of the experiment when the

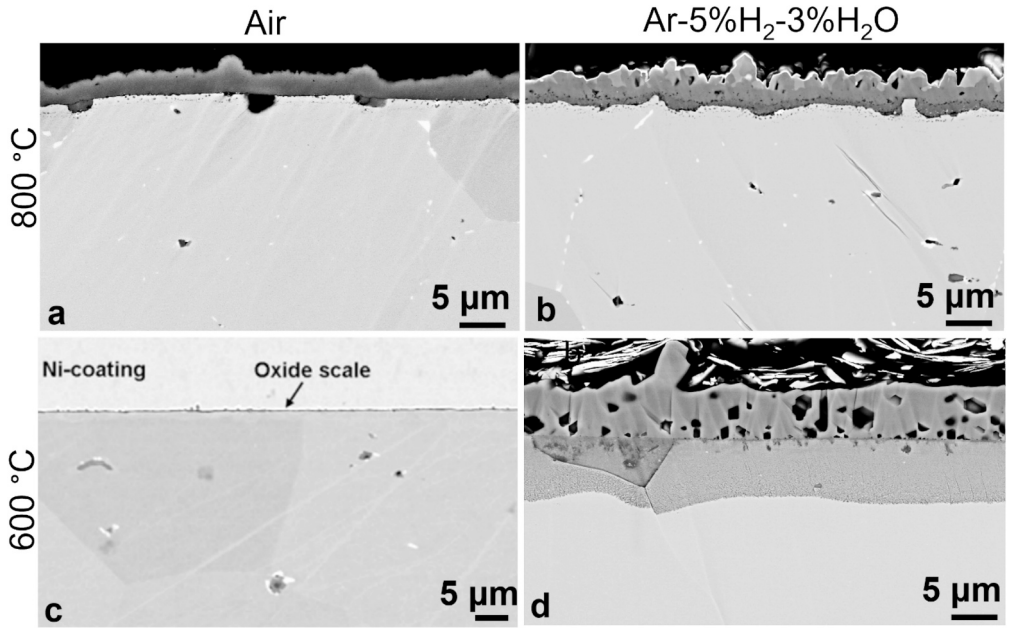

Fig. 9. Oxidation morphologies of AISI 441 under different conditions illustrating the inverse temperature effect observed in H_2/H_2O atmospheres. While protective scales form in air and at 800 °C, severe Fe-rich oxide formation occurs at 600 °C in H_2/H_2O. All micrographs correspond to exposures of 336 h, except panel (c), which corresponds to 1000 h. Reprinted with permissions from [19,57,190].

samples may corrode much faster between 550–700 °C as described in the next section. Indeed, Krogsgaard has found an effect of heating rate on oxidation experiments performed at 800 °C [199]. This is important since it may lead to observations of corrosion phenomena falsely attributed to the experimental conditions that already occur during the heat-up stage.

6.2.2. Oxidation below 800 °C

The trend towards lower operating temperatures is primarily driven by the aim of utilizing cheaper materials and reducing degradation kinetics. However, there are several studies that show dramatically increased corrosion rates in H_2/H_2O in the temperature range 600–700 °C. For instance, AISI 441 exposed at 600 °C for 1000 h formed thin protective scales (≈350-400 nm [19]) in air while very thick Fe-rich oxides (≈ 20–25 μm) were observed in H_2/H_2O atmospheres [57,59].

Young et al. [59] exposed several FSS in Ar-4%H_2-20%H_2O between 500–900 °C including AISI 441 and Crofer 22 APU. For AISI 441, 600 °C is the critical temperature where degradation was most intense. For Crofer 22 APU the most severe corrosion was observed at 550–600 °C while increasing the temperature improved the protectiveness [59]. Chyrkin et al. [57] also investigated the effect of temperature between 550–900 °C on AISI 441 in Ar-5%H_2-3%H_2O and found similar results. Hence, it is clear that in these conditions an inverse temperature relationship is observed with more severe corrosion at lower temperatures as shown in Fig. 9.

6.3. Effect of humidity

Humidity is another important parameter that affects the oxidation behavior. This is especially critical for SOEC conditions where $H_2/H_2O \approx 0.1$ is expected at the inlet. Unfortunately, very limited data are available in such environments. Niewolak et al.[17] demonstrated that increasing the humidity concentration from 2% to 20% at 800 °C did not affect the mass gain for Crofer 22 H. Young et al. [59] obtained similar results. However, at low temperatures (≈ 600–650 °C) the situation is different.

Chyrkin et al. [57] exposed AISI 441 at 600 °C in as-received and pre-oxidized conditions under dry Ar-5%H_2 (900 ppm H_2O), Ar-5%H_2-3%H_2O and Ar-4%H_2-20%H_2O atmospheres for 336 h. In dry Ar-5%H_2 protective behavior was observed irrespective of the pre-oxidation state since only Cr but not Fe can oxidize under these conditions. However, increasing the water vapor concentration to 3% H_2O stabilizes Fe_3O_4 and resulted in complete coverage with Fe-rich oxides on the non-pre-oxidized sample while the pre-oxidized sample remained protective. A further increase of water vapor concentration to 20% H_2O intensified the corrosion attack and the pre-oxidized specimen partially lost its protectiveness. Chen et al. [58] recently investigated Fe-20Cr-x model alloys (x: 0, 1Si, 2Mn, 2Al all in wt%) at 650 °C in Ar-y%H_2-10%H_2O (y: 2, 10, 20%H_2) in a time resolved manner (20–310 h). All alloys exhibited a coarse-grained microstructure due to production by vacuum arc melting. The binary Fe-20Cr alloy failed in all conditions, but the most severe effect was observed in Ar-2%H_2-10%H_2O where H_2/H_2O ratio was lowest. In terms of alloying elements, Mn addition showed little beneficial effect followed by Al. Si addition, on the other hand, suppressed breakaway corrosion by the formation of a SiO_2 underlayer, yet even this alloy failed in Ar-10%H_2O.

6.4. Mechanistic considerations

Over the years, several studies were carried out to explain why widespread breakaway corrosion occurs in H_2/H_2O atmospheres while the same materials form protective scales in air [25,200–206]. Yet there is no general agreement on the exact mechanism responsible for breakaway corrosion in these atmospheres. As outlined in the Fundamentals of High-Temperature Oxidation section Wagner provided the best quantitative description on whether a protective oxide scale can form (Criterion I) and be maintained (Criterion II). The critical input parameters are: Cr diffusion in the steel ($\widetilde{D}_{Fe-Cr}$), oxygen permeability ($N_O^{(s)}D_O$) and the parabolic rate constant (kp). The $N_{Cr}^{(1)}$ value for 600 °C using the bulk transport parameters is around 8 wt% Cr (section 2). This is in agreement with experiments in air where it is generally accepted that 10 wt% Cr is sufficient for external oxide formation. Yet, in H_2/H_2O, steels containing even 18–22 wt% Cr fail [57,59].

In terms of Criterion I H_2/H_2O affects the balance between oxygen permeation and Cr supply expressed as the $\frac{N_O^{(s)}D_O}{\widetilde{D}_{Fe-Cr}}$ ratio to shift it towards the non-protective behavior. The first attempt to rationalize the H_2/H_2O effect in terms of the Wagnerian criteria was undertaken in studies of Essuman et al. [206,207] postulating that hydrogen dissolved in the metal distorts the alloy lattice and thereby increases the oxygen permeability. This conclusion was based on the observation of enhanced internal oxidation in humid gases compared to dry Ar-O_2 and independently supported by [44,208]. The effect of H_2 on oxygen permeability was questioned by many authors and resulted in a series of studies [43,209–213]. All aforementioned studies convincingly demonstrated that hydrogen had no measurable effect on the lattice oxygen permeability especially at higher temperatures. At the same time, the deeper internal oxidation zones (IOZ) observed in [44,203,206–208] and more recently in [23,40] should be attributed to a higher interfacial (i.e. metal grain boundaries or oxide precipitate/matrix interfaces) oxygen permeability in the presence of H_2/H_2O. The latter effect was demonstrated to be specifically strong at lower temperatures [58,214] where transport is dominated by grain boundary (GB) diffusion. At 700 °C, the depth of the IOZ at the steel GBs increases by a factor of two compared to the bulk IOZ [43] and at 600 °C the difference increases to a factor of 4, which implies an increase in $N_O^{(s)}D_O$ by a factor of 16 [215]. Similar GB tails were reported in [216].

Another possible way to affect the $\frac{N_O^{(s)}D_O}{\widetilde{D}_{Cr}}$ ratio for hydrogen is to decrease $\widetilde{D}_{Fe-Cr}$. Ani et al. [208] demonstrated in a diffusion couple experiment that lattice diffusion of Cr in Fe-10Cr was not affected by the presence of H_2. Gunduz et al. [217] hypothesized that hydrogen may decrease Cr diffusion at the alloy grain boundaries (GB) as other interstitial impurity elements have been reported to

mitigate GB diffusion [218]. Segregation of hydrogen at the GBs of AISI 430 was recently evidenced with ToF-SIMS after a dual atmosphere exposure at 750 °C [219]. Finally, GB diffusion of Cr in a binary model alloy Fe-18Cr at 600 °C was measured to be factor of 1.5–2.0 slower in Ar-5%H_2 compared to purified Ar [220].

A combination of the experimentally measured acceleration factor for oxygen permeability ($N_O^{(s)}D_O$) with the Cr GB diffusion ($\widetilde{D_{Fe-Cr}}$) deceleration factor results in a change in $N_{Cr}^{(1)}$ by approximately a factor of 5.

This may explain the apparent discrepancy with Wagner's model. Nevertheless, one should keep in mind that the model was derived for a case where Cr but not Fe can oxidize. Furthermore, it is obvious that for intermediate temperatures a model which ignores GB transport will fail to predict reasonable critical Cr thresholds in H_2/H_2O. More dedicated research is thus required to quantify the GB transport for both O and Cr in Fe-Cr model systems to provide a reasonable quantitative input for predictive models.

6.5. Interaction with Ni components

Another important aspect is the interdiffusion between the interconnect and the fuel electrode contact. Contacting between the Ni/YSZ electrode and the interconnect is commonly achieved through a Ni mesh or some other kind of Ni-rich component which is used to improve the contact [221]. However, this leads to interdiffusion between ferritic steel and Ni-mesh which leads to austenite formation [67,151,222]. This direct metal/metal contact potentially has the advantage of low ASR although Cr that diffused into the Ni-mesh tends to oxidize internally and might form an oxide layer on Ni grain boundaries potentially increasing ASR [223]. More severe is a significant CTE mismatch between the formed austenite and the rest of the interconnect [67]. Furthermore, this is problematic because the Cr diffusion in austenite is almost 80 times lower than ferrite when values are extrapolated to 600 °C [47]. Hence, when combined with the harsh oxidation conditions of H_2/H_2O it is probable that austenitization leads to non-protective behavior. Additionally, Ni diffusion can promote brittle σ phase formation particularly in steels with Mo or W additions [67,224].

This section has outlined the challenges and underlying oxidation mechanisms of interconnect steels encountered in H_2/H_2O atmosphere relevant to the fuel electrode side of SOECs. The following section focuses on protective coatings and mitigation strategies developed to address these issues.

6.6. Steam side coatings and other mitigation strategies

6.6.1. Surface treatment

Surface preparation significantly affects whether alloys will form a protective or a non-protective scale between 600–800 °C. At 800 °C, Ardigo et al. [183] exposed AISI 441 steel in as-received and polished condition. Polished samples performed much better compared to as-received samples due to induced surface deformation by sample preparation. At 600 °C the effect is more pronounced. Niewolak et al. [19] performed oxidation tests on several commercial ferritic and austenitic steels including Crofer 22 APU, AISI 430, AISI 441 and showed that ground samples exhibited substantially improved corrosion resistance compared with polished specimens. Chyrkin et al. [57] also demonstrated the same effect and showed that at 600 °C in Ar-5%H_2-3%H_2O protective behavior was observed for ground (P1200 grit paper) AISI 441, while as-received samples failed in the same conditions. In the same study, by cross-sectional investigations, a 1.5 μm deep recrystallization layer was observed. The grain size within this layer was determined to be around 60–100 nm. Formation of this layer proves that the near surface region in the alloy is substantially deformed by grinding and recrystallized at 600 °C [57]. Therefore, either the dislocation network or the ultra-fine grained recrystallization layer provides fast diffusion paths that dominate the diffusion process at low temperatures (e.g. 600 °C). Despite this success in Ar-5%H_2-3%H_2O, tests with higher humidity concentrations ($H_2/H_2O \approx 0.02–0.05$) are needed for SOEC conditions to confirm the beneficial effect of grinding.

6.6.2. Pre-oxidation

Pre-oxidation as a mitigation strategy is commonly utilized to form protective layers on FSS interconnects. The idea behind pre-oxidation is to form protective layers (Cr_2O_3/Cr_2MnO_4) on FSS by oxidizing them for a short time in air at operating temperature or a higher temperature. This pre-formed layer has proven to be effective to protect the FSS when compared with the non-pre-oxidized material. For instance, Ardigo et al. [198] investigated the effect of pre-oxidation (800 °C, 10 h, air) on AISI 441 in Ar-1%H_2-9%H_2O at 800 °C for 100 h and found protective Cr_2O_3 /Cr_2MnO_4 scales. Alnegren et al. [225] pre-oxidized AISI 441 samples for 3 h at 800 °C in air and subsequently exposed samples in Ar-5%H_2-3%H_2O at 600 °C up to 3000 h. Except for a few minor Fe-rich nodules the whole surface was covered with protective Cr_2O_3 /Cr_2MnO_4. The same pre-oxidation parameters also resulted in protective layers in Ar-5%H_2-3%H_2O at 600 °C, 700 °C and 800 °C [226]. Tomas et al. [227] reported similar results at 600 °C for 3000 h with 5 h pre-oxidation treatment at 800 °C. Chyrkin et al. [57] also exposed pre-oxidized AISI 441 (800 °C, 20 min) along with non-pre-oxidized samples under Ar-5%H_2-3%H_2O between 550–900 °C for 336 h. Non-pre-oxidized samples formed Fe-rich oxides while pre-oxidized samples always showed protective behavior within this temperature range. Hence, pre-oxidation at 800 °C even for 20 min was successful in Ar-5%H_2-3%H_2O atmosphere. The same study also investigated the effect of pre-oxidation temperature (600 °C and 800 °C) while maintaining the same oxide scale thickness (equal mass gains after pre-oxidation). Subsequent exposures at 600 °C showed that pre-oxidation at 600 °C was not effective in maintaining a protective oxide scale. The protective behavior provided by 800 °C pre-oxidation in air is most probably related to two parameters, I) coverage with $(Cr,Mn)_3O_4$ spinel and II) a coarser oxide grain size [57]. Although a pre-oxidation of 20 min at 800 °C was successful when AISI 441 steel was exposed at 600 °C in Ar-5%H_2-3%H_2O, exposures in higher humidity (Ar-4%H_2-20%H_2O) resulted in the local failure of the pre-oxidized samples after 336 h [57]. Hence, the effect of pre-

oxidation at higher temperatures (800–900 °C) for different durations might be interesting as a future study on interconnect steels for high humidity $H_2/H_2O \approx 0.1$ SOEC environments. Such a study was performed by Shen et al. [228] on porous AISI 434 L steel by pre-oxidation at 850 °C for 10 h. The samples were subsequently exposed in Ar-2.5%H_2-8.2%H_2O and Ar-2.2%H_2-20%H_2O atmospheres between 600–800 °C for 500 h. The samples showed protective behavior in all cases. Yet, a sharp increase in mass gains was observed at 800 °C presumably due to very low Mn concentration (0.14 wt%) of 434 L steel [228]. Therefore, studies with higher Mn containing interconnect steels are needed within this context.

6.6.3. Coatings

In addition to pre-oxidation, coatings have been investigated as a means of improving the corrosion resistance of interconnect steels in H_2/H_2O atmospheres. However, compared with air-side applications, the number of successful coating concepts is considerably smaller due to the low stability of many oxide coatings under reducing conditions. The expected benefits of coatings on the fuel side are i) slowing down the oxide scale growth rate and maintaining protective oxide layers without increasing ASR, ii) mitigating the interdiffusion between Ni-mesh and interconnect. In line with typical operating temperatures, coatings are mostly tested around 800–850 °C, although recent studies have increasingly focused on lower temperatures. To serve this purpose, different coating materials such as spinel and perovskite oxides, reactive elements and their oxides as well as metallic coatings (Ni) have been investigated.

Fontana et al. [229] deposited reactive oxide coatings (La_2O_3, Nd_2O_3, Y_2O_3) on Crofer 22 APU and Fe-30Cr by MOCVD and exposed at 800 °C in Ar-1%H_2-10%H_2O up to 100 h. On Crofer 22 APU, all coatings resulted in moderate reduction in oxide growth rate with La_2O_3 and Nd_2O_3 being most effective. Top view SEM investigations showed that the surfaces were crack free in all cases. In a RE free binary Fe-30Cr model alloy the situation was different since it formed only Cr_2O_3 not a duplex Cr_2O_3/Cr_2MnO_4 scale. In this case oxidation of the uncoated alloy was much faster and consequently the effect of the coatings was much more pronounced.

Sachitanand et al. [186] deposited thin films of Co, Ce and La on Sanergy HT steel and exposed these samples in as-deposited and pre-oxidized (16 h, 850 °C) condition at 850 °C up to 500 h in Ar-5%H_2-3%H_2O. The Co coating agglomerated into metallic islands on the surface while La and Ce effectively decreased the oxide growth rate by a factor of 2–3. Ardigo et al. [230] deposited perovskite ($La_{1-x}Sr_xMnO_{3-\delta}$) and spinel ($Co_3O_4$) coatings on AISI 441 and tested them at 800 °C in Ar-1%H_2-9%H_2O for 3000 h. The authors did not report oxidation rates but stated that both coatings prevented Fe-rich oxide formation. Furthermore, the Co_3O_4 coating under these conditions is reduced into Co while LSM is decomposed into MnO and La_2O_3 which resulted in a slight reduction in ASR values. Hence both coatings are not feasible under H_2/H_2O atmosphere [230]. In a follow-up study, Ardigo et al. [231] tested two spinel (Co_3O_4, Co_2MnO_4) and two perovskite ($La_{0.8}Sr_{0.2}MnO_3$ and $LaNi_{0.6}Fe_{0.4}O_3$) coatings at 800 °C in Ar-1%H_2-9%H_2O for up to 3000 h. All coatings prevented Fe-rich oxide formation. The thinnest (<1.5 μm) oxide scales were formed on the LSM coated samples while the thickest oxide scales were observed on Co_3O_4 coated samples (3 μm). Yet, all coatings experienced decomposition due to instability of Ni and Co oxides. King Jr. et al. [187] coated Ni and Ni-P coatings on AISI 430 steel and exposed them in Ar-3%H_2–(dry and 3%H_2O) at 800 °C up to 100 h. In dry conditions the Ni-P showed very similar mass gains (0.55 mg/cm^2) compared to bare alloy (0.58 mg/cm^2) while Ni exhibited a better performance (Ni:0.46 mg/cm^2). It should be stated that in dry Ar-3%H_2 Fe does not oxidize. Yet, under wet conditions the Ni-P coating was unsuccessful and exhibited much higher mass gains (1.4 mg/cm^2) than bare AISI 430 (0.72 mg/cm^2) after 100 h. Ni coating on the other hand resulted in lower mass gains (0.44 mg/cm^2). At 800 °C interconnect steels usually form protective scales in H_2/H_2O conditions. Among the tested coatings, only reactive element oxide coatings provided a beneficial effect on oxide growth rate reduction. Other coatings such as Co and Ni containing spinels as well as LSM were not stable under these conditions and did not provide a significant beneficial effect and might be detrimental in the long-term oxidation tests.

At 600 °C the number of studies is even more limited. Therefore, data from the fuel side of samples exposed to a dual-atmosphere H_2/H_2O environment are also included in this section. Tomas et al. [227] deposited Al (1000 nm) and Al_2O_3 (600 nm) films on the fuel side of AISI 441 as a hydrogen barrier. Coated samples were pre-oxidized (3 h 800 °C) and subsequently exposed at 600 °C up to 3000 h in Ar-5%H_2-3%H_2O. All samples exhibited protective behavior. Furthermore, Al coated + pre-oxidized samples were additionally exposed to 7000 h which also resulted in protective behavior. Despite this success, the drawback was a high ASR of these coatings (Al:0.1 Ω*cm^2, Al_2O_3:1.1 Ω*cm^2) even after 168 h at 600 °C. In a follow up study Tomas et al. [232] deposited Al_2O_3 (30 nm, 100 nm, 300 nm, 600 nm), CeO_2(50 nm, 300 nm), Cr_2O_3 (200 nm) and YSZ (50 nm, 200 nm) on AISI 441 steel samples and subsequently pre-oxidized (20 min at 800 °C). The samples were exposed at 600 °C for 1000 h in Ar-5%H_2-3%H_2O. All samples including the uncoated pre-oxidized showed protective behavior. Sadeghimeresht et al. investigated austenitic 304 L samples that were exposed at 600 °C in Ar-10%H_2-20%H_2O for 168 h in bare and coated (Ni, Ni-Cr by HVAF) condition [185]. The coated samples, especially Ni-Cr coating, were able to prevent corrosion while bare samples developed typical duplex non-protective oxide scales [185]. In a similar manner, a low Cr (9 wt% Cr) ferritic/martensitic ODS (0.25 wt% Y_2O_3) steel was exposed at 650 °C under steam atmosphere in bare condition and with a Cr interdiffusion coating (4 μm Cr by PVD + annealing 1150 °C for 1 h) for 500 h [233]. The uncoated specimen exhibited thick Fe-base scales while the Cr interdiffusion coating resulted in the formation of very thin Cr_2O_3 scales [233]. These examples are given to illustrate that even low alloyed steels can exhibit excellent performance by utilizing such coatings.

Pre-oxidation and coatings were not only utilized to slow down oxide growth rate but also to mitigate interdiffusion between nickel mesh and interconnect. Yet studies are very limited within that context. One such study was carried out by Froitzheim et al. [223]. In that study Crofer 22 APU was pre-oxidized at 800 °C for 100 h and subsequently sputter coated with Ni to simulate the stack conditions. However, pre-oxidation did not prevent the inter-diffusion between Ni and Crofer 22 APU due to dissociation of pre-formed layer by Ni. As an alternative strategy, a 2–4 μm thick CeO_2 coating was proposed as a diffusion barrier against interdiffusion. This barrier layer prevented interdiffusion successfully, but void formation was observed between the oxide scale (Cr_2O_3/Cr_2MnO_4) and the CeO_2 coating. To prevent contact loss, a 3 μm thick copper interlayer was deposited on pre-oxidized Crofer 22 APU and subsequently coated with 2 μm thick CeO_2. Good contact between all layers was achieved and interdiffusion was mitigated.

To summarize, high temperature oxidation of interconnect steels on the steam electrode side of SOECs (H_2/H_2O) is substantially different compared to the air side. In contrast to the air side, an inverse temperature effect on the oxidation rate is observed in H_2/H_2O. Corrosion rates are fastest around 600–650 °C due to formation of Fe-rich non-protective layers. Increasing temperature reduces the tendency for fast growing Fe-oxides. At 800 °C, especially for Mn containing steels, the oxidation rates in air and H_2/H_2O are relatively similar. Oxidation rates are initially faster in H_2/H_2O but slower over the long term due to coverage with Cr_2MnO_4. In some cases, Fe-rich oxides are formed on the surfaces which is likely related to initial oxide formation. Increased humidity further intensified the corrosion rate around the critical temperature of 600 °C. In the intermediate temperature range, degradation is very sensitive to modifications of the near surface microstructure and surface treatment such as grinding has a major impact, due to formation of a fine-grained recrystallization layer.

As a mitigation strategy, pre-oxidation seems to be a viable option to prevent Fe-rich oxide formation on the fuel electrode side of SOEC. In fact, due to this success, it can be argued whether coatings are necessary to improve the oxidation properties of interconnect steels on the steam electrode of SOECs.

However, coatings not only serve to improve the oxidation properties on the steam side, they may also prevent the interdiffusion between Ni contact and interconnect or act as hydrogen barriers to mitigate the dual atmosphere effect observed on the air side as will be discussed in the next section.

6.7. SOFC vs SOEC – H_2/H_2O side

Despite the important work carried out so far, the water vapor concentrations in most studies simulating the steam side are relatively low and more relevant to SOFC anode gas compositions. Furthermore, mitigation strategies such as pre-oxidation or coatings have so far been studied primarily in these low $p(H_2O)$ atmospheres. Hence, exposures at higher humidity ($H_2/H_2O \approx 0.1$) need to be performed to determine the corrosion behavior as well as confidently predict lifetimes in such environments. Furthermore, it is desired to operate SOECs at higher pressures (≈5 bar or 0.5 MPa) rather than ambient atmosphere to avoid costly hydrogen compression [234,235]. Running cells under elevated pressure in general results in higher OCV and an increase in efficiency [236,237]. This behavior is also modeled by Rizvandi et al. [234]. To the best of the authors' knowledge, no dedicated studies have investigated the effect of absolute pressure on the oxidation behavior of interconnect steels in H_2/H_2O atmospheres. Consequently, the influence of pressure under SOEC-relevant conditions remains largely unknown. A pressure effect has, however, been observed in studies conducted in steam and supercritical steam environments for materials used in boiler applications. For example, Zhang et al. [238] tested P92 and found an increase in corrosion rate by about 30% when the pressure was increased to 80 bar. Direct extrapolation of these results to SOEC conditions is difficult because boiler environments typically contain steam with trace amounts of O_2, whereas SOEC fuel-side atmospheres contain H_2/H_2O mixtures and are governed by fundamentally different oxidation mechanisms. Moreover, the relatively modest effect observed at 80 bar suggests that increasing the pressure to the few-bar range relevant to SOEC operation is unlikely to have a major direct effect on oxidation. Pressurization nevertheless also increases the absolute partial pressure of H_2 at a constant H_2/H_2O ratio. This may enhance hydrogen uptake and transport through the steel, potentially affecting steam-side oxidation and hydrogen-mediated degradation mechanisms such as the dual-atmosphere effect discussed in Section 7.2. Dedicated studies under pressurized H_2/H_2O conditions are therefore required to elucidate these aspects.

7. Dual atmosphere conditions

The interconnects in a SOEC stack are subject to a high temperature environment with O_2, potentially diluted with a sweep gas, on one side and a H_2/H_2O mixture on the other. This so-called dual atmosphere is known to result in corrosion that differs from the results obtained in experiments where the steel is exposed to only one of these atmospheres. The effect has been most widely studied with respect to SOFC interconnects although similar results have also been observed in boiler tubes [239]. In SOEC context this is not only relevant for interconnects but might also have implications for certain BOP components.

7.1. Observations

In SOFC context a dual atmosphere effect was first reported by Yang et al. in 2003 [240]. They reported that AISI 430 exposed to dual atmosphere conditions (air//H_2-3%H_2O) formed a more Fe-rich oxide scale, including the presence of Fe_2O_3, on the air side while an experiment with air on both sides resulted in a protective oxide scale of Cr_2O_3 and spinel. This triggered a stream of investigations studying various FSS under dual atmosphere conditions. Table 4 presents an overview of dual atmosphere results published in peer reviewed papers. Most of these studies focused on temperatures of 800–900 °C (relevant operating temperatures for SOFCs at that time) and gave contradictory results. Some authors confirmed Yang's findings [240] or found an even more severe effect [241] while others reported only a slight enrichment of Fe in the oxide scale or no observable effect at all [242–245]. Nevertheless, there is agreement that the dual atmosphere effect is only observed on the air side and the fuel side is unaffected by whether the other side of the sample is exposed to air or H_2/H_2O. Subsequent work by Alnegren et al. [226] and Gunduz et al. [217] investigated AISI 441 under dual atmosphere conditions at temperatures between 500–800 °C. These studies showed the most severe dual atmosphere effect is observed around 600 °C, whereas, somewhat counterintuitively, higher temperatures promote more protective oxide scales. Furthermore, it was shown that pre-oxidation of the samples effectively reduced the dual atmosphere effect [217,246,247]. This is in line with permeation experiments by Kurokawa [245] showing that hydrogen permeation is about four orders of magnitude lower through Cr_2O_3 than Fe or Fe-Cr steel. Considering these results the discrepancies between the earlier dual atmosphere studies carried

Table 4
Summary of dual atmosphere oxidation studies.

Year	Authors	Temperature	Metal	Thickness	Duration	Air side	Fuel side	Comparison Dual vs Single
2003	Yang et al [240]	800 °C	AISI 430	0.5 mm	300 h	air	H_2-3%H_2O	Thicker, Fe_2O_3
2004	Kurokawa et al [245]	800 °C	AISI 430	<2mm	24–300 h	dry air	Ar-20%H_2-0.6%H_2O	Almost similar
2004	Yang et al [253]	800 °C	AISI 430	0.5 mm	300 h	air	H_2-3%H_2O	Thicker, Fe_2O_3
2004	Yang et al [253]	800 °C	Crofer 22 APU	0.5 mm	300 h	air	H_2-3%H_2O	Similar, Fe_2O_3 when cyclic
2004	Yang et al [253]	800 °C	E-brite	0.5 mm	300 h	air	H_2-3%H_2O	Minimal difference
2005	Hammer et al [65]	800 °C	Crofer 22 APU	Not specified	300 h	air	H_2-3%H_2O	Similar with Fe enrichment
2005	Yang et al [254]	800 °C	Crofer 22 APU	0.5	300 h	air - (1–3)% H_2O	H_2-3%H_2O	Fe_2O_3 nodules
2006	Holcomb et al [255]	700 °C	316 L	0.78 mm	100 h	air	H_2	4 vs 50 μm (in breakaway part)
2007	Yang et al [256]	800 °C	Haynes 230	0.5 mm	300 h	air-3%H_2O	H_2-3%H_2O	Similar
2007	Yang et al [256]	800 °C	Haynes 242	0.5 mm	300 h	air-3%H_2O	H_2-3%H_2O	Similar
2007	Yang et al [256]	800 °C	Hastelloy S	0.5 mm	300 h	air-3%H_2O	H_2-3%H_2O	No NiO found
2007	Yang et al [256]	800 °C	Crofer 22 APU	0.5 mm	300 h	air ~ 1% H_2O	H_2-3%H_2O	Minimal difference Fe enrichment
2007	Yang et al [256]	800 °C	Fecralloy	0.5 mm	300 h	air ~ 1% H_2O	H_2-3%H_2O	Minimally thicker
2007	Yang et al [256]	800 °C	Haynes 230	0.5 mm	300 h	air ~ 1% H_2O	H_2-3%H_2O	Small differences in morphology
2007	Yang et al [256]	800 °C	Ni (99.5%)	0.5 mm	300 h	air ~ 1% H_2O	H_2-3%H_2O	Minimally thicker
2008	Rufner et al [241]	800 °C	AISI 430	0.9 mm	200 h	air-3%H_2O	H_2-3%H_2O	Slightly more Fe, thickness similar
2008	Rufner et al [241]	800 °C	AISI 441	1.6 mm	200 h	air-3%H_2O	H_2-3%H_2O	Significant effect in thickness single:0.5 μm vs dual 8 μm
2012	Amendola et al [250]	800 °C	Crofer 22 APU	0.8 mm	200 h	air-3%H_2O	H_2-3%H_2O	More Fe, thickness similar especially with Pre-oxidation
2012	Skilbred et al [243]	800–900 °C	Sanergy HT	0.2 mm	100–500 h	air	dry and wet Ar-5%H_2	Similar thickness, more Fe
2012	Zhao & Fergus [257]	800 °C	AISI 430	1.2 mm	200 h	dry air	H_2-3%H_2O	Thicker but not significant, more Fe
2012	Zhao & Fergus [257]	800 °C	AISI 441	1.45 mm	200 h	air, dry or 3%H_2O	H_2-3%H_2O	Thicker but not significant, more Fe
2012	Zhao & Fergus [258]	800 °C	AISI 430	1 mm	100–400 h	wet air	wet Ar 5% H_2	Thicker but large variation due to nodules
2012	Zhao & Fergus [258]	800 °C	AISI 441	1 mm	100–400 h	wet air	wet Ar 5% H_2	Slightly thicker
2014	Leonard [259]	800 °C	AISI 441	0.2 mm	100 h	air-3%H_2O	H_2-3%H_2O	Ni coated. Much thicker oxide scale
2014	Stygar et al [260]	800 °C	DIN 50049	1 mm	110–478 h		Ar H_2 H_2O	No difference
2015	Ardigo et al [244]	800 °C	AISI 441	1 mm	100 h	O_2-5%H_2O	Ar-1% H_2-9%H_2O	Similar
2017	Li et al [252]	750 °C	430	1 mm	200 h	ambient air	N2-5%H_2, H_2, CH_4	Intense Fe_2O_3 formation in particular in pure H_2
2017	Stygar et al [261]	800 °C	Crofer 22 APU	1 mm	100–1000 h	air	Ar-10%H_2-0.6%H_2O	thinner in dual. Local corrosion variation over sample surface
2018	Alnegren et al [226]	600-800°C	AISI 441	0.2 mm	1000 h	air, dry or 3%H_2O	Ar-5%H_2-3%H_2O	Pre-oxidized. Breakaway at 600 °C Identical in 700–800 °C
2019	Wang et al [262]	650 °C	AISI 441	0.15 mm	500 h	air -50%H_2O	Ar-2.8%H_2	Similar oxide scales due to 50% steam concentration in air
2021	Reisert et al [247]	600 °C	ZMG232G10	0.1 mm	50 h	dry air	4%H_2-3H_2O in N_2	Massive difference in top view images, Fe_2O_3 formation
2021	Reisert et al [247]	600 °C	AISI 444	0.1 mm	50 h	dry air	4%H_2-3H_2O in N_2	Massive difference in top view images, Fe_2O_3 formation
2021	Reisert et al [247]	600 °C	Al-FSS	0.1 mm	50 h	dry air	4%H_2-3H_2O in N_2	Minimal difference in top view images
2023	Reisert et al [18]	600 °C	ZMG232G10	0.1 mm	500 h	dry air	4%H_2-3H_2O in N_2	As-received nodule formation pre-oxidized protective

(*continued on next page*)

Table 4 (*continued*)

Year	Authors	Temperature	Metal	Thickness	Duration	Air side	Fuel side	Comparison Dual vs Single
2024	Inuzuka et al [249]	700 °C	ZMG232G10	1 mm	500 h	ambient air	90%H_2O-10%H_2	Similar scale formation
2024	Inuzuka et al [249]	700 °C	Crofer 22 APU	1 mm	500 h	ambient air	90%H_2O-10%H_2	Similar scale formation
2024	Inuzuka et al [249]	700 °C	430	1 mm	500 h	ambient air	90%H_2O-10%H_2	Heavy corrosion under dual conditions

out at 800 °C can be mostly understood. Some experiments relied on a mechanical clamping mechanism while others required brazing or glass sealants, the latter requires a heat treatment step at higher temperature presumably carried out in air which corresponds to a pre-oxidation step. Furthermore, because at 600 °C the dual atmosphere effect is far more severe than at 800 °C the heating rate, which is often not reported, can be a critical parameter affecting results. Although this makes comparisons of results from different laboratories difficult, individual studies shed light on certain parameters that affect the severity of the dual atmosphere effect. Higher Cr content in the steel [65,248,249], pre-oxidation [226,246,250], grinding rather than polishing and greater steel thickness [251] are all beneficial. In contrast, pure hydrogen is more harmful than diluted mixtures [252] and Laves phase containing steels seem to be more prone to attack than steels without Nb additions [241].

Fig. 10a shows dual atmosphere induced breakaway oxidation spot on AISI 441. The oxide scale exhibits a typical island/crater morphology with an outer Fe_2O_3 oxide island and an inward growing $(Fe,Cr)_3O_4$ oxide crater. On the left-hand side of the image the protective oxide is intact and is so thin that it is barely visible. Fig. 10b shows a highly similar morphology from a ferritic steel interconnect that was operated in a stack for more than 5000 h.

7.2. Mechanism

The apparent contradictions in the results have led some authors to attribute the dual atmosphere effect to leakage or sealant contamination while claiming that it does not occur in real stack operation [263]. Fig. 11 shows the piping made of AISI 316 L stainless steel leading to the dual atmosphere sample holder after one experiment for 1000 h. While the steel pipe with air on the inside shows a thin protective scale its counterpart that was filled with Ar-5%H_2 is massively corroded on the air side. Similar results with tubular specimens of AISI 316 L were published by Holcomb et al. [255].

Hence, there is clear evidence confirming the existence of a dual atmosphere effect under certain conditions. It is also commonly agreed upon that hydrogen diffuses through the metal affecting air side oxidation. In their groundbreaking paper, Yang et al. [240] used hydrogen diffusion data that were recorded between 30–50 °C [264] and extrapolated them to 800 °C and achieved a value for $D_H = 1.6*10^{-2}$ cm^2/s. Based on this value a diffusion distance of 76 mm within 1 h was estimated and this number has been commonly cited in the literature ever since. However, other authors [265] performed experiments on Fe in the relevant temperature range and estimate $D_H \sim 3*10^{-4}$ cm^2/s, so two orders of magnitude lower. Nevertheless, this does not change the fact that hydrogen diffusion through a thin ferritic stainless steel sheet will be very fast.

Despite the work carried out in the past 20 years, the underlying mechanism of how hydrogen affects the air side oxidation is elusive. Yang et al. followed up their initial findings with a second paper, in which they proposed that hydrogen in the oxide scale results in an increase of cation vacancies which in turn would result in faster oxide scale growth [253]. This argument has been commonly repeated in the literature [241,243,247,260]. Others [255] suggested that water vapor formation due to the combination of

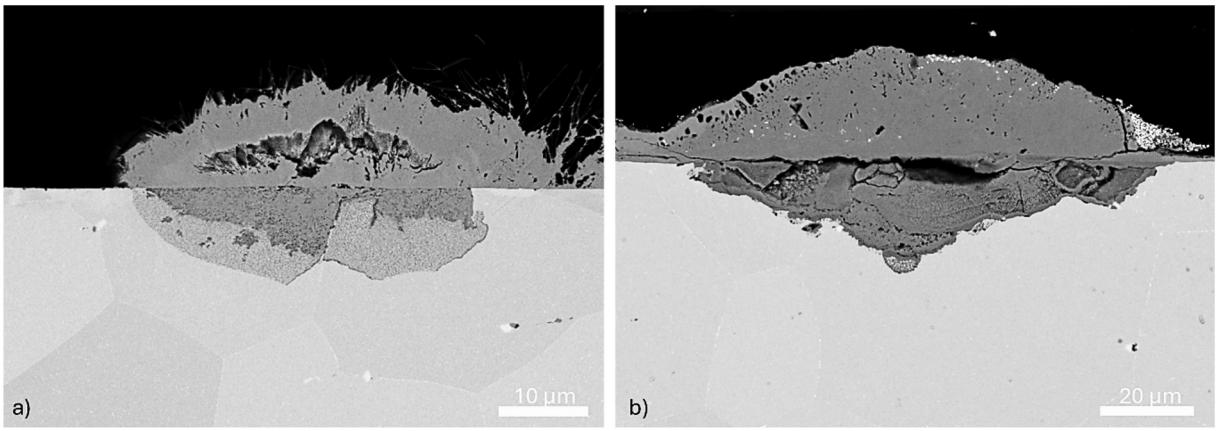

Fig. 10. Typical, dual atmosphere induced breakaway oxidation morphologies. (a) Air side of AISI 441 exposed 500 h at 600 °C (including 20 min pre-oxidation) adapted from [248] (b) Air side of a ferritic steel interconnect that was operated in a SOFC stack at approximately 600 °C, for more than 5000 h at Ceres Power in 2021. (Courtesy of R. Leah, Ceres Power).

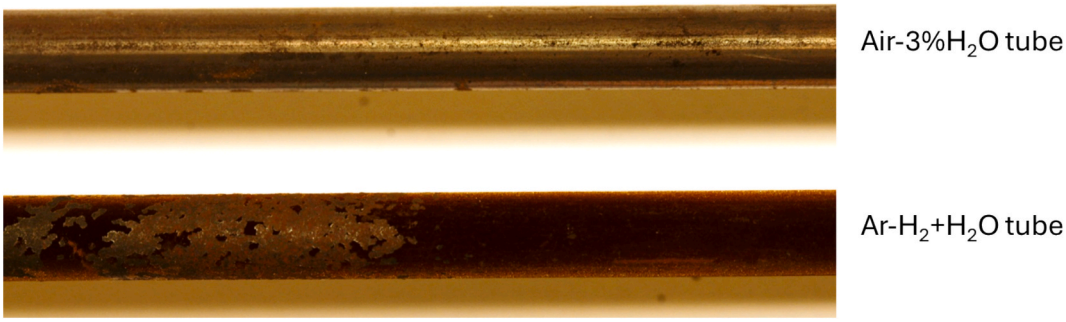

Fig. 11. Image of the 316 L stainless steel pipes leading to the dual atmosphere setup after the first 1000 h experiment. The steel tubes have an outer diameter of 6 mm and the pictured area is about 20 cm from the samples so the observed corrosion cannot reasonably be attributed to leakage from the sample holder.

hydrogen with oxygen results in pore generation and faster transport of oxidants along these pores (Rahmel and Tobolski mechanism) [200]. Common to these arguments is that they suggest mechanisms that result in faster oxide scale growth which would then lead to a thicker oxide scale, possibly leading to delamination, more Cr depletion and subsequently leading to breakaway corrosion.

Although thicker oxide scales in some cases are observed under dual atmosphere conditions [225,241,257] these thicker scales often comprise of Fe_2O_3 either as continuous layer or as nodules. However, Fe_2O_3 is formed after the oxide has lost its protective properties, while in locations where the oxide scale is protective the observed differences between dual and single atmosphere exposures are often negligible or even slightly thinner under dual atmosphere conditions [226]. The formation of Fe_2O_3 can also result in misleading data if average oxide thicknesses are compared because they are skewed by thick sections of Fe-rich oxide. In a later paper Yang et al. [256] presented a cross-section of the protective region of the oxide scale formed under dual atmosphere conditions on Crofer 22 APU, this oxide is indeed thinner than the oxide scale formed under single atmosphere conditions. Alnegren et al. [226] meticulously measured the thickness of the protective oxide between 600 and 800 °C and found no increase in thickness of the protective oxide. To conclude, once breakaway has occurred the oxide scale will be significantly thicker in dual atmosphere, however, this is not the cause for breakaway but a consequence. Hence, all explanations suggesting faster oxide scale growth whether by doping, pore formation or other mechanisms seem to be inadequate to explain the breakdown of the protective oxide scale and hence the dual atmosphere effect. Furthermore, Gunduz et al. [217] performed a quantitative analysis using Wagner's model and concluded that even a 10-fold increase in oxidation rate would not be sufficient to cause breakaway oxidation on a Fe-18%Cr steel.

Alternatively, Essuman et al. [206] proposed that dissolved hydrogen interstitials in the metal increase the oxygen permeability leading to increased internal oxidation. Alnegren et al. [226] speculated that this immobilization of Cr could explain the dual atmosphere effect. However, recent work by Chyrkin et al. [43,213] provided evidence that there is no significant effect of hydrogen on bulk oxygen permeability. Nevertheless, experiments with a diluted binary Fe-2Cr alloy in H_2/H_2O revealed increased oxygen permeation, beyond the bulk IOZ, along the alloy grain boundaries (GBs) below 800 °C [43]. This hints at potentially increased oxygen permeability along interfaces such as steel GBs in the presence of H_2. It is thus conceivable that once the protective oxide breaks, e.g. due to a local defect, fast oxygen ingress along internal oxide interfaces causes widespread breakaway. Compare Fig. 10a which shows a network of sub-micron oxide precipitates growing into the metal. This huge number of interfaces might provide transport pathways for oxygen to cause widespread failure.

An alternative explanation was provided by Gunduz et al. [217]. By discarding all other explanations, they concluded that the only plausible hypothesis left was that hydrogen affects Cr diffusion, in particular along metal grain boundaries. Segregation of hydrogen at the GBs of AISI 430 was recently evidenced with ToF-SIMS after a dual-atmosphere exposure at 750 °C [219]. Unfortunately, there is a lack of direct experimental evidence for this hypothesis. Nevertheless, the fact that the dual atmosphere effect is most severe around 600 °C and is reduced or disappears entirely at higher temperatures hints at Cr diffusion being of critical importance [217].

In summary, the mechanism behind dual atmosphere corrosion is not fully understood. While most data and models can provide accurate pictures of bulk processes, grain boundary transport is much harder to account for. Unfortunately, at intermediate temperatures around 600 °C where the dual atmosphere effect is most pronounced the protectiveness of a Cr_2O_3 scale is to a very large extent governed by grain boundary transport.

7.3. Mitigation

Any mitigation strategy against dual atmosphere corrosion will either focus on the protective oxide scale on the air side or alternatively on reducing hydrogen ingress on the fuel side. The easiest mitigation strategy seems to be pre-oxidation of the steel. It was shown by several authors [18,225–227,246–248,250] that pre-oxidation substantially reduces dual atmosphere corrosion which can have a beneficial effect on both sides of the steel. By selectively removing the pre-oxidation scale Goebel et al. [246] showed most of the beneficial effect can be attributed to the oxide scale on the fuel side. This is in line with Kurokawa [245] who showed that a Cr_2O_3 scale reduces hydrogen permeation by about four orders of magnitude. Goebel et al. [246] furthermore showed a clear relationship between duration of pre-oxidation and the onset of breakaway corrosion. Reisert et al. [247] compared pre-oxidation in H_2/H_2O (when

FeO is not stable) with pre-oxidation in air and found the former to be more effective. However, it should be noted that the pre-oxidation in air had a substantially lower mass gain (≈thinner oxide scale). Despite the benefits of pre-oxidation it seems that pre-oxidation only delays the onset of hematite formation. Tomas et al. [227] showed that a sample pre-oxidized for 5 h at 800 °C shows initially protective behavior but between 1000 and 3000 h of exposure the number and size of hematite nodules were slowly but continuously increasing. An alternative approach is the use of coatings that inhibit hydrogen ingress on the fuel side. Tomas et al. [232] tested different oxide coatings (Cr_2O_3, CeO_2, YSZ and Al_2O_3) in the range between 50 and 600 nm and found that the latter two were best in minimizing dual atmosphere corrosion, however, these oxides are also poor electronic conductors resulting in significantly increased ASR. In another work, Tomas et al. [227] tested metallic Al that became oxidized during operation and got similar results as for Al_2O_3. The effect of a classical MCO type coating on the air side seems to have no large benefit if any [250].

8. Electrical performance and operational effects

8.1. Area specific resistance (ASR)

Because the interconnect is part of the electric circuit and Cr_2O_3 is a mediocre electronic conductor, the electronic resistance of the oxide scale is of central importance. Resistance is commonly reported as Area Specific Resistance (ASR) which is the resistance multiplied with the contact area. It is most commonly expressed in mΩ*cm^2. Since steel has a much higher electronic conductivity the resistance across the metallic interconnect is typically dominated by the resistivity of the oxide scale, which grows with time. With parabolic oxide scale growth kinetics and constant oxide resistivity, one would expect that ASR follows similar parabolic kinetics. Nevertheless, this is often not the case, probably due to several factors, such as impurity incorporation, improved contacting, and sintering of electrodes.

A multitude of ASR measurement techniques have been reported in the literature. The typical setup sandwiches a sample between two electrodes and a four-point measurement is applied to eliminate the resistance contribution of the wires. The measured resistance is attributed to the oxide scales and is commonly divided by two as the sample is oxidized on both sides, although this is not always clearly specified in publications. ASR measurements reported in the literature can be classified into two broad categories: in-situ and ex-situ. Ex-situ ASR measurements are conducted after oxidation tests and typically measure resistance in a through-plane configuration, where the dominant contribution arises from the growing Cr_2O_3 scale. In-situ ASR measurements are conducted during oxidation tests often over extended periods of time, where the ASR is measured either at regular intervals or continuously. The choice of contact material, which significantly influences ASR measurements, varies between noble metals (e.g. Pt [119]) and perovskite oxides (e.g., LSCF, LSM, LSC [93]) as shown in Fig. 12a and b, respectively. The selection of a contact material is critical, as it can induce anomalous oxidation [266] of the FSS or introduce additional contact resistance from the formation of secondary phases (e.g., $SrCrO_4$) at the paste/oxide scale interface [101]. When a noble metal (Pt) is used as the contact material, the resulting ASR value reflects the combined resistance of the oxide scale and the coating; however, this configuration does not accurately represent the operational environment of a SOC stack. ASR measurements using perovskite oxides provide a metric closer to reality, but they can be harder to interpret due to contacting effects. Furthermore, the temperature dependence of the ASR is harder to measure due to the temperature dependence of the conductivity of the ceramic electrode. Moreover, the use of various contact materials with different compositions and densities by various labs, variations in design and applied load make it difficult to compare results across the published literature. Most literature data compare a coating with an uncoated steel, measured using the same technique. But it is difficult to compare the value in a quantitative manner. For example, Yang et al. and Öztürk et al. reported an ASR value of 9–10 mΩ*cm^2 for uncoated Crofer 22 APU at 800 °C after 500 h while Mohsenifar et al. reported a value above 40 mΩ*cm^2 for nominally identical conditions [267–270]. This illustrates that while various ASR methods give similar order of magnitude values a comparison of absolute values is rarely meaningful. This point is further demonstrated by a subsequent publication by Yang et al. that reported 40 mΩ*cm^2 for uncoated Crofer 22 APU at 800 °C after 400 h using LSF contacting instead of Pt. Niewolak et al. [263] compiled long-term ASR data for different uncoated steels at 800 °C: Venskutonis reported a value of ~ 3 mΩ*cm^2 after 500 h that increased to ~ 12 mΩ*cm^2 after 5000 h while others reported much higher values (≥100 mΩ*cm^2 after 500 h) and steeper increases for Si containing

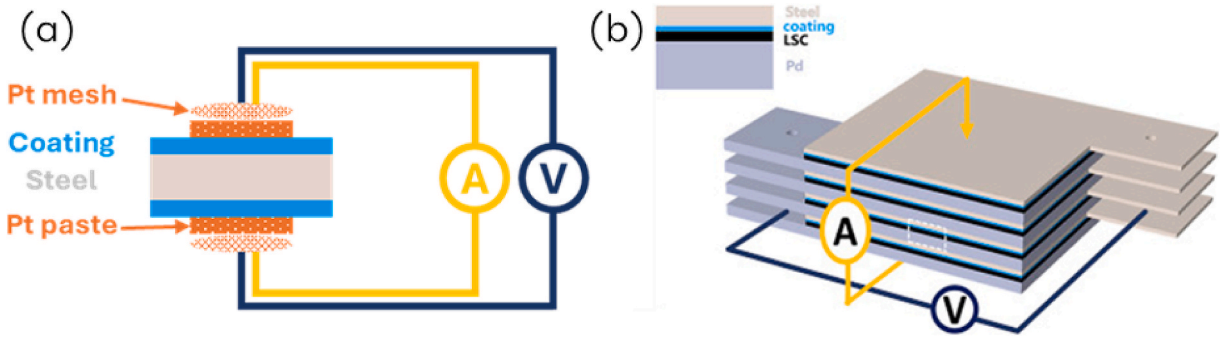

Fig. 12. Schematic representation of ASR measurements using (a) Pt as the contact layer on a single coated FSS coupon and (b) LSC as the contact layer with multiple specimens connected in series (only one voltage probe shown for clarity). Reprinted with permission from [272].

steels. This difference is attributed to SiO_2 formation but the effect of measurement method should not be discarded because Talic et al. [271] reported around 50 mΩ*cm^2 for uncoated Crofer APU after 4000 h of exposure.

For the reasons mentioned above, meaningful comparisons between coated steels are only possible when they are conducted systematically using a consistent experimental setup and identical contact materials [272,273]. In the literature an acceptable ASR of 100 mΩ*cm^2 is commonly cited [274]. The origin of this limit could not be identified by the authors, but it has been stated already in the early 2000 s. Nevertheless, for modern interconnects a much lower limit is probably more realistic. Most reported ASR measurements have been carried out at 800 °C with durations of a few hundred hours. For these conditions typical values for uncoated steels are in the range of 10–50 mΩ*cm^2 while the use of a protective coating commonly results in lower values.

For the selection of coatings conductivity has been one of the most important selection criteria. Indeed, many spinel coatings in the literature have various dopants added to improve the conductivity of the coatings. Petric et al. [170] have reported the conductivity of various spinels which could be potentially used as coatings in SOFC interconnects at 800 °C, and the conductivity varies substantially between the spinels with Fe, Mn, Ni and Co as A and B in AB_2O_4. Nevertheless, underneath the coating a Cr_2O_3 scale is formed and the conductivity of Cr_2O_3 is several orders of magnitude lower than that of the coating. Consequently, the conductivity of the coating itself is expected to contribute little to the overall ASR in most cases (see section 5.4).

8.2. Effect of current polarity in SOEC

The oxide scale on ferritic stainless steels grows primarily by diffusion of ionic species, typically chromium cations and oxygen anions, through the oxide layer. Because ionic transport involves charged species, it is not unreasonable to expect that an applied electric current can influence these diffusion processes by modifying the electrochemical potential gradients across the oxide scale.

In solid oxide electrolysis cells (SOECs), the current densities are commonly higher than in solid oxide fuel cells (SOFCs), which may exacerbate such effects. Studies have shown that electric fields or currents can alter oxide growth kinetics by accelerating or retarding ionic migration depending on the polarity and magnitude of the applied potential. Jeon et al.[275] employed molecular dynamics to study the initial oxidation of Fe during the first nanoseconds of exposure in the presence of an external field of 10 MV/cm and found a significant but limited effect. In contrast, the electric field over the oxide scale of an interconnect is in the range of well below 1 kV/cm. Nevertheless, some experimental studies support the notion that there is a small but noticeable effect. Kodjamanova and co-workers investigated Crofer 22 APU and Crofer 22 H at 800 °C with an applied current of 0.5 A/cm^2 and reported that in SOEC mode this led to accelerated corrosion on the oxygen electrode (O_2) side, while the corrosion rate on the H_2/H_2O side was reduced [276]. Kawamura et al. [277] investigated Fe–25Cr alloys at 1073 K under conditions with and without an applied current of 0.5 A/cm^2. After 240 h, they observed that, in SOFC mode, the scale thickness on the fuel electrode side on the interconnect increased by approximately 15%, while it decreased correspondingly on the air electrode side when current was applied. Ryter et al. [278] studied the effect of current on Ni plated AISI 441 in dual atmosphere conditions at 700 °C and 0.5 A/cm^2 and found an effect on both sides although due to massive coating-steel interaction it is hard to pinpoint the effect of current.

Li et al. [279] investigated 5-cell stacks with AISI 430 interconnects and also reported that electric current promotes cation migration and a corresponding effect on ASR. On the other hand, e.g. Talic et al. [271] and Molin et al. [280] used the same current density of 0.5 A/cm^2 when they studied coated interconnects and observed no difference in ASR between the two sides of the sample indicating no significant effect of current polarity. One reason for these discrepancies may be whether the test is performed in single atmosphere (Kodjamanova et al., Talic et al., Molin et al.), dual atmosphere (Kawamura et al., Ryter et al.) or in real stacks (Li et al.). Nevertheless, this cannot account for the differences observed in the single atmosphere studies.

8.3. Interconnect performance and degradation during long-term stack operation

Over the past fifteen years, more than twenty papers have reported long-term stack operation data with post-mortem analysis. Most focus on the cell development, and only a few examine the interconnect in detail [14,151,273,281–290]. Most studies were carried out in SOFC mode, but because operating conditions (mode, temperature, duration, fuel) and materials (steel, coating) vary widely, firm mechanistic conclusions are difficult to draw. Nevertheless, most stacks use Crofer 22 APU coated on the air side with a $(Co,Mn)_3O_4$-type coating.

Stack studies broadly confirm the oxidation and chromium transport mechanisms established in laboratory exposures. Most of these studies were carried out at 700–850 °C, and almost all authors reported well-adherent, protective $Cr_2O_3/(Cr,Mn)_3O_4$ scales similar to those observed in laboratory tests. A notable exception are studies from Forschungszentrum Jülich, which reported widespread breakaway oxidation in 0.2 mm thick Crofer 22 APU foils in the manifold area, attributed to local overheating and hydrogen/steam leakage [283,288].

Several authors showed that oxidation rates vary within the stack due to local variations in operating conditions. Although the underlying causes cannot always be identified unambiguously, gradients in temperature and steam content, for example between inlet and outlet, appear to be the most likely explanation [14,285,286]. Some studies provided data from stacks operated for different durations. Although there is considerable scatter in the data, oxide growth appears to follow sub-parabolic kinetics or to slow down after approximately 5,000–9,000 h [14,151,284–286]. Furthermore, in stacks using AISI 441 interconnects, discontinuous Si-rich subscale formation has been reported; however, the authors concluded that any effect on ASR is likely negligible [287].

Protective coatings largely suppress chromium poisoning of the cathode, although $SrCrO_4$ formation has been reported in some cases [284,289]. In addition, solid-state diffusion resulted in Cr and Fe incorporation into the coating [284,285,287].

Interdiffusion between the interconnect and the Ni contact is widely reported and results in local austenitization [151,283,287]. In

contrast, σ-phase formation, which has been reported in laboratory experiments, was not observed in the stack analyses. In carbon-containing fuels, Cr-carbide formation additionally lowered the Cr activity at the interface [282].

None of the published studies reported a clear dual-atmosphere effect, which is commonly attributed to pre-oxidation during the start-up phase [284,287]. Furthermore, operating temperatures above 700 °C are expected to reduce the severity of the dual atmosphere effect. In contrast, Fig. 10b clearly shows evidence of a dual-atmosphere effect in a stack operated at 600 °C.

Li et al. performed short term stack tests using AISI 430 to investigate the effect of current and indeed found such an effect [279]. However, Ghiara et al.[285] (air side) and Piccardo et al. [151] compared oxide-scale thicknesses after up to 40,000 h in gas-channel regions and areas in electrical contact with the cathode and concluded that current had no significant effect. Likewise, no other post-mortem study reports a measurable effect on oxide-scale thickness, although some authors suggest that current may influence diffusion processes.

9. Summary and outlook

Ferritic stainless steels will remain the dominant metallic interconnect materials for planar solid oxide electrolysis cells because they offer the most viable combination of thermal expansion compatibility, electrical conductivity, manufacturability, availability, and cost. Their lifetime is nevertheless limited by the growth and eventual breakdown of chromia-based oxide scales. On the oxygen side, the growth of the duplex $Cr_2O_3/(Cr,Mn)_3O_4$ scale increases the area-specific resistance with time, while Cr(VI) volatilization causes additional chromium depletion and electrode contamination in particular when steam is present. On the oxygen side, chromium volatilization is generally less critical in SOEC than in SOFC due to lower flow rate and drier atmosphere. Nevertheless, protective coatings are expected to remain important for limiting chromia growth rate and reducing ASR. They may also enable the use of interconnects in reversible solid oxide cells.

The fuel/steam side presents different and less well-understood challenges. At approximately 800 °C, Mn-containing ferritic steels commonly form protective duplex scales with oxidation rates comparable to those in air. At lower temperatures, particularly around 600 to 650 °C, steam-rich H_2/H_2O atmospheres can instead cause rapid formation of Fe-rich, non-protective oxides. Lowering the operating temperature therefore does not necessarily result in a longer service lifetime.

Under dual-atmosphere conditions, hydrogen transport through the steel can additionally promote localized breakaway oxidation on the oxygen side. Although this effect is experimentally well established under certain conditions, the mechanisms by which hydrogen affects chromium and oxygen transport, particularly along alloy grain boundaries, remain unresolved.

There is consequently no universally best SOEC interconnect material. Material selection requires a system-specific trade-off among corrosion resistance, electrical performance, cost, manufacturability, and compatibility with the cell and stack design. For electrolyte-supported cells operating at comparatively high temperatures, high-chromium ferritic steels with reactive-element additions, such as Crofer 22 APU or functionally equivalent grades, may be preferred because of their larger chromium reservoir and improved scale adherence along with a reduced oxide growth rate. Below approximately 700 °C, less highly alloyed and less expensive steels such as AISI 441/430 may provide adequate performance, provided that surface condition, thermal pre-treatment, coating, contact design, and operating history are carefully controlled. A suitable oxygen-side coating generally remains advisable. On the steam side, controlled pre-oxidation is currently among the most promising mitigation measures, although its effectiveness under high-steam SOEC inlet conditions and repeated cycling has not been sufficiently validated. The state of the art is therefore not a single alloy-coating combination, but a materials system tailored to the stack design and operating conditions.

This need for system-specific optimization also defines the most important directions for future work. Most published studies rely on steady-state, isothermal exposures, whereas SOEC operation includes heating and cooling, start-up and shutdown, current fluctuations, interruptions in steam supply, fuel-gas switching, local gas-composition gradients, and transitions between electrolysis and standby or fuel-cell operation. Thermal history of the interconnect deserves particular attention because heating rate, surface condition, and pre-oxidation can determine whether protective or Fe-rich oxides form. However, systematic studies under representative operating cycles remain scarce. Pressure effects likewise require dedicated investigation. The limited data on transient operation, pressure, applied current, and interactions of interconnects with sealing and contact materials represent important gaps between laboratory testing and industrial operation. The present review focuses on steam electrolysis, but the use of CO_2-containing feedstocks in co-electrolysis for syngas production introduces additional degradation mechanisms. Depending on gas composition, temperature, pressure, and conversion, carbon-containing species may promote carburization and additional degradation mechanisms.

A comprehensive lifetime model would be highly valuable, but model development alone is insufficient. The central challenge is validation against long-term stack operation. A useful model must account for chromium depletion, non-parabolic oxidation, component thickness, temperature and non-steady state operation. Validation requires detailed operating histories together with post-test characterization of interconnects from representative stacks. Much of the most relevant knowledge is now generated within industry. These data are rarely published in sufficient detail, creating an increasing gap between laboratory research and industrial experience.

Interconnect development should also extend beyond corrosion performance to cost, manufacturability, resource efficiency, and end-of-life recovery. Ferritic stainless steels are compatible with established recycling routes, but coatings, contact materials, and joining processes may complicate recovery. Future development should therefore consider design for recycling and reduced dependence on critical elements alongside durability and electrical performance.

The objective is not to identify a universally optimal material, but to establish manufacturable and economically viable interconnect systems whose durability has been validated under representative SOEC operating conditions.

CRediT authorship contribution statement

Kerem Ozgur Gunduz: Writing – review & editing, Writing – original draft, Conceptualization. **Mareddy Reddy:** Writing – review & editing, Writing – original draft, Conceptualization. **Anton Chyrkin:** Writing – review & editing, Writing – original draft. **Jan Froitzheim:** Writing – review & editing, Writing – original draft, Funding acquisition, Conceptualization.

Declaration of competing interest

The authors declare that they have no known competing financial interests or personal relationships that could have appeared to influence the work reported in this paper.

Acknowledgements

The authors gratefully acknowledge valuable discussions and insights from Tobias Holt Nørby (Topsoe), Robert Leah (Ceres Power), and Jouni Puranen (Elcogen), whose industrial perspectives helped to shape this review. JF gratefully acknowledges funding by Nordic Energy Research through the MoreH2 project.

Data availability

Data will be made available on request.

References

[1] Battelle Memorial Institute. Manufacturing cost analysis of 1 kw and 5 kw solid oxide fuel cell (Sofc) for auxiliary power applications; 2014.
[2] Prosser JH, James BD, Murphy BM, Wendt DS, Casteel MJ, Westover TL, et al. Cost analysis of hydrogen production by high-temperature solid oxide electrolysis. Int J Hydrogen Energy 2024;49:207–27.
[3] Battelle Memorial Institute. Manufacturing Cost Analysis of 1, 5, 10 and 25 kW Fuel Cell Systems for Primary Power and Combined Heat and Power Applications. 2017.
[4] Beyrami J, Nakashima RN, Nemati A, Frandsen HL. Lifetime and performance of solid oxide electrolysis stacks and systems under different operation modes and conditions. Int J Hydrogen Energy 2025;102:980–95.
[5] Quadakkers WJ, Piron-Abellan J, Shemet V, Singheiser L. Metallic interconnectors for solid oxide fuel cells – a review. Mater High Temp 2003;20:115–27.
[6] Küngas R, Blennow P, Heiredal-Clausen T, Holt T, Rass-Hansen J, Primdahl S, et al. eCOs - a commercial CO2 electrolysis system developed by Haldor Topsoe. ECS Trans 2017;78:2879.
[7] Hodjati-Pugh O, Dhir A, Steinberger-Wilckens R. The development of current collection in micro-tubular solid oxide fuel cells—a review. Appl Sci 2021;11:1077.
[8] Han S, Wei T, Wang S, Zhu Y, Guo X, He L, et al. Recent progresses in the development of tubular segmented-in-series solid oxide fuel cells: Experimental and numerical study. Int J Miner Metall Mater 2024;31:427–42.
[9] Kofstad P. High Temperature Corrosion. London and New York: Elsevier Applied Science Publishers Ltd.; 1988.
[10] Young DJ. High temperature oxidation and corrosion of metals, vol. 1. Elsevier; 2008.
[11] Fontana S, Chevalier S, Caboche G. Metallic Interconnects for Solid Oxide fuel Cell: Performance of Reactive Element Oxide Coating during 10, 20 and 30 months Exposure. Oxid Met 2012;78:307–28.
[12] Canovic S, Froitzheim J, Sachitanand R, Nikumaa M, Halvarsson M, Johansson L-G, et al. Oxidation of Co- and Ce-nanocoated FeCr steels: a microstructural investigation. Surf Coat Technol 2013;215:62–74.
[13] Sachitanand R, Sattari M, Svensson J-E, Froitzheim J. Evaluation of the oxidation and Cr evaporation properties of selected FeCr alloys used as SOFC interconnects. Int J Hydrogen Energy 2013;38:15328–34.
[14] Linder M, Hocker T, Holzer L, Friedrich KA, Iwanschitz B, Mai A, et al. Cr2O3 scale growth rates on metallic interconnectors derived from 40,000 h solid oxide fuel cell stack operation. J Power Sources 2013;243:508–18.
[15] Yamamura K, Uehara T, Tanaka S, Yasuda N. Oxidation Behavior of Fe-Cr Ferritic Alloy for SOFC Interconnects ZMG232G10 in Air and H2/H2O. ECS Trans 2013;57:2177.
[16] Huczkowski P, Christiansen N, Shemet V, Niewolak L, Piron-Abellan J, Singheiser L, et al. Growth Mechanisms and Electrical Conductivity of Oxide Scales on Ferritic Steels Proposed as Interconnect Materials for SOFC's. Fuel Cells 2006;6:93–9.
[17] Niewolak L, Young DJ, Hattendorf H, Singheiser L, Quadakkers WJ. Mechanisms of Oxide Scale Formation on Ferritic Interconnect Steel in simulated Low and High pO2 Service Environments of Solid Oxide fuel Cells. Oxid Met 2014;82:123–43.
[18] Reisert M, Aphale AN, Anisur MR, Belko S, Yaginuma M, Shiomi T, et al. Controlled thermal pre-treatment of ZMG232G10® for corrosion mitigation under simulated SOFC interconnect exposure conditions. Int J Hydrogen Energy 2023;48:18420–32.
[19] Niewolak L, Wessel E, Singheiser L, Quadakkers WJ. Potential suitability of ferritic and austenitic steels as interconnect materials for solid oxide fuel cells operating at 600°C. J Power Sources 2010;195:7600–8.
[20] Kim BK, Ko YS, Jung I-H, Han HN, Yi K-W, Kim D-I. Role of the alloy grain boundaries in the high-temperature oxidation and Cr volatilization of 22 wt% Cr ferritic stainless steel for SOFC applications. Corros Sci 2023;213:110940.
[21] Pillai R, Chyrkin A, Quadakkers WJ. Modeling in high temperature corrosion: a review and outlook. Oxid Met 2021;96:385–436.
[22] Chyrkin A, Froitzheim J. Premature breakaway oxidation of ferritic stainless steels triggered by austenitization. Corros Sci 2025;256:113260.
[23] Chyrkin A, Quadakkers WJ. Effect of α-to-γ transformation on internal oxidation in FeCr-base alloys in dry and wet gases. J Alloy Compd 2025;1045:184722.
[24] Chyrkin A, Froitzheim J, Zurek J, Naumenko D. Austenitization triggering breakaway oxidation of FeCr-base alloys at 900 °C. Corros Sci 2025;244:112605.
[25] Galerie A, Petit JP, Wouters Y, Mougin J, Srisrual A, Hou PY. Water vapour effects on the oxidation of chromia-forming alloys. Mater. Sci. Forum, vol. 696, Trans Tech Publ; 2011, p. 200–5.
[26] Bataillou L, Desgranges C, Martinelli L, Monceau D. Modelling of the effect of grain boundary diffusion on the oxidation of Ni-Cr alloys at high temperature. Corros Sci 2018;136:148–60.
[27] Sabioni ACS, Souza JNV, Ji V, Jomard F, Trindade VB, Carneiro JF. Study of ion diffusion in oxidation films grown on a model Fe–15%Cr alloy. Solid State Ion 2015;276:1–8.
[28] Tedmon CS. The effect of Oxide Volatilization on the Oxidation Kinetics of Cr and Fe-Cr Alloys. J Electrochem Soc 1966;113:766.
[29] Asteman H, Svensson J-E, Norell M, Johansson L-G. Influence of water vapor and flow rate on the high-temperature oxidation of 304L; effect of chromium oxide hydroxide evaporation. Oxid Met 2000;54:11–26.

[30] Froitzheim J, Ravash H, Larsson E, Johansson LG, Svensson JE. Investigation of chromium volatilization from FeCr interconnects by a denuder technique. J Electrochem Soc 2010;157:B1295.
[31] Falk-Windisch H, Svensson JE, Froitzheim J. The effect of temperature on chromium vaporization and oxide scale growth on interconnect steels for Solid Oxide fuel Cells. J Power Sources 2015;287:25–35.
[32] Goebel C, Berger R, Bernuy-Lopez C, Westlinder J, Svensson J-E, Froitzheim J. Long-term (4 year) degradation behavior of coated stainless steel 441 used for solid oxide fuel cell interconnect applications. J Power Sources 2020;449:227480.
[33] Huczkowski P, Shemet V, Piron-Abellan J, Singheiser L, Quadakkers WJ, Christiansen N. Oxidation limited life times of chromia forming ferritic steels. Mater Corros 2004;55:825–30.
[34] Galerie A, Henry S, Wouters Y, Mermoux M, Petit J-P, Antoni L. Mechanisms of chromia scale failure during the course of 15–18Cr ferritic stainless steel oxidation in water vapour. Mater High Temp 2005;22:105–12.
[35] Pujilaksono B, Jonsson T, Heidari H, Halvarsson M, Svensson J-E, Johansson L-G. Oxidation of Binary FeCr Alloys (Fe–2.25Cr, Fe–10Cr, Fe–18Cr and Fe–25Cr) in O2 and in O2 + H2O Environment at 600 °C. Oxid Met 2011;75:183–207.
[36] Wagner C. Theoretical analysis of the diffusion processes determining the oxidation rate of alloys. J Electrochem Soc 1952;99:369.
[37] Wagner C. Reaktionstypen bei der Oxydation von Legierungen. Zeitschrift Für Elektrochemie, Berichte Der Bunsengesellschaft Für Physikalische Chemie 1959; 63:772–82.
[38] Nanko M, Do DTM. Oxide nano-rod array structure via a simple metallurgical process. IOP Conf Ser: Mater Sci Eng 2011;20:012012.
[39] Gesmundo F, Viani F, Niu Y. The internal oxidation of two-phase binary alloys beneath an external scale of the less-stable oxide. Oxid Met 1997;47:355–80.
[40] Chyrkin A, Froitzheim J, Quadakkers WJ. Transition from Internal to External Oxidation in Binary Fe–Cr Alloys around 900 °C. High Temp Corros Mater 2024; 102:3.
[41] Meijering JL. On the diffusion of oxygen through solid iron. Acta Metall 1955;3:157–62.
[42] Swisher JH, Turkdogan ET. Solubility, permeability, and diffusivity of oxygen in solid iron. AIME Met Soc Trans 1967;239:426–31.
[43] Chyrkin A, Cossu C, Svensson J-E, Froitzheim J. Internal Oxidation of a Fe–Cr Binary Alloy at 700–900 °C: the Role of Hydrogen and Water Vapor. Oxid Met 2022;98:273–89.
[44] Setiawan AR, Hanafi Bin Ani M, Ueda M, Kawamura K, Maruyama T. Oxygen Permeability through Internal Oxidation Zone in Fe-Cr Alloys under Dry and Humid Conditions at 973 and 1 073 K. ISIJ Int. 2010;50:259–63.
[45] Takada J, Adachi M. Determination of diffusion coefficient of oxygen in α-iron from internal oxidation measurements in Fe-Si alloys. J Mater Sci 1986;21: 2133–7.
[46] Takada J, Yamamoto S, Kikuchi S, Adachi M. Internal oxidation of Fe-Al alloys in the α-phase region. Oxid Met 1986;25:93–105.
[47] Williams PI, Faulkner RG. Chemical volume diffusion coefficients for stainless steel corrosion studies. J Mater Sci 1987;22:3537–42.
[48] Whittle DP, Wood GC, Evans DJ, Scully DB. Concentration profiles in the underlying alloy during the oxidation of iron-chromium alloys. Acta Metall 1967;15: 1747–55.
[49] Alberry PJ, Haworth CW. Interdiffusion of Cr, Mo, and W in Iron. Met Sci 1974;8:407–12.
[50] Brylewski T, Molin S, Stygar M, Bik M, Jeleń P, Sitarz M, et al. Oxidation kinetics and electrical properties of oxide scales formed under exposure to air and Ar–H_2-H_2O atmospheres on the Crofer 22 H ferritic steel for high-temperature applications such as interconnects in solid oxide cell stacks. Int J Hydrogen Energy 2024;94:209–22.
[51] Meier GH, Jung K, Mu N, Yanar NM, Pettit FS, Pirón Abellán J, et al. Effect of Alloy Composition and Exposure Conditions on the Selective Oxidation Behavior of Ferritic Fe–Cr and Fe–Cr–X Alloys. Oxid Met 2010;74:319–40.
[52] Whittle DP. The oxidation of finite samples of heat-resistant alloys. Corros Sci 1972;12:869–72.
[53] Cowen HC, Webster SJ. Chromium depletion during oxidation of stainless steel foils. Corrosion of steels in CO_2. Proceedings of the British Nuclear Energy Society international conference at Reading University, 23-24 September 1974, 1974.
[54] Quadakkers WJ, Bongartz K. The prediction of breakaway oxidation for alumina forming ODS alloys using oxidation diagrams. Mater Corros 1994;45:232–41.
[55] Young DJ, Chyrkin A, Quadakkers WJ. A simple Expression for predicting the Oxidation Limited Life of Thin Components Manufactured from FCC High Temperature Alloys. Oxid Met 2012;77:253–64.
[56] Evans HE, Donaldson AT, Gilmour TC. Mechanisms of breakaway oxidation and application to a chromia-forming steel. Oxid Met 1999;52:379–402.
[57] Chyrkin A, Gunduz KO, Asokan V, Svensson J-E, Froitzheim J. High temperature oxidation of AISI 441 in simulated solid oxide fuel cell anode side conditions. Corros Sci 2022;203:110338.
[58] Chen J, Zhang J, Young DJ. Effect of hydrogen on oxidation of Fe-20Cr-(1Si, 2Mn or 2Al) alloys in water vapour at 650 °C. Corros Sci 2025;251:112932.
[59] Young DJ, Zurek J, Singheiser L, Quadakkers WJ. Temperature dependence of oxide scale formation on high-Cr ferritic steels in Ar–H2–H2O. Corros Sci 2011; 53:2131–41.
[60] Kleinschmager H, Reich A. Notizen: Allox-Leiter zur elektrischen Serienschaltung von Hochtemperatur-Brennstoffzellen / All-ox Conductor for Series connection of High-Temperature fuel. Cells 1972;27:363–5.
[61] Martinz H-P, Köck W, Sakaki T. Ducropur, Ducrolloy-New chromium materials. J Phys IV 1993;3:C9–205.
[62] Quadakkers WJ, Shemet V, Singheiser L. Material used at high temperatures. EP1287571B1, 2001.
[63] Jiao Z, Shikazono N, Kasagi N. Performance of an anode support solid oxide fuel cell manufactured by microwave sintering. J Power Sources 2010;195:151–4.
[64] Udomsilp D, Rechberger J, Neubauer R, Bischof C, Thaler F, Schafbauer W, et al. Metal-Supported Solid Oxide fuel Cells with Exceptionally High Power Density for Range Extender Systems. Cell Rep Phys Sci 2020;1.
[65] Hammer JE, Laney SJ, Jackson RW, Coyne K, Pettit FS, Meier GH. The Oxidation of Ferritic Stainless Steels in simulated Solid-Oxide Fuel-Cell Atmospheres. Oxid Met 2007;67:1–38.
[66] Xiong W, Hedström P, Selleby M, Odqvist J, Thuvander M, Chen Q. An improved thermodynamic modeling of the Fe–Cr system down to zero kelvin coupled with key experiments. Calphad 2011;35:355–66.
[67] Garcia-Fresnillo L, Shemet V, Chyrkin A, de Haart LGJ, Quadakkers WJ. Long-term behaviour of solid oxide fuel cell interconnect materials in contact with Ni-mesh during exposure in simulated anode gas at 700 and 800 °C. J Power Sources 2014;271:213–22.
[68] Stanislowski M, Froitzheim J, Niewolak L, Quadakkers WJ, Hilpert K, Markus T, et al. Reduction of chromium vaporization from SOFC interconnectors by highly effective coatings. J Power Sources 2007;164:578–89.
[69] Sakai N, Horita T, Yamaji K, Xiong YP, Kishimoto H, Brito ME, et al. Material transport and degradation behavior of SOFC interconnects. Solid State Ion 2006; 177:1933–9.
[70] Hua B, Kong Y, Zhang W, Pu J, Chi B, Jian L. The effect of Mn on the oxidation behavior and electrical conductivity of Fe–17Cr alloys in solid oxide fuel cell cathode atmosphere. J Power Sources 2011;196:7627–38.
[71] Kim T-H, Song R-H, Mehran MT, Joh D-W, Hussain A, Lee S-B, et al. Effects of Mn concentration on durability of Fe-Cr ferritic steels dispersed with La_2O_3 for solid oxide fuel cell interconnects. J Power Sources 2024;594:234020.
[72] Yang Z, Xia G-G, Maupin GD, Stevenson JW. Evaluation of Perovskite Overlay Coatings on Ferritic Stainless Steels for SOFC Interconnect applications. J Electrochem Soc 2006;153:A1852.
[73] Bakhshi-Zadeh A, Salmani S, Faghihi-Sani MA, Abdoli H, Jalili N. Oxidation behavior and electrical properties of de-siliconized AISI 430 Alloy with Mn1.5Co1.5O4 Coating for Solid Oxide fuel Cell Interconnect. Oxid Met 2020;93:401–15.
[74] Stott FH, Gabriel GJ, Wei FI, Wood GC. The development of silicon-containing oxides during the oxidation of iron-chromium-base alloys. Mater Corros 1987; 38:521–31.
[75] Horita T, Yamaji K, Yokokawa H, Toji A, Uehara T, Ogasawara K, et al. Effects of Si and Al concentrations in Fe–Cr alloy on the formation of oxide scales in H2–H2O. Int J Hydrogen Energy 2008;33:6308–15.

[76] Vayyala A, Povstugar I, Galiullin T, Naumenko D, Quadakkers WJ, Hattendorf H, et al. Effect of Nb Addition on Oxidation Mechanisms of High Cr Ferritic Steel in Ar–H_2–H_2O. Oxid Met 2019;92:471–91.
[77] Vayyala A, Povstugar I, Naumenko D, Quadakkers WJ, Hattendorf H, Mayer J. A Nanoscale Study of Thermally Grown Chromia on High-Cr Ferritic Steels and Associated Oxidation Mechanisms. J Electrochem Soc 2020;167:061502.
[78] Froitzheim J, Meier GH, Niewolak L, Ennis PJ, Hattendorf H, Singheiser L, et al. Development of high strength ferritic steel for interconnect application in SOFCs. J Power Sources 2008;178:163–73.
[79] Ishikawa S, Yamashita T, Kiryu T, Chai YW, Kimura Y. Effect of Mo addition on laves phase precipitation behavior in Fe-20%Cr-x%Nb alloys. Mater Charact 2022;190:112077.
[80] Azevedo CRF, Padilha AF. The most frequent failure causes in super ferritic stainless steels: are they really super? Procedia Struct Integr 2019;17:331–8.
[81] Holt A, Kofstad P. Electrical conductivity of Cr2O3 doped with TiO_2. Solid State Ion 1999;117:21–5.
[82] Abellan JP, Quadakkers WJ. Development of ferritic steels for application as interconnect materials for intermediate temperature solid oxide fuel cells (SOFCs) 2005.
[83] Inoue Y, Hiraide N, Hayashi A, Ushioda K. Effect of Titanium on Oxidation Behavior of High-Purity Ferritic Stainless Steel. Mater Trans 2019;60:1968–76.
[84] Chevalier S. What did we learn on the reactive element effect in chromia scale since Pfeil's patent? Mater Corros 2014;65:109–15.
[85] Hou PY. The Reactive Element effect – past, present and Future. Mater Sci Forum 2011;696:39–44.
[86] Pint BA. Progress in understanding the reactive element effect since the Whittle and Stringer literature review. John Stringer Symposium on High Temperature Corrosion 2001:9–19.
[87] Yasuda N, Uehara T, Okamoto M, Aoki C, Ohno T, Toji A. Improvement of Oxidation Resistance of Fe-Cr Ferritic Alloy Sheets for SOFC Interconnects. ECS Trans 2009;25:1447.
[88] Jo KH, Kim JH, Kim KM, Lee IS, Kim SJ. Development of a new cost effective Fe-Cr ferritic stainless steel for SOFC interconnect. Int J Hydrogen Energy 2015;40:9523–9.
[89] Knoth RJ. High purity ferritic Cr Mo stainless steel – five years' successful fight against corrosion in the process industry. Mater Corros 1977;28:409–16.
[90] Therma 22FCTM stainless steel is the long-lasting choice for fuel cells and electrolyzers | Outokumpu 2025.
[91] JFE Steel's New Ferritic Stainless Steel for SOFC Interconnects Achieves Oxidation Resistance and Conductivity without Requiring Coating |JFE Steel Corporation 2025.
[92] Reddy MJ, Chausson TE, Svensson JE, Froitzheim J. 11–23% Cr steels for solid oxide fuel cell interconnect applications at 800 °C – how the coating determines oxidation kinetics. Int J Hydrogen Energy 2023;48:12893–904.
[93] Talic B, Venkatachalam V, Hendriksen PV, Kiebach R. Comparison of MnCo2O4 coated Crofer 22 H, 441, 430 as interconnects for intermediate-temperature solid oxide fuel cell stacks. J Alloy Compd 2020;821:153229.
[94] Horita T, Xiong Y, Yamaji K, Sakai N, Yokokawa H. Stability of Fe–Cr alloy interconnects under CH_4–H_2O atmosphere for SOFCs. J Power Sources 2003;118:35–43.
[95] Alnegren P, Sattari M, Froitzheim J, Svensson JE. Degradation of ferritic stainless steels under conditions used for solid oxide fuel cells and electrolyzers at varying oxygen pressures. Corros Sci 2016;110:200–12.
[96] Zhang K, El-Kharouf A, Caykara T, Steinberger-Wilckens R. Effect of Temperature and Water Content on the Oxidation Behaviour and Cr Evaporation of High-Cr Alloys for SOFC Cathode Air Preheaters. High Temp Corros Mater 2023;100:21–45.
[97] Sand T, Geers C, Cao Y, Svensson JE, Johansson LG. Effective reduction of chromium-oxy-hydroxide evaporation from Ni-base alloy 690. Oxid Met 2019;92:259–79.
[98] Reddy MJ, Svensson J-E, Froitzheim J. Reevaluating the Cr evaporation characteristics of Ce/Co coatings for interconnect applications. ECS Trans 2021;103:1899–905.
[99] Key C, Eziashi J, Froitzheim J, Amendola R, Smith R, Gannon P. Methods to Quantify Reactive Chromium Vaporization from Solid Oxide fuel Cell Interconnects. J Electrochem Soc 2014;161:C373.
[100] Dogdibegovic E, Ibanez S, Wallace A, Kopechek D, Arkenberg G, Swartz S, et al. Performance of stainless steel interconnects with (Mn,Co)3O4-based coating for solid oxide electrolysis. Int J Hydrogen Energy 2022;47:24279–86.
[101] Zhou L, Mason JH, Li W, Liu X. Comprehensive review of chromium deposition and poisoning of solid oxide fuel cells (SOFCs) cathode materials. Renew Sustain Energy Rev 2020;134:110320.
[102] Huang K. A thermodynamic perspective on electrode poisoning in solid oxide fuel cells. Int J Miner Metall Mater 2024;31:1449–55.
[103] Bentzen JJ, Høgh JVT, Barfod R, Hagen A. Chromium poisoning of LSM/YSZ and LSCF/CGO composite cathodes. Fuel Cells 2009;9:823–32.
[104] Jiang SP, Chen X. Chromium deposition and poisoning of cathodes of solid oxide fuel cells - a review. Int J Hydrogen Energy 2014;39:505–31.
[105] Horita T. Chromium poisoning for prolonged lifetime of electrodes in solid oxide fuel cells - Review. Ceram Int 2021;47:7293–306.
[106] Harrison CM, Slater PR, Steinberger-Wilckens R. A review of Solid Oxide fuel Cell cathode materials with respect to their resistance to the effects of chromium poisoning. Solid State Ion 2020;354:115410.
[107] Zhu Z, Sugimoto M, Pal U, Gopalan S, Basu S. Multiple cycle chromium poisoning and in-situ electrochemical cleaning of LSM-based solid oxide fuel cell cathodes. J Power Sources Adv 2020;6:100037.
[108] Zhu Z, Sugimoto M, Pal U, Gopalan S, Basu S. Electrochemical cleaning: an in-Situ method to reverse chromium poisoning in solid oxide fuel cell cathodes. J Power Sources 2020;471:228474.
[109] Vayyala A, Povstugar I, Naumenko D, Quadakkers WJ, Hattendorf H, Mayer J. Effect of gas composition on the oxide scale growth mechanisms in a ferritic steel for solid oxide cell interconnects. Corros Sci 2023;221:111317.
[110] Lu Z, Zhu J, Payzant EA, Paranthaman MP. Electrical Conductivity of the Manganese Chromite Spinel Solid solution. J Am Ceram Soc 2005;88:1050–3.
[111] Crawford JA, Vest RW. Electrical Conductivity of Single-Crystal Cr_2O_3. J Appl Phys 1964;35:2413–8.
[112] Holt A, Kofstad P. Electrical conductivity and defect structure of Mg-doped Cr_2O_3. Solid State Ion 1997;100:201–9.
[113] Holt A, Kofstad P. Electrical conductivity and defect structure of Cr_2O_3. II. Reduced temperatures (<~1000°C). Solid State Ion 1994;69:137–43.
[114] Mareddy Jayanth Reddy. Metallic materials for solid oxide fuel cells and electrolysers - Mitigating high temperature corrosion. PhD Thesis Chalmers University of Technology 2023.
[115] Mikkelsen L. High temperature oxidation of iron-chromium alloys. Technical University of Denmark; 2003. PhD Thesis.
[116] Alman DE, Jablonski PD. Effect of minor elements and a Ce surface treatment on the oxidation behavior of an Fe-22Cr-0.5Mn (Crofer 22 APU) ferritic stainless steel. Int J Hydrogen Energy 2007;32:3743–53.
[117] Fontana S, Chevalier S, Caboche G. Metallic interconnects for solid oxide fuel cell: Performance of reactive element oxide coating during long time exposure. Mater Corros 2011;62:650–8.
[118] Grolig JG, Froitzheim J, Svensson JE. Coated stainless steel 441 as interconnect material for solid oxide fuel cells: Oxidation performance and chromium evaporation. J Power Sources 2014;248:1007–13.
[119] Grolig JG, Froitzheim J, Svensson JE. Coated stainless steel 441 as interconnect material for solid oxide fuel cells: Evolution of electrical properties. J Power Sources 2015;284:321–7.
[120] Yang Z, Xia GG, Maupin GD, Stevenson JW. Conductive protection layers on oxidation resistant alloys for SOFC interconnect applications. Surf Coat Technol 2006;201:4476–83.
[121] Grolig JG, Alnegren P, Froitzheim J, Svensson JE. Copper Iron Conversion Coating for Solid Oxide fuel Cell Interconnects. J Power Sources 2015;297:534–9.
[122] Falk-Windisch H, Claquesin J, Sattari M, Svensson JE, Froitzheim J. Co- and Ce/Co-coated ferritic stainless steel as interconnect material for Intermediate Temperature Solid Oxide fuel Cells. J Power Sources 2017;343:1–10.
[123] Tomas M, Asokan V, Puranen J, Svensson JE, Froitzheim J. Efficiencies of cobalt- and copper-based coatings applied by different deposition processes for applications in intermediate-temperature solid oxide fuel cells. Int J Hydrogen Energy 2022;47:32628–40.

[124] Zhao Q, Geng S, Chen G, Wang F. Application of sputtered NiFe2 alloy coating for SOFC interconnect steel. J Alloy Compd 2018;769:120–9.
[125] Hua B, Zhang W, Wu J, Pu J, Chi B, Jian L. A promising $NiCo_2O_4$ protective coating for metallic interconnects of solid oxide fuel cells. J Power Sources 2010;195:7375–9.
[126] Paknahad P, Askari M, Ghorbanzadeh M. Application of sol–gel technique to synthesis of copper–cobalt spinel on the ferritic stainless steel used for solid oxide fuel cell interconnects. J Power Sources 2014;266:79–87.
[127] Dayaghi AM, Askari M, Gannon P. Pre-treatment and oxidation behavior of sol–gel Co coating on 430 steel in 750 °C air with thermal cycling. Surf Coat Technol 2012;206:3495–500.
[128] Jalilvand G, Faghihi-Sani MA. Fe doped Ni–Co spinel protective coating on ferritic stainless steel for SOFC interconnect application. Int J Hydrogen Energy 2013;38:12007–14.
[129] Sabato AG, Zanchi E, Molin S, Cempura G, Javed H, Herbrig K, et al. Mn-Co spinel coatings on Crofer 22 APU by electrophoretic deposition: up scaling, performance in SOFC stack at 850 °C and compositional modifications. J Eur Ceram Soc 2021;41:4496–504.
[130] Sun Z, Wang R, Nikiforov AY, Gopalan S, Pal UB, Basu SN. CuMn1.8O4 protective coatings on metallic interconnects for prevention of Cr-poisoning in solid oxide fuel cells. J Power Sources 2018;378:125–33.
[131] Zanchi E, Sabato AG, Molin S, Cempura G, Boccaccini AR, Smeacetto F. Recent advances on spinel-based protective coatings for solid oxide cell metallic interconnects produced by electrophoretic deposition. Mater Lett 2021;286:129229.
[132] Zanchi E, Talic B, Sabato AG, Molin S, Boccaccini AR, Smeacetto F. Electrophoretic co-deposition of Fe2O3 and $Mn_{1.5}Co_{1.5}O_4$: Processing and oxidation performance of Fe-doped Mn-Co coatings for solid oxide cell interconnects. J Eur Ceram Soc 2019;39:3768–77.
[133] Pinto R, Carmezim MJ, Montemor MF. Electrodeposition and isothermal aging of Co and Mn layers on stainless steel for interconnectors: initial stages of spinel phase formation. J Power Sources 2014;255:251–9.
[134] Fu QX, Sebold D, Tietz F, Buchkremer HP. Electrodeposited cobalt coating on Crofer22APU steels for interconnect applications in solid oxide fuel cells. Solid State Ion 2011;192:376–82.
[135] Lee S-I, Hong J, Kim H, Son J-W, Lee J-H, Kim B-K, et al. Highly dense Mn-Co spinel coating for protection of metallic interconnect of solid oxide fuel cells. J Electrochem Soc 2014;161:F1389–94.
[136] Lenka RK, Patro PK, Sharma J, Mahata T, Sinha PK. Evaluation of $La_{0.75}Sr_{0.25}Cr_{0.5}Mn_{0.5}O_3$ protective coating on ferritic stainless steel interconnect for SOFC application. Int J Hydrogen Energy 2016;41:20365–72.
[137] Xie Y, Qu W, Yao B, Shaigan N, Rose L. Dense protective coatings for SOFC interconnect deposited by spray pyrolysis. ECS Trans 2010;26:357–62.
[138] Talic B, Hendriksen PV, Wiik K, Lein HL. Thermal expansion and electrical conductivity of Fe and Cu doped $MnCo_2O_4$ spinel. Solid State Ion 2018;326:90–9.
[139] Mehdizade M, Smeacetto F, Winiarski M, Molin S. Effect of process parameters on properties of $Mn_{1.5}CuFe_{0.5}O_4$ spinel oxide coatings deposited by spray pyrolysis method. Int J Hydrogen Energy 2025;130:213–29.
[140] Pandiyan S, Bianco M, El-Kharouf A, Tomov RI, Steinberger-Wilckens R. Evaluation of inkjet-printed spinel coatings on standard and surface nitrided ferritic stainless steels for interconnect application in solid oxide fuel cell devices. Ceram Int 2022;48:20456–66.
[141] Han GD, Neoh KC, Bae K, Choi HJ, Park SW, Son JW, et al. Fabrication of lanthanum strontium cobalt ferrite (LSCF) cathodes for high performance solid oxide fuel cells using a low price commercial inkjet printer. J Power Sources 2016;306:503–9.
[142] Ajitdoss LC, Smeacetto F, Bindi M, Beretta D, Salvo M, Ferraris M. Mn1.5Co1.5O4 protective coating on Crofer22APU produced by thermal co-evaporation for SOFCs. Mater Lett 2013;95:82–5.
[143] Molin S, Sabato AG, Bindi M, Leone P, Cempura G, Salvo M, et al. Microstructural and electrical characterization of Mn-Co spinel protective coatings for solid oxide cell interconnects. J Eur Ceram Soc 2017;37:4781–91.
[144] Spotorno R, Piccardo P, Perrozzi F, Valente S, Viviani M, Ansar A. Microstructural and Electrical Characterization of Plasma Sprayed Cu-Mn Oxide Spinels as Coating on Metallic Interconnects for Stacking Solid Oxide fuel Cells. Fuel Cells 2015;15:728–34.
[145] Grünwald N, Sohn YJ, Yin X, Menzler NH, Guillon O, Vaßen R. Microstructure and phase evolution of atmospheric plasma sprayed Mn-Co-Fe oxide protection layers for solid oxide fuel cells. J Eur Ceram Soc 2019;39:449–60.
[146] Vaßen R, Grünwald N, Marcano D, Menzler NH, Mücke R, Sebold D, et al. Aging of atmospherically plasma sprayed chromium evaporation barriers. Surf Coat Technol 2016;291:115–22.
[147] Grünwald N, Lhuissier P, Salvo L, Villanova J, Menzler NH, Guillon O, et al. In situ investigation of atmospheric plasma-sprayed Mn–Co–Fe–O by synchrotron X-ray nano-tomography. J Mater Sci 2020;55:12725–36.
[148] Puranen J, Pihlatie M, Lagerbom J, Salminen T, Laakso J, Hyvärinen L, et al. Influence of powder composition and manufacturing method on electrical and chromium barrier properties of atmospheric plasma sprayed spinel coatings prepared from MnCo2O4 and Mn_2CoO_4 + Co powders on Crofer 22 APU interconnectors. Int J Hydrogen Energy 2014;39:17246–57.
[149] Reddy MJ, Kamecki B, Talic B, Zanchi E, Smeacetto F, Hardy JS, et al. Experimental review of the performances of protective coatings for interconnects in solid oxide fuel cells. J Power Sources 2023;568:232831.
[150] Harthøj A, Holt T, Møller P. Oxidation behaviour and electrical properties of cobalt/cerium oxide composite coatings for solid oxide fuel cell interconnects. J Power Sources 2015;281:227–37.
[151] Piccardo P, Spotorno R, Geipel C. Investigation of a Metallic Interconnect Extracted from an SOFC Stack after 40,000 h of operation. Energies (Basel) 2022;15:3548.
[152] Mah JCW, Muchtar A, Somalu MR, Ghazali MJ. Metallic interconnects for solid oxide fuel cell: a review on protective coating and deposition techniques. Int J Hydrogen Energy 2017;42:9219–29.
[153] Tan KH, Rahman HA, Taib H. Coating layer and influence of transition metal for ferritic stainless steel interconnector solid oxide fuel cell: a review. Int J Hydrogen Energy 2019;44:30591–605.
[154] Hilger M, El Jardali K, Feyzi V, Vakhrameev D, Naumenko D, Schwaiger R, et al. Towards sustainable interconnects for solid oxide cells: an integrated technical and environmental evaluation of coating methods. J Power Sources 2025;659:238471.
[155] Liu T, Tao Y, Song H, Liu Y, Deng J, Yu Y, et al. Degradation mechanisms and protective coatings for ferritic stainless-steel interconnects of solid oxide fuel cells: a review. Mater Today Commun 2024;41:110802.
[156] Ignaczak J, Bik M, Lemieszek B, Kamecki B, Cempura G, Jasiński P, et al. Long-term stability and oxidation behavior of Mn_2CuO_4, $Mn_{1.9}Fe_{0.1}CuO_4$, $Mn_{1.7}Fe_{0.3}CuO_4$ coatings on SOFC interconnects: summary of a 10,000-h oxidation test. J Power Sources 2026;674:239785.
[157] Stanislowski M, Wessel E, Hilpert K, Markus T, Singheiser L. Chromium Vaporization from High-Temperature Alloys. J Electrochem Soc 2007;154:A295.
[158] Brylewski T, Molin S, Marczyński M, Mazur Ł, Domaradzki K, Kryshtal O, et al. Influence of Gd deposition on the oxidation behavior and electrical properties of a layered system consisting of Crofer 22 APU and $MnCo_2O_4$ spinel. Int J Hydrogen Energy 2021;46:6775–91.
[159] Froitzheim J, Canovic S, Nikumaa M, Sachitanand R, Johansson LG, Svensson JE. Long term study of Cr evaporation and high temperature corrosion behaviour of Co coated ferritic steel for solid oxide fuel cell interconnects. J Power Sources 2012;220:217–27.
[160] Rakshith Nugehalli Sachitanand. Thin-Film Coated Steel Foils as Interconnects for Solid Oxide fuel Cells (SOFC) Oxidation and Chromium Evaporation Properties. Chalmers University of Technology; 2015. PhD Thesis.
[161] Talic B, Hendriksen PV, Wiik K, Lein HL. Diffusion couple study of the interaction between Cr_2O_3 and $MnCo_2O_4$ doped with Fe and Cu. Solid State Ion 2019;332:16–24.
[162] Zanchi E, Ignaczak J, Molin S, Cempura G, Boccaccini AR, Smeacetto F. Electrophoretic co-deposition of $Mn_{1.5}Co_{1.5}O_4$, Fe_2O_3 and CuO: Unravelling the effect of simultaneous addition of Cu and Fe on the microstructural, thermo-mechanical and corrosion properties of in-situ modified spinel coatings for solid oxide cell interconnects. J Eur Ceram Soc 2022;42:3271–81.
[163] Moeini A, Bafte N, Malek Khachatourian A, Golmohammad M, Madaah Hosseini HR, Varma RS. Doping effects on microstructural, electrical, thermal, and oxidation properties of Mn–Co spinels as interconnect coat in fuel cell application: a review. Int J Hydrogen Energy 2025;162:150703.

[164] Goebel C, Fefekos AG, Svensson JE, Froitzheim J. Does the conductivity of interconnect coatings matter for solid oxide fuel cell applications? J Power Sources 2018;383:110–4.
[165] Zanchi E, Molin S, Sabato AG, Talic B, Cempura G, Boccaccini AR, et al. Iron doped manganese cobaltite spinel coatings produced by electrophoretic co-deposition on interconnects for solid oxide cells: Microstructural and electrical characterization. J Power Sources 2020;455.
[166] Magdefrau NJ, Chen L, Sun EY, Yamanis J, Aindow M. Formation of spinel reaction layers in manganese cobaltite-coated Crofer22 APU for solid oxide fuel cell interconnects. J Power Sources 2013;227:318–26.
[167] Fan Y, Zhang T, Hu Y, Lou L, Xu S, Gao J, et al. Pre-oxidation enables superior performance of low-cost AISI 441 SOFC interconnects: Suppressing stress-driven oxidation under dense spinel coating. Corros Sci 2026;268:113907.
[168] Cong W, Fu Y, He P, Lin T, Feng G, Zhang Z, et al. Microstructure evolution and chromium suppression mechanism in pre-oxidized Ce/Co-coated AISI 441 stainless steel for solid oxide fuel cell interconnects. Int J Hydrogen Energy 2025;167:151044.
[169] Liu D, Geng S, Chen G, Wang F. $NiO/NiFe_2O_4$ dual-layer coating on pre-oxidized SUS 430 steel interconnect. Int J Hydrogen Energy 2022;47:21462–71.
[170] Petric A, Ling H. Electrical conductivity and thermal expansion of spinels at elevated temperatures. J Am Ceram Soc 2007;90:1515–20.
[171] Tomas M, Goebel C, Svensson J-E, Froitzheim J. Cu-based Coatings for IT-SOFC applications. ECS Trans 2019;91:2291–8.
[172] Mazur Ł, Brylewski T. Electrophoretic Deposition and Physicochemical Properties of Ni- and Fe-Doped Cu–Mn Spinel Coatings Enhanced with $Ce_{0.9}Y_{0.1}O_2$ Nanoparticles on Fe16Cr Ferritic Stainless Steel Interconnects for SOEC applications. Metall Mater Trans A 2024;55:5100–13.
[173] Mehdizade M, Smeacetto F, Winiarski M, Małys M, Molin S. Role of Fe substitution in modifying the properties of $Mn_{2-x}CuFe_xO_4$ spinel oxide layers for SOFC interconnect applications. Int J Hydrogen Energy 2026;231:154933.
[174] Juuti T, Karjalainen P, Rovatti L, Heikkinen E-P, Pohjanne P. Contribution of Mo and Si to laves-phase precipitation in type 444 steel and its effect on steel properties — VTT's Research Information Portal. 7th European Stainless Steel Conference - Science and Market, Como, Italy 21 - 23.9.2011, Como: Associazione Italiana di Metallurgia AIM; 2011.
[175] Cavichiolo LS, Nørby TH, Pantleon K, Hald J. Effects of interdiffusion in nickel coated AISI 441 steel. Mater Charact 2022;194:112413.
[176] Cavichiolo LS, Nørby TH, Hald J, Pantleon K. Long-term effects of soft-chromising Ni-electroplated AISI 441 commodity steel for SOC stack interconnects. Corros Sci 2024;227:111728.
[177] Hindam H, Whittle DP. Microstructure, adhesion and growth kinetics of protective scales on metals and alloys. Oxid Met 1982;18:245–84.
[178] Palcut M, Mikkelsen L, Neufeld K, Chen M, Knibbe R, Hendriksen PV. Corrosion stability of ferritic stainless steels for solid oxide electrolyser cell interconnects. Corros Sci 2010;52:3309–20.
[179] Schmucker E, Petitjean C, Martinelli L, Panteix P-J, Ben Lagha S, Vilasi M. Oxidation of Ni-Cr alloy at intermediate oxygen pressures. I. Diffusion mechanisms through the oxide layer. Corros Sci 2016;111:474–85.
[180] Jian L, Huezo J, Ivey DG. Carburisation of interconnect materials in solid oxide fuel cells. J Power Sources 2003;123:151–62.
[181] Gheno T, Monceau D, Zhang J, Young DJ. Carburisation of ferritic Fe–Cr alloys by low carbon activity gases. Corros Sci 2011;53:2767–77.
[182] Opila EJ, Myers DL, Jacobson NS, Nielsen IMB, Johnson DF, Olminsky JK, et al. Theoretical and experimental investigation of the thermochemistry of CrO2 (OH)2 (g). J Phys Chem A 2007;111:1971–80.
[183] Ardigo-Besnard MR, Popa I, Heintz O, Chassagnon R, Vilasi M, Herbst F, et al. Effect of surface finishing on the oxidation behaviour of a ferritic stainless steel. Appl Surf Sci 2017;412:196–206.
[184] Ardigo MR, Popa I, Chevalier S, Weber S, Heintz O, Vilasi M. Effect of water vapor on the oxidation mechanisms of a commercial stainless steel for interconnect application in high temperature water vapor electrolysis. Oxid Met 2013;79:495–505.
[185] Sadeghimeresht E, Markocsan N, Joshi S. Isothermal oxidation behavior of HVAF-sprayed Ni and NiCr coatings in H2-H2O environment. Surf Coat Technol 2017;317:17–25.
[186] Sachitanand R, Sattari M, Svensson J-E, Froitzheim J. The Oxidation of Coated SOFC Interconnects in fuel Side Environments. Fuel Cells 2016;16:32–8.
[187] King MK, Mahapatra MK. Corrosion of nickel and nickel–phosphorous-coated AISI 430 in dry (Ar–3%H2) and humid hydrogen ($Ar–3\%H_2–3\%H_2O$) atmosphere. J Mater Res 2021;36:322–32.
[188] Li C, Wang J, Fan L, Jia L, Yang Y. Advances in SOEC electrodes, electrolytes, and stacks: a review of materials innovation and intellectual patent trends. Mater Sci Eng B 2025;322:118621.
[189] Brett DJL, Atkinson A, Brandon NP, Skinner SJ. Intermediate temperature solid oxide fuel cells. Chem Soc Rev 2008;37:1568–78.
[190] Gunduz KO, Chyrkin A, Goebel C, Froitzheim J. Unpublished Results.
[191] Naoumidis A, Schulze HA, Jungen W, Lersch P. Phase studies in the chromium-manganese-titanium oxide system at different oxygen partial pressures. J Eur Ceram Soc 1991;7:55–63.
[192] Essuman E, Meier GH, Zurek J, Hänsel M, Norby T, Singheiser L, et al. Protective and non-protective scale formation of NiCr alloys in water vapour containing high- and low-pO2 gases. Corros Sci 2008;50:1753–60.
[193] Chandra-Ambhorn S, Wouters Y, Antoni L, Toscan F, Galerie A. Adhesion of oxide scales grown on ferritic stainless steels in solid oxide fuel cells temperature and atmosphere conditions. J Power Sources 2007;171:688–95.
[194] Zurek J, Young DJ, Essuman E, Hänsel M, Penkalla HJ, Niewolak L, et al. Growth and adherence of chromia based surface scales on Ni-base alloys in high- and low-pO_2 gases. Mater Sci Eng A 2008;477:259–70.
[195] Michalik M, Hänsel M, Zurek J, Singheiser L, Quadakkers WJ. Effect of water vapour on growth and adherence of chromia scales formed on Cr in high and low pO_2-environments at 1000 and 1050°C. Mater High Temp 2005;22:213–21.
[196] Guillou S, Desgranges C, Chevalier S. Study of the growth mechanism of some oxide scales on alloy 230 in high temperature vapor electrolysis (HTVE) conditions. Defect Diffus. Forum, vol. 323, Trans Tech Publ; 2012, p. 577–82.
[197] Guillou S, Desgranges C, Chevalier S. Study of Conductivity of K41X Chromia Forming Alloy in High Temperature Electrolysis Environment. Oxid Met 2013;79:507–16.
[198] Ardigo-Besnard MR, Popa I, Chevalier S. Impact of pre-oxidation on the reactivity and conductivity in $H_2–H_2O$ atmosphere of a ferritic stainless steel for high temperature water vapour electrolysis. Int J Hydrogen Energy 2022;47:23508–13.
[199] Krogsgaard T, Svensson J-E, Froitzheim J. Oxidation of Ferritic Stainless Steels: Lessons Learnt from Ar-H2/H2O Exposures. 19th International Symposium on Solid Oxide Fuel Cells (SOFC-XIX), ECS. 2025.
[200] Rahmel A, Tobolski J. Einfluss von wasserdampf und kohlendioxyd auf die oxydation von eisen in sauerstoff bei hohen temperaturen. Corros Sci 1965;5:333–46.
[201] Norby T. Protonic defects in oxides and their possible role in high temperature oxidation. J Phys IV 1993;3:C9–.
[202] Norby T. The influence of hydrogen defects on transport properties of oxides. American Ceramic Society Inc, Nonstoichiometric Compounds Advances in Ceramics 1987;23:107–23.
[203] Essuman E, Meier GH, Żurek J, Hänsel M, Singheiser L, Quadakkers WJ. Enhanced internal oxidation as trigger for breakaway oxidation of Fe–Cr alloys in gases containing water vapor. Scr Mater 2007;57:845–8.
[204] Galerie A, Wouters Y, Caillet M. The kinetic behaviour of metals in water vapour at high temperatures: can general rules be proposed? Mater. Sci. Forum, vol. 369, Trans Tech Publ; 2001, p. 231–8.
[205] Young DJ. Effects of water vapour on the oxidation of chromia formers. Mater. Sci. Forum, vol. 595, Trans Tech Publ; 2008, p. 1189–97.
[206] Essuman E, Meier GH, Żurek J, Hänsel M, Quadakkers WJ. The effect of Water Vapor on Selective Oxidation of Fe–Cr Alloys. Oxid Met 2008;69:143–62.
[207] Essuman E, Meier GH, Zurek J, Hänsel M, Singheiser L, Quadakkers WJ. Enhanced internal oxidation as reason for breakdown of protective chromia scales on FeCr-alloys in water vapour containing gases. Mater Sci Forum 2008;595–598:699–706.
[208] Bin AMH, Kodama T, Ueda M, Kawamura K, Maruyama T. The effect of Water Vapor on High Temperature Oxidation of Fe-Cr Alloys at 1073 K. Mater Trans 2009;50:2656–63.

[209] Jullian D, Prillieux A, Zhang J, Young DJ. Oxygen permeability of Fe-Ni-Cr alloys at 1100 and 1150 °C under carbon-free and carbon-containing gases. Mater Corros 2017;68:197–204.
[210] Prillieux A, Jullian D, Zhang J, Monceau D, Young DJ. Internal oxidation in dry and wet conditions for oxygen permeability of Fe–Ni alloys at 1150 and 1100 °C. Oxid Met 2017;87:273–83.
[211] Jullian D, Prillieux A, Hibbert DB, Zhang J, Young DJ. Internal oxidation of austenitic Fe-Ni-Cr alloys at high temperatures: Deduction of oxygen permeability and the influence of carbon-bearing gases. Corros Sci 2023;224:111465.
[212] Jullian D, Zhang J, Hibbert DB, Young DJ. Oxygen solubility in austenitic Fe-Ni alloys at high temperatures. J Alloy Compd 2018;732:646–54.
[213] Chyrkin A, Cossu C, Svensson J-E, Froitzheim J. Effect of Hydrogen on the Internal Oxidation of a Pd–Cr Alloy in Dual-Atmosphere Conditions. Oxid Met 2022;97:527–38.
[214] Wang J, Mao S, Zhang J, Young DJ. Effects of Si, Mn, Ti and Ce on oxidation of Fe-Cr alloys in water vapour. Npj Mater. Degrad. 2025 9:1 2025;9:1–15.
[215] Chyrkin A. Unpublished Results.
[216] Auinger M, Praig VG, Linder B, Danninger H. Grain boundary oxidation in iron-based alloys, investigated by 18O enriched water vapour – the effect of mixed oxides in binary and ternary Fe–{Al, Cr, Mn, Si} systems. Corros Sci 2015;96:133–43.
[217] Gunduz KO, Chyrkin A, Goebel C, Hansen L, Hjorth O, Svensson JE, et al. The effect of hydrogen on the breakdown of the protective oxide scale in solid oxide fuel cell interconnects. Corros Sci 2021;179.
[218] Lukianova OA, Kulitckii V, Rao Z, Li Z, Wilde G, Divinski SV. Self-diffusion in carbon-alloyed CoCrFeMnNi high entropy alloys. Acta Mater 2022;237:118136.
[219] Yang G, Wang S, Potter A, Sumner J. Investigating the role of grain boundary hydrogen in dual atmosphere effects for solid oxide cells interconnect applications. Corros Sci 2026;258:113333.
[220] Chyrkin A, Divinski SV. Unpublished Results.
[221] Sarda V, Auvinen S, Shemet V, Quadakkers WJ, Pihlatie M, Kiviaho J, et al. Long Term Resistivity Behavior of SOFC Interconnect/Ni-Mesh/Anode Interfaces. ECS Trans 2013;57:2279.
[222] Chen M, Molin S, Zhang L, Ta N, Hendriksen PV, Kiebach W-R, et al. Modeling of Ni Diffusion Induced Austenite Formation in Ferritic Stainless Steel Interconnects. ECS Trans 2015;68:1691.
[223] Froitzheim J, Niewolak L, Brandner M, Singheiser L, Quadakkers WJ. Anode Side Diffusion Barrier Coating for Solid Oxide fuel Cells Interconnects. J Fuel Cell Sci Technol 2010;7.
[224] Niewolak L, Garcia-Fresnillo L, Meier GH, Quadakkers WJ. Sigma-phase formation in high chromium ferritic steels at 650°C. J Alloy Compd 2015;638:405–18.
[225] Alnegren P, Sattari M, Svensson J-E, Froitzheim J. Severe dual atmosphere effect at 600 °C for stainless steel 441. J Power Sources 2016;301:170–8.
[226] Alnegren P, Sattari M, Svensson J-E, Froitzheim J. Temperature dependence of corrosion of ferritic stainless steel in dual atmosphere at 600–800 °C. J Power Sources 2018;392:129–38.
[227] Tomas M, Visibile A, Svensson J-E, Froitzheim J. Novel coatings for protecting solid oxide fuel cell interconnects against the dual-atmosphere effect. Int J Hydrogen Energy 2023;48:18405–19.
[228] Shen F, Welander MM, Tucker MC. Oxidation of porous stainless steel supports for metal-supported solid oxide electrolysis cells. Int J Hydrogen Energy 2023;48:12168–75.
[229] Fontana S, Chevalier S, Caboche G. Metallic interconnects for solid oxide fuel cell: effect of water vapour on oxidation resistance of differently coated alloys. J Power Sources 2009;193:136–45.
[230] Ardigo MR, Popa I, Chevalier S, Girardon P, Perry F, Laucournet R, et al. Effect of coatings on long term behaviour of a commercial stainless steel for solid oxide electrolyser cell interconnect application in H2/H2O atmosphere. Int J Hydrogen Energy 2014;39:21673–7.
[231] Ardigo-Besnard MR, Popa I, Chevalier S. Effect of spinel and perovskite coatings on the long term oxidation of a ferritic stainless steel in H2/H2O atmosphere. Corros Sci 2019;148:251–63.
[232] Tomas M, Svensson J-E, Froitzheim J. Hydrogen-barrier coatings against dual-atmosphere corrosion for IT-SOFC interconnect applications. Int J Hydrogen Energy 2024;58:852–62.
[233] Kim C, Kim SH, Cha J-H, Jang C, Kim TK. Chromium diffusion coating on an ODS ferritic-martensitic steel and its oxidation behavior in air and steam environments. Coatings 2020;10:492.
[234] Rizvandi OB, Frandsen HL. Modeling of single- and double-sided high-pressure operation of solid oxide electrolysis stacks. Int J Hydrogen Energy 2023;48:30102–19.
[235] Todd D, Schwager M, Mérida W. Thermodynamics of high-temperature, high-pressure water electrolysis. J Power Sources 2014;269:424–9.
[236] Jensen SH, Sun X, Ebbesen SD, Knibbe R, Mogensen M. Hydrogen and synthetic fuel production using pressurized solid oxide electrolysis cells. Int J Hydrogen Energy 2010;35:9544–9.
[237] Hansen JB, Christiansen N, Nielsen JU. Production of Sustainable Fuels by Means of Solid Oxide Electrolysis. ECS Trans 2011;35:2941.
[238] Zhang N, Zhu Z, Lv F, Jiang D, Xu H. Influence of exposure pressure on oxidation behavior of the ferritic–martensitic steel in steam and supercritical water. Oxid Met 2016;86:113–24.
[239] Nakagawa K, Matsunaga Y, Yanagisawa T. Mater. High Temp. Corrosion behavior of ferritic steels on the air sides of boiler tubes in a steam/air dual environment 2014.
[240] Yang Z, Walker MS, Singh P, Stevenson JW. Anomalous Corrosion Behavior of Stainless Steels under SOFC Interconnect Exposure Conditions. Electrochem Solid St 2003;6:B35.
[241] Rufner J, Gannon P, White P, Deibert M, Teintze S, Smith R, et al. Oxidation behavior of stainless steel 430 and 441 at 800°C in single (air/air) and dual atmosphere (air/hydrogen) exposures. Int J Hydrogen Energy 2008;33:1392–8.
[242] Skilbred AWB, Haugsrud R. The effect of Water Vapour on the Corrosion of Sandvik Sanergy HT under dual Atmosphere Conditions. Oxid Met 2013;79:639–54.
[243] Bredvei Skilbred AW, Haugsrud R. The effect of dual atmosphere conditions on the corrosion of Sandvik Sanergy HT. Int J Hydrogen Energy 2012;37:8095–101.
[244] Ardigo MR, Popa I, Combemale L, Chevalier S, Herbst F, Girardon P. Dual atmosphere study of the K41X stainless steel for interconnect application in high temperature water vapour electrolysis. Int J Hydrogen Energy 2015;40:5305–12.
[245] Kurokawa H, Kawamura K, Maruyama T. Oxidation behavior of Fe–16Cr alloy interconnect for SOFC under hydrogen potential gradient. Solid State Ion 2004;168:13–21.
[246] Goebel C, Alnegren P, Faust R, Svensson J-E, Froitzheim J. The effect of pre-oxidation parameters on the corrosion behavior of AISI 441 in dual atmosphere. Int J Hydrogen Energy 2018;43:14665–74.
[247] Reisert M, Anisur MR, Lee L, Aphale AN, Hong J, Yaginuma M, et al. Corrosion of chromia-forming and alumina-forming ferritic stainless steels under dual atmosphere exposure conditions. J Electrochem Soc 2021;168:111506.
[248] Tomas M, Svensson J-E, Froitzheim J. Evaluation of selected Fe–Cr steels under single- and dual-atmosphere conditions for intermediate-temperature solid oxide fuel cell interconnect applications. Int J Hydrogen Energy 2024;65:112–25.
[249] Inuzuka R, Osada N, Imai K, Kameda T, Ishihara T. Accelerated High-Temperature Oxidation Behavior of Ferritic Stainless Steel under Air/H_2+H_2O dual Atmosphere. J Electrochem Soc 2024;171:084504.
[250] Amendola R, Gannon P, Ellingwood B, Hoyt K, Piccardo P, Genocchio P. Oxidation behavior of coated and preoxidized ferritic steel in single and dual atmosphere exposures at 800°C. Surf Coat Technol 2012;206:2173–80.
[251] Goebel C, Bo C, Svensson J-E, Froitzheim J. The Influence of Different Factors on the dual Atmosphere effect Observed for AISI 441 Interconnects used in Solid Oxide fuel Cells. ECS Trans 2019;91:2261.
[252] Li J, Yan D, Gong Y, Jiang Y, Li J, Pu J, et al. Investigation of anomalous oxidation behavior of SUS430 alloy in solid oxide fuel cell dual atmosphere. J Electrochem Soc 2017;164:C945.

[253] Yang Z, Walker MS, Singh P, Stevenson JW, Norby T. Oxidation Behavior of Ferritic Stainless Steels under SOFC Interconnect Exposure Conditions. J Electrochem Soc 2004;151:B669.
[254] Yang Z, Xia G, Singh P, Stevenson JW. Effects of water vapor on oxidation behavior of ferritic stainless steels under solid oxide fuel cell interconnect exposure conditions. Solid State Ion 2005;176:1495–503.
[255] Holcomb GR, Ziomek-Moroz M, Cramer SD, Covino BS, Bullard SJ. Dual-environment effects on the oxidation of metallic interconnects. J Mater Eng Perform 2006;15:404–9.
[256] Yang Z, Xia G-G, Walker MS, Wang C-M, Stevenson JW, Singh P. High temperature oxidation/corrosion behavior of metals and alloys under a hydrogen gradient. Int J Hydrogen Energy 2007;32:3770–7.
[257] Zhao Y, Fergus JW. Oxidation of Alloys 430 and 441 in SOFC dual atmospheres: effects of flow rate and humidity. J Electrochem Soc 2012;159:C109.
[258] Zhao Y, Fergus JW. Oxidation behavior of stainless steel 441 and 430 in dual atmosphere - effects of alloy grain boundaries. ECS Trans 2012;41:147.
[259] Leonard ME, Amendola R, Gannon PE, Shong W-J, Liu C-K. High-temperature (800 °C) dual atmosphere corrosion of electroless nickel-plated ferritic stainless steel. Int J Hydrogen Energy 2014;39:15746–53.
[260] Stygar M, Brylewski T, Kruk A, Przybylski K. Oxidation properties of ferritic stainless steel in dual Ar–H2–H2O/air atmosphere exposure with regard to SOFC interconnect application. Solid State Ion 2014;262:449–53.
[261] Stygar M, Dąbrowa J, Dziembaj P, Brylewski T. Influence of Gaseous Media Flow in the dual Ar-H2-H2O/air Atmosphere Setup on the Scale Growth Kinetics of Crofer 22APU Ferritic Stainless Steel. J Mater Eng Perform 2017;26:540–6.
[262] Wang R, Sun Z, Choi J-P, Basu SN, Stevenson JW, Tucker MC. Ferritic stainless steel interconnects for protonic ceramic electrochemical cell stacks: Oxidation behavior and protective coatings. Int J Hydrogen Energy 2019;44:25297–309.
[263] Niewolak L, Tietz F, Quadakkers WJ. 7 - Interconnects. In: Kendall K, Kendall M, editors. High-Temperature Solid Oxide Fuel Cells for the 21st Century (Second Edition), Boston: Academic Press; 2016, p. 195–254.
[264] Yen SK, Tsai YC. Critical hydrogen concentration for the brittle fracture of AISI 430 stainless steel. J Electrochem Soc 1996;143:2736.
[265] Causey RA, Karnesky RA, San MC. 4.16 - Tritium Barriers and Tritium Diffusion in Fusion Reactors. In: Konings RJM, editor. Comprehensive Nuclear Materials. Oxford: Elsevier; 2012. p. 511–49.
[266] Grolig JG, Froitzheim J, Svensson JE. Effect of cerium on the electrical properties of a cobalt conversion coating for solid oxide fuel cell interconnects - a study using impedance spectroscopy. Electrochim Acta 2015;184:301–7.
[267] Yang Z, Hardy JS, Walker MS, Xia G, Simner SP, Stevenson JW. Structure and Conductivity of Thermally Grown Scales on Ferritic Fe-Cr-Mn Steel for SOFC Interconnect applications. J Electrochem Soc 2004;151:A1825.
[268] Öztürk B, Topcu A, Öztürk S, Cora ÖN. Oxidation, electrical and mechanical properties of Crofer®22 solid oxide fuel cell metallic interconnects manufactured through powder metallurgy. Int J Hydrogen Energy 2018;43:10822–33.
[269] Yang Z, Xia G, Simner SP, Stevenson JW. Thermal growth and performance of manganese cobaltite spinel protection layers on ferritic stainless steel SOFC interconnects. J Electrochem Soc 2005;152:A1896.
[270] Mohsenifar F, Ebrahimifar H, Irannejad A. Applying the protective Mn–Co–La2O3 Coating on Crofer 22 APU Ferritic Stainless Steel used as Solid Oxide fuel Cell Interconnects. Acta Metall Sin (English Letters) 2024;37:872–88.
[271] Talic B, Molin S, Wiik K, Hendriksen PV, Lein HL. Comparison of iron and copper doped manganese cobalt spinel oxides as protective coatings for solid oxide fuel cell interconnects. J Power Sources 2017;372:145–56.
[272] Bianco M, Tallgren J, Hong J-E, Yang S, Himanen O, Mikkola J, et al. Ex-situ experimental benchmarking of solid oxide fuel cell metal interconnects. J Power Sources 2019;437:226900.
[273] Bianco M, Caliandro P, Diethelm S, Yang S, Dellai A, Van herle J, et al. In-situ experimental benchmarking of solid oxide fuel cell metal interconnect solutions. J Power Sources 2020;461:228163.
[274] Chevalier S, Combemale L, Popa I, Chandra-ambhorn S, Chandra-ambhorn W, Promdirek P, et al. CHAPTER 6 Development of SOFC Interconnect Stainless Steels. Solid State Phenom 2020;300:135–56.
[275] Jeon B, Van Overmeere Q, van Duin ACT, Ramanathan S. Nanoscale oxidation and complex oxide growth on single crystal iron surfaces and external electric field effects. PCCP 2013;15:1821–30.
[276] Kodjamanova P, Fu Q, Gautier L. Electric current effects on the corrosion behaviour of high chromium ferritic steels. Oxid Met 2013;79:53–64.
[277] Kawamura K, Nitobe T, Kurokawa H, Ueda M, Maruyama T. Effect of Electric current on growth of Oxide Scale on Fe–25Cr Alloy for SOFC Interconnect at 1073 K. J Electrochem Soc 2012;159:B259.
[278] Ryter J, Amendola R, McCleary M, Shong W-J, Liu C-K, Spotorno R, et al. Effect of electrical current on the oxidation behavior of electroless nickel-plated ferritic stainless steel in solid oxide fuel cell operating conditions. Int J Hydrogen Energy 2018;43:426–34.
[279] Li J, Zhang W, Yang J, Yan D, Pu J, Chi B, et al. Oxidation behavior of metallic interconnect in solid oxide fuel cell stack. J Power Sources 2017;353:195–201.
[280] Molin S, Jasinski P, Mikkelsen L, Zhang W, Chen M, Hendriksen PV. Low temperature processed MnCo2O4 and MnCo1.8Fe0.2O4 as effective protective coatings for solid oxide fuel cell interconnects at 750 °C. J Power Sources 2016;336:408–18.
[281] Malzbender J, Batfalsky P, Vaßen R, Shemet V, Tietz F. Component interactions after long-term operation of an SOFC stack with LSM cathode. J Power Sources 2012;201:196–203.
[282] Niewolak L, Blum L, Peters R, Grüner D, Quadakkers WJ. Behavior of Metallic Components during 4,000 h operation of an SOFC Stack with Carbon Containing fuel Gas. Fuel Cells 2016;16:600–10.
[283] Groß-Barsnick SM, Fang Q, Batfalsky P, Niewolak L, Blum L, Quadakkers WJ. Post-test Characterization of Metallic Materials and Adjacent Components in an SOFC Stack after 34,000 h operation at 700 °C. Fuel Cells 2019;19:84–95.
[284] Bianco M, Ouweltjes JP, Van herle J. Degradation analysis of commercial interconnect materials for solid oxide fuel cells in stacks operated up to 18000 hours. Int J Hydrogen Energy 2019;44:31406–22.
[285] Ghiara G, Piccardo P, Bongiorno V, Geipel C, Spotorno R. Characterization of metallic interconnects extracted from solid oxide fuel cell stacks operated up to 20,000 h in real life conditions: the air side. Energies (Basel) 2020;13:6487.
[286] Ghiara G, Piccardo P, Bongiorno V, Repetto L, Geipel C, Spotorno R. Characterization of metallic interconnects extracted from Solid Oxide fuel Cell stacks operated up to 20,000 h in real life conditions: the fuel side. Int J Hydrogen Energy 2021;46:23815–27.
[287] Aicart J, Couturier K, Hubert M, Vulliez K, Elie M, Champelovier L, et al. Component analysis of a 25-cell stack following 6.7 kh of high temperature electrolysis. Int J Hydrogen Energy 2024;93:562–73.
[288] Lenser C, Zurek J, Naumenko D, Thieu C-A, Son J-W, de Haart U, et al. Performance analysis of a planar solid oxide fuel cell stack between 750 °C and 500 °C. J Power Sources 2020;474:228671.
[289] Menzler NH, Sebold D, Guillon O. Post-test characterization of a solid oxide fuel cell stack operated for more than 30,000 hours: the cell. J Power Sources 2018;374:69–76.
[290] Yang J, Huang W, Wang X, Li J, Yan D, Pu J, et al. Study on component interface evolution of a solid oxide fuel cell stack after long term operation. J Power Sources 2018;387:57–63.